

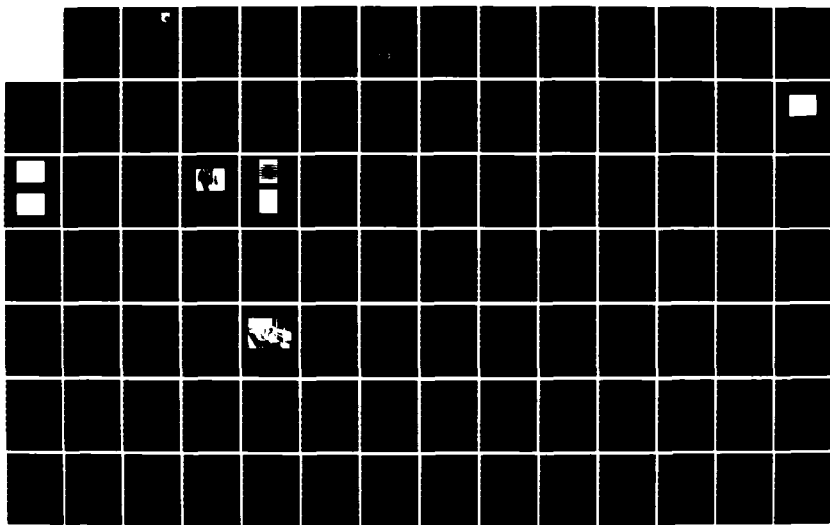
AD-A165 950 TECHNIQUES FOR OPTICAL INTERFEROMETROGRAPHY(U) DAYTON
UNIV OH RESEARCH INST R J LIGHTMAN ET AL. DEC 85
UDR-TR-85-101 AFMRL-TR-85-3098 F33615-83-C-3020

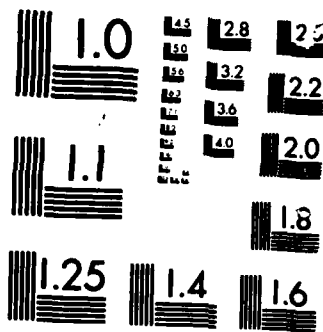
1/2

UNCLASSIFIED

F/G 20/6

NL





MICROCOPY RESOLUTION TEST CHART

AD-A165 950

AFWAL-TR-85-3098

TECHNIQUES FOR OPTICAL INTERFERANEMOGRAPHY

A. J. Lightman and S. Cartwright
University of Dayton
Research Institute
Dayton, OH 45469-0001



December 1985

Final Report for Period 15 September 1983 - 16 June 1985

Approved for Public Release; Distribution is Unlimited

DTIC FILE COPY

FLIGHT DYNAMICS LABORATORY
AIR FORCE WRIGHT AERONAUTICAL LABORATORIES
AIR FORCE SYSTEM COMMAND
WRIGHT-PATTERSON AIR FORCE BASE, OH 45433-6563

2
DTIC
SELECTED
S MAR 25 1986 **D**
B

NOTICE

When Government drawings, specifications, or other data are used for any purpose other than in connection with a definitely related Government procurement operation, the United States Government thereby incurs no responsibility nor any obligation whatsoever; and the fact that the government may have formulated, furnished, or in any way supplied the said drawings, specifications, or other data, is not to be regarded by implication or otherwise as in any manner licensing the holder or any other person or corporation, or conveying any rights or permission to manufacture use, or sell any patented invention that may in any way be related thereto.

This report has been reviewed by the Office of Public Affairs (ASD/PA) and is releasable to the National Technical Information Service (NTIS). At NTIS, it will be available to the general public, including foreign nations.

This technical report has been reviewed and is approved for publication.

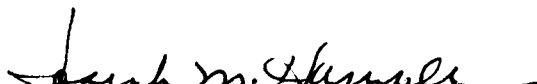


George L. Seibert
GEORGE L. SEIBERT, Tech Mgr
Aero-Optic Instrumentation Group
Experimental Engineering Branch

FOR THE COMMANDER



DONALD A. DREESBACH, Colonel, USAF
Chief, Aeromechanics Division
Flight Dynamics Laboratory



Joseph M. Hamble
JOSEPH M. HAMBLE, Chief
Experimental Engineering Branch
Aeromechanics Division

"If your address has changed, if you wish to be removed from our mailing list, or if the addressee is no longer employed by your organization please notify AFWAL/FIMN, W-PAFB, OH 45433 to help us maintain a current mailing list".

Copies of this report should not be returned unless return is required by security considerations, contractual obligations, or notice on a specific document.

UNCLASSIFIED

SECURITY CLASSIFICATION OF THIS PAGE

AD-A165950

| REPORT DOCUMENTATION PAGE | | | |
|---|--|---|--------------------------------------|
| 1a. REPORT SECURITY CLASSIFICATION Unclassified | | 1b. RESTRICTIVE MARKINGS | |
| 2a. SECURITY CLASSIFICATION AUTHORITY N/A | | 3. DISTRIBUTION/AVAILABILITY OF REPORT Approved for public release; Distribution is unlimited. | |
| 2b. DECLASSIFICATION/DOWNGRADING SCHEDULE N/A | | | |
| 4. PERFORMING ORGANIZATION REPORT NUMBER(S) UDR-TR-85-101 | | 5. MONITORING ORGANIZATION REPORT NUMBER(S) AFWAL-TR-85-3098 | |
| 6a. NAME OF PERFORMING ORGANIZATION University of Dayton Research Institute | 6b. OFFICE SYMBOL (If applicable) | 7a. NAME OF MONITORING ORGANIZATION Air Force Wright Aeronautical Laboratories Flight Dynamics Laboratory (AFWAL/FIMN) | |
| 6c. ADDRESS (City, State and ZIP Code) 300 College Park Dayton, OH 45469 | | 7b. ADDRESS (City, State and ZIP Code) WPAFB, OH 45433 | |
| 8a. NAME OF FUNDING/SPONSORING ORGANIZATION Flight Dynamic Laboratory | 8b. OFFICE SYMBOL (If applicable) AFWAL/FIMN | 9. PROCUREMENT INSTRUMENT IDENTIFICATION NUMBER F33615-83-C-3020 | |
| 8c. ADDRESS (City, State and ZIP Code) WPAFB, OH 45433 | | 10. SOURCE OF FUNDING NOS. PROGRAM ELEMENT NO. 61102F PROJECT NO. 2404 TASK NO. 13 WORK UNIT NO. 20 | |
| 11. TITLE (Include Security Classification) Techniques for Optical Interferanemography | | | |
| 12. PERSONAL AUTHOR(S) A. J. Lightman and S. Cartwright | | | |
| 13a. TYPE OF REPORT Final | 13b. TIME COVERED FROM 9/15/83 TO 6/16/85 | 14. DATE OF REPORT (Yr., Mo., Day) December 1985 | 15. PAGE COUNT 116 |
| 16. SUPPLEMENTARY NOTATION Lau | | | |
| 17. COSATI CODES FIELD 20 GROUP 06 SUB. GR. | | 18. SUBJECT TERMS (Continue on reverse if necessary and identify by block number) optical interferanemography; flow diagnostics laser Doppler anemometry Lau interferometry; | |
| 19. ABSTRACT (Continue on reverse if necessary and identify by block number) The suitability of available anemometry and interferometry systems for forming an optical interferanemography system has been evaluated. It was determined that a three-dimensional laser Doppler interferometer (LDA) should be able to provide the spatial and velocity resolution required. All standard interferometric systems measure the integrated index variation along the line of sight. Consequently, they do not provide spatial resolution and are only adequate in systems that are symmetric along the line of sight. If spatial resolution is required, a tomographic system can be used but the optical access required exceeds that commonly available in wind tunnels. To overcome these shortcomings a new interferometric technique was searched for. It was found that the Lau interferometer could be modified so that measurements were made in a restricted volume. The interferometer that was assembled and tested operated in a shearing mode. The system used a white light source, yielding a bright image, and the system is able to withstand severe vibrations without degrading the signal. The Lau interferometer has been examined in detail | | | |
| 20. DISTRIBUTION/AVAILABILITY OF ABSTRACT UNCLASSIFIED/UNLIMITED <input checked="" type="checkbox"/> SAME AS RPT. <input type="checkbox"/> DTIC USERS <input type="checkbox"/> | | 21. ABSTRACT SECURITY CLASSIFICATION Unclassified | |
| 22a. NAME OF RESPONSIBLE INDIVIDUAL George Seibert | | 22b. TELEPHONE NUMBER (Include Area Code) 513-255-2809 | 22c. OFFICE SYMBOL AFWAL/FIMN |

UNCLASSIFIED

SECURITY CLASSIFICATION OF THIS PAGE

Section 19 continued

and the theory of operation is presented.

Keywords - field /

UNCLASSIFIED

SECURITY CLASSIFICATION OF THIS PAGE

TABLE OF CONTENTS

| SECTION | PAGE |
|---|------|
| I INTRODUCTION | 1 |
| II INTERFEROMETRIC MEASUREMENT OF LOCALIZED FLOW-FIELD DENSITIES | 3 |
| 1. Interferometry Principles | 3 |
| 2. Optical System | 4 |
| 3. The Lau Interferometer | 9 |
| 4. Lau Interferometer Experiments | 18 |
| III COMBINED LDA/LAU INTERFEROMETRIC INTERFER- ANEMOGRAPHY SYSTEM | 25 |
| IV SUMMARY AND CONCLUSIONS | 27 |
| REFERENCES | 29 |
| APPENDIX | A-1 |

S DTIC
 ELECTED
 MAR 25 1986 **D**
B



| | |
|---------------|-------------------------------------|
| Accession For | |
| NTIS | <input checked="" type="checkbox"/> |
| DTIC | <input type="checkbox"/> |
| Unan. | <input type="checkbox"/> |
| Just | <input type="checkbox"/> |
| | |
| By | <input type="checkbox"/> |
| Dist | <input type="checkbox"/> |
| Avail | <input type="checkbox"/> |
| Dist | <input type="checkbox"/> |
| A-1 | |

LIST OF ILLUSTRATIONS

| FIGURE | | PAGE |
|--------|---|------|
| 1 | Initial Moire Technique for Localized Imaging. | 5 |
| 2 | The Optical Phase-Measurement System Implemented. The system was first operated with coherent illumination at G_1 and then adapted to incoherent illumination. | 7 |
| 3 | An Alternate Optical Phase Measurement System Using Wollaston Prisms. | 8 |
| 4 | Geometrical Interpretation of the Lau Inter- ferometer. | 14 |
| 5 | Infinite Fringe Lau Interferogram of a Gas Stream. | 19 |
| 6 | Lau Interferogram of a Gas Stream When Bias Fringes are Added. | 20 |
| 7 | Lau Interferogram of Object Used in Figure 6, but Object Moved out of the Region of Focus. | 20 |
| 8 | Mach-Zehnder Interferogram of a Thermal Gradient from a Heated Nichrome Wire Wrapped Around a Glass Rod (~ 2 mm diam). The interferogram was taken end- on. The thermal gradient is clearly evident. | 23 |
| 9 | Lau Interferometer Bias Fringes with Unheated Wire. | 24 |
| 10 | Difference Image Obtained by Electronically Sub- tracting Lau Interferogram of Unheated Object from the Heated Object Interferogram. The shift in the fringe position is clearly evident. | 24 |
| 11 | Combined Lau Interferometer and 3-D LDA Systems to Form an Interferanemography System. | 26 |

LIST OF SYMBOLS

| | |
|----------------------|--|
| b | = grating spacing |
| d | = distance |
| F, f | = focal length of lens |
| $G(x)$ | = complex amplitude transmittance of an object |
| K_{DG} | = Dale-Gladstone constant |
| l | = distance along optical path |
| n | = index of refraction |
| s | = fringe shift |
| $W(x', x'', \omega)$ | = cross-spectral density function between locations x' and x'' at frequency ω |
| x, y, z | = rectangular frame position coordinates in flowfield |
| δ | = displacement from focal plane |
| Δ | = displacement |
| λ | = wavelength of light |
| ρ | = density |

SECTION I INTRODUCTION

As part of Contract No. F33615-83-C-3020 the University of Dayton has conducted a study of technologies required for an interferanemography system. Interferometry and laser Doppler anemometry were evaluated for their applicability to interferanemography, as were other technologies.

The specified requirements for an interferanemographic system are to provide real-time/on-line simultaneous measurements of density and velocity in complex flow fields.

Interferometry is a generally accepted method for measurement of air density. Within the past decade holographic interferometric techniques have been used successfully to obtain density data in a variety of wind tunnel studies. However, the general application and wide use of interferometry is hindered in wind tunnel studies by the following: (a) single line-of-sight views of the flow field which limit the application to 2-D or 3-D axisymmetric fields, (b) insufficient measurements for optically weak fields (i.e., hypersonic flows or low-density flows), (c) manual data reduction methods now widely used. The application of traditional interferometry to flow-field measurements is presented in Appendix A, which is the Interim Technical Report UDR-TR-84-48 . In view of the limitations of standard interferometric techniques, the Lau interferometer was adapted for use in flow-field measurements. This has led to some novel operational capability for interferometers, including measurement in a restricted volume.

Laser Doppler techniques have been used to measure velocities in subsonic and supersonic flow fields. Laser Doppler Anemometry (LDA) is a process whereby changes in the frequency (Doppler shifting) of laser radiation scattered from particles moving through an optical control volume are monitored to compute the velocity of the moving particles.

Appendix A, the Interim Technical Report, presents a development of the requirements and techniques for interferometric measurements of a general three-dimensional flow field. As a part of the study using interferometry, it was necessary to characterize the interferometer sensitivities for the different wind tunnels at Wright-Patterson Air Force Base, and the results of this comparison are presented in Section 2, Appendix A.

Section 3, Appendix A, presents a development of the LDA requirements and techniques for characterization of local velocities in a complex flow field. Alternate techniques for measurement of the local velocities are compared to LDA to see if they offer any advantage over LDA in work by the Flight Dynamics Laboratory.

Section 4, Appendix A, summarizes the potential of existing technology to obtain real-time/on-line interferanemographic measurements in complex flow fields.

The theory of the Lau interferometer, as it was used for flow-field measurement, is developed in Section II of this report. The system performance was demonstrated through visualization measurements of the varying density fields of a freon jet exiting into air and of a thermal field around a heated cylinder. These are presented in Section III of this report.

SECTION II

INTERFEROMETRIC MEASUREMENT OF LOCALIZED FLOW-FIELD DENSITIES

The goal of this program was to provide an interferometric technique capable of making localized measurements of density in a flow field. This is to be combined with a velocity probe. The velocity probe analysis was submitted as an Interim Technical Report, and is attached as Appendix A. Included in that interim report was a discussion of the status of interferometry and its application to density measurements. The basic problem is that interferometric techniques integrate the phase variation along the optical path. In this report we will discuss our attempts to find a localized measurement technique. The study has led to the adaptation of the Lau interferometer. The optical configuration, its method of operation, and its potential for localized measurements will be described in the following paragraphs.

1. INTERFEROMETRY PRINCIPLES

As a ray of light traverses a medium, the phase of the electromagnetic radiation at any location is dependent upon the refractive index of the medium integrated along the optical path.¹ If two rays travelling different optical paths are mixed, the resulting fringe shift is given by

$$S(x,y) = \frac{1}{\lambda} \int (n(x,y,z) - n_{ref}) dz$$

[see Appendix A, Equation (1)]. This equation shows that the effect observed is the result of the difference in index of refraction of the test ray from the reference ray, integrated along the entire optical path. To limit the region of observation it is necessary to provide a common path for the interrogation ray and the reference ray over the entire path length, except in the region of interest. This will yield a local measurement of index change which can be related to the local density variation through the Dale-Gladstone coefficient

$$K_{DG} = \frac{n-1}{\rho}$$

by the equation

$$\Delta\rho = \Delta n / K_{DG}$$

2. OPTICAL SYSTEM

The initial concept was based upon the use of an optical system using fast lenses and a white-light source. A white-light illuminated grating was focused in the region of interest and then reimaged on a matching grating. The transmission of the combined gratings was then imaged onto a detector (Figure 1). Since the source was incoherent, every point on the first grating would be an effective source, independent of every other position on the grating. By appropriately selecting components the radiation from each source would propagate along a common optical path for most of the region. Only in the region of interest would the optical paths be distinctly separate. Once past this region the optical paths would again merge. As a result of the common path, only phase variation in the region of interest results in relative path length variation. In the original concept the phase variation would lead to a deflection of the emerging ray and a deflection of the image, resulting in a moire effect. Unfortunately, a lens is the ideal component for re-imaging the deflected ray back onto the same location where the undeflected ray reimages and, as a result, no effect was observed.

The concept was considered to be still valid; the question was how to convert a deflection into a movement of the image. The answer comes from Fourier optics. A change in direction in the front focal plane of a lens is equivalent to a deflection due to a spatial index variation and it will result in a translation of the image in the back focal plane by an amount proportional to the angle (spatial frequency). Of the many potential

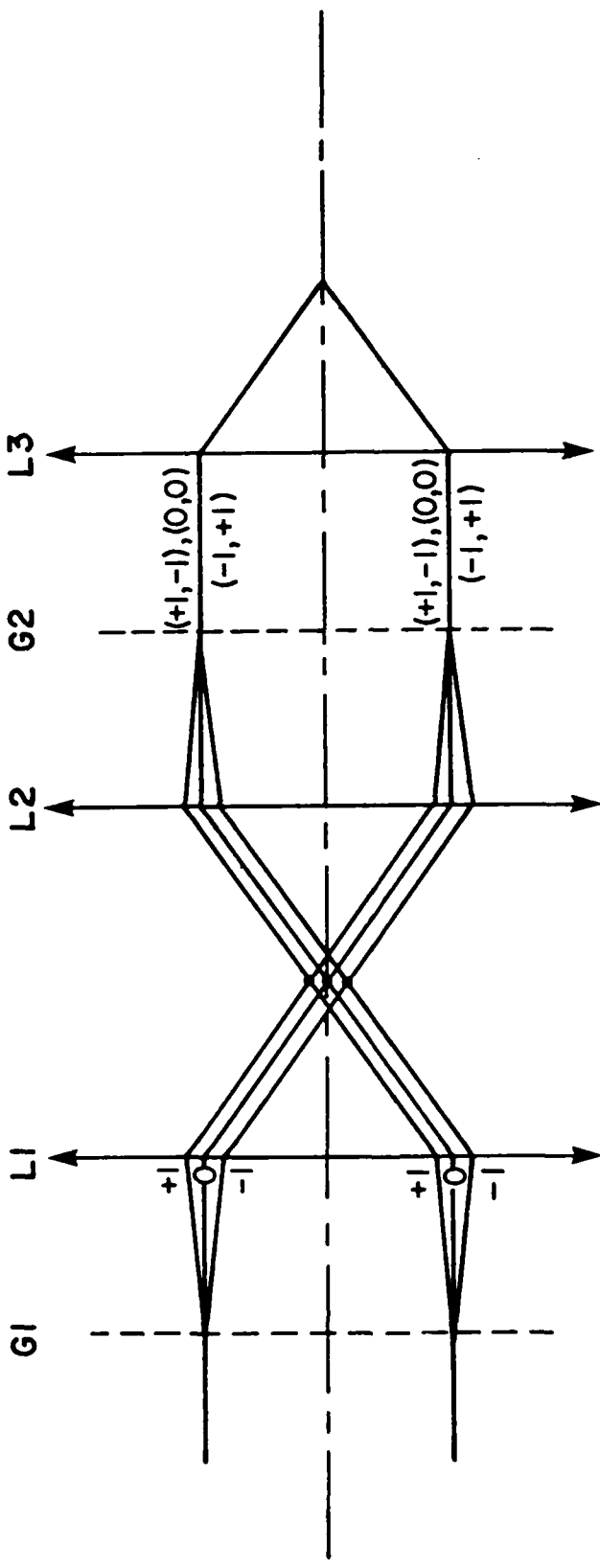


Figure 4. Geometrical Interpretation of the Lau Interferometer.

realizations of such a system we studied two in detail and implemented one in the laboratory.

The concept of the system implemented is simple to visualize when using a coherent source and then straightforward to extend to an incoherent source. When coherent light illuminates a subject in the front focal plane of a lens, the spatial Fourier transform is imaged at the rear focal plane of the lens. If the subject is a Ronchi ruling, the spatial Fourier transform is a series of equally spaced dots, with a well known intensity variation, along a line through the optical axis in a direction normal to the ruling. The second lens retransforms the rays, reforming the image (Figure 2). If there is a spatial phase variation at the original Fourier plane, the resulting image would vary in a manner related to the phase variation. In reforming the image onto a matched ruling, variations in the reformed image would become apparent. To overcome the presence of dead spots in the Fourier plane--spatial locations where there is no light to interrogate the local density--the system was changed from a coherent source to an incoherent white light source. The wide range of wavelengths results in a uniform coverage at the front focal plane. The validity of employing an incoherent source is discussed in Section III.

The other potential system considered is closely related to the first. The optical system would provide two optical beams at a small angle to each other but overlapping over most of their passage through the optical system. They would distinctly separate only near the focal plane. The reimaged system would be reformed into a single path, focused onto a detector, and mixed in the detection process. This system can be implemented using Wollaston prisms as shown in Figure 3. The observed signal would be the variation in intensity. In this format the signal is a coarse measurement tool. Several optical systems with much higher resolution, based on this technique, can be realized in a straightforward manner. For example, a Bragg cell used as a beam splitter

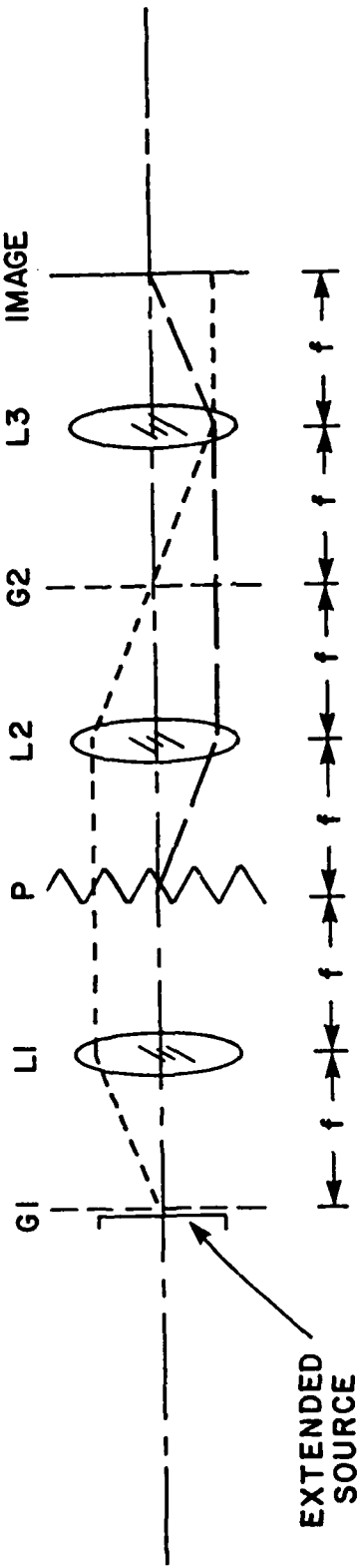


Figure 2. The Optical Phase-Measurement System Implemented. The system was first operated with coherent illumination at G_1 and then adapted to incoherent illumination (L_1 - lens with focal length f , G_i - grating, P phase object)

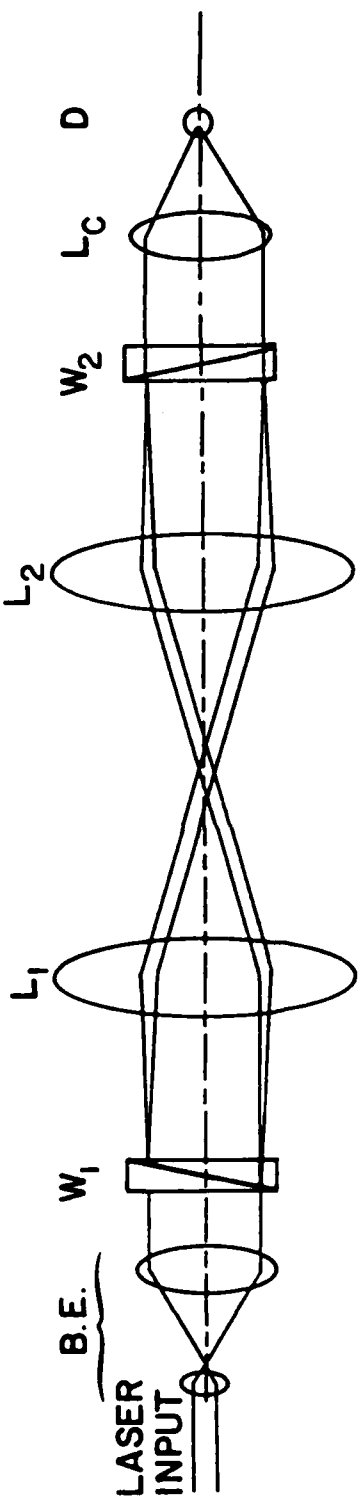


Figure 3. An Alternate Optical Phase Measurement System Using
Wollaston prisms (BE - beam expander, W_1 - Wollaston prism,
 L_1 - lens, D - detector).

would also introduce a frequency offset and produce a bias frequency making phase sensitive detection usable. The system might be worth pursuing in a separate investigation.

The optical system selected in the current study is a Lau interferometer. The application of this system to the measurement of flowfields is novel and we will report the results. The system is very robust, is easy to align, and uses a bright white-light source. All of these properties are advantageous when taking measurements in wind tunnels where there is often a high-level acoustic environment, where it is difficult to get good optical access, and where light collection efficiency is poor.

3. THE LAU INTERFEROMETER

It is well known that incoherent light can gain a measure of coherence merely by propagating through space as described by the van Cittert-Zernicke Theorem.² We will denote the state of coherence by the cross-spectral density function³ $W(x',x'',\omega)$ which describes the phase relationship between two points x' and x'' as a function of the frequency ω or equivalently the wavelength λ . The cross-spectral density function may be propagated through a system by a series of Fresnel-like integrals in the same manner as the mutual coherence function.⁴ The cross-spectral density function has the added benefit that it is a valid description for broadband illumination; the more commonly used mutual coherence function is valid only in the quasi-monochromatic approximation.

We can use the propagation integral to find the relation between the coherence of light fields on opposite sides of a lens, a situation common to most optical systems. At the distance d in front of the lens an object with complex amplitude transmittance $G(x_1)$ is illuminated by light with a cross-spectral density function $W_1(x_1',x_1'')$ (the ω is dropped for convenience). The light propagation to the lens is represented by $\exp[-i\pi x_2^2/\lambda F]$.

We calculate the cross-spectral density function $W_3(x'_3, x''_3)$ in a plane located $F-\Delta$ away from the lens. It will be convenient later to consider displacements about the focal plane, but Δ should not be considered a small quantity. By repeated application of the double Fresnel integral we arrive at

$$W_3(x'_3, x''_3) = C \iint e^{-\frac{i\pi}{\lambda F} x'_2^2} e^{i\frac{\pi}{\lambda F} x''_2^2} \iint W_1(x'_1, x''_1) G(x'_1) G^*(x''_1) \\ x \cdot e^{\frac{i\pi}{\lambda d} [(x'_2 - x'_1)^2 - (x''_2 - x''_1)^2]} dx'_1 dx''_1 e^{\frac{i\pi}{\lambda(F-\Delta)} [(x'_3 - x'_2)^2 - (x''_3 - x''_2)^2]} dx'_2 dx''_2 . \quad (1)$$

The factor C contains the constants of propagation. It is convenient to switch to a sum and difference notation. We let $x_1 = (x'_1 + x''_1)$, $\Delta x_1 = x'_1 - x''_1$. Then equation (1) becomes:

$$W(x_3, \Delta x_3) = C \iint e^{-\frac{i2\pi}{\lambda F} x_2 \Delta x_2} \iint W_1(x_1, \Delta x_1) G(x_1 + \frac{\Delta x_1}{2}) G^*(x_1 - \frac{\Delta x_1}{2}) \\ x \cdot e^{\frac{i2\pi}{\lambda d} [x_2 \Delta x_2 + x_1 \Delta x_1 - x_1 \Delta x_2 - x_2 \Delta x_1]} e^{\frac{i2\pi}{\lambda(F-\Delta)} [x_3 \Delta x_3 + x_2 \Delta x_2 - x_2 \Delta x_3 - x_3 \Delta x_2]} \\ x \cdot dx_1 d\Delta x_1 dx_2 d\Delta x_2 . \quad (2)$$

We note that by letting $\Delta x_3 = 0$ we find the intensity in plane 3.

After a great deal of tedious but straightforward manipulation of Equation (2) we arrive at

$$W_3(x_3, \Delta x_3) = Ce^{\frac{i2\pi}{\lambda} \frac{a}{F-\Delta a} x_3 \Delta x_3} \iint W_1(x_1, \Delta x_1) G(x_1 + \frac{\Delta x_1}{2}) G^*(x_1 - \frac{\Delta x_1}{2})$$

$$x e^{i \frac{2\pi}{\lambda} \frac{\Delta/F}{F-\Delta\alpha} x_1 \Delta x_1} e^{-i \frac{2\pi}{\lambda} \frac{1}{F-\Delta\alpha} (x_1 \Delta x_3 + x_3 \Delta x_1)} dx_1 d\Delta x_1 \quad (3)$$

where $\alpha = 1-d/F$.

We can distinguish several cases of interest. If $\Delta = 0$ (observation in the focal plane of the lens) then

$$W_3(x_3, \Delta x_3) = Ce^{i \frac{2\pi}{\lambda} \frac{\alpha}{F} x_3 \Delta x_3} \int \int W_1(x_1, \Delta x_1) G(x_1 + \frac{\Delta x_1}{2}) G^*(x_1 - \frac{\Delta x_1}{2}) \\ x e^{-i \frac{2\pi}{\lambda F} (x_1 \Delta x_3 + x_3 \Delta x_1)} dx_1 d\Delta x_1 . \quad (4)$$

For any state of coherence W_1 , there is a two-dimensional Fourier transform relationship between W_1 and W_3 .

If $W_1(x_1, \Delta x_1) = \delta(\Delta x_1)$, then the input illumination is totally incoherent. Equation (3) becomes

$$W_3(x_3, \Delta x_3) = Ce^{i \frac{2\pi}{\lambda} \frac{\alpha}{F-\Delta\alpha} x_3 \Delta x_3} \int G(x_1) G^*(x_1) e^{-i \frac{2\pi}{\lambda(F-\Delta)} x_1 \Delta x_3} dx_1 \\ = Ce^{i \frac{2\pi}{\lambda} \frac{\alpha}{F-\Delta\alpha} x_3 \Delta x_3} \tilde{G}(\frac{\Delta x_3}{\lambda(F-\Delta)}) \quad (5)$$

where \tilde{G} is the Fourier transform of $|G|^2$, the intensity transmittance of the object.

Equation (5) is a significant result. At all distances beyond the lens the field coherence is in the form of a Fourier transform of the input object. The effect of changing Δ is to

change the scaling of the Fourier transform. The coordinate of the Fourier transform is the difference coordinate Δx . That is, if a point x_0 is fixed in the observation plane, Equation (5) gives the coherence relation a distance Δx away from x_0 . There is no fixed reference system for evaluating Equation (5); it must be evaluated for every point in the plane of interest.

We will consider the special case of a grating-like input in plane 1. Let

$$G(x) = T(x) * \sum_{n=-\infty}^{\infty} \delta(x-nb), \quad (6)$$

where * represents convolution. Equation (6) describes a function $T(x)$ replicated about $x = nb$, $n = 0, \pm 1, \pm 2, \dots$ $T(x)$ can be considered a grating line shape and has a width less than b . In the case of a simple grating or Ronchi ruling $T(x)$ is either 1 or 0, so $T(x) = |T(x)|^2$. Equation (5) then becomes

$$W_3(x_3, \Delta x_3) = Ce^{j\frac{2\pi}{\lambda} \frac{a}{F-\Delta} x_3 \Delta x_3} \tilde{T}\left(\frac{\Delta x_3}{\lambda(F-\Delta)}\right) \sum_{m=-\infty}^{\infty} \delta\left(\frac{\Delta x_3}{\lambda(F-\Delta)} - \frac{m}{b}\right). \quad (7)$$

That is, the coherence function is a set of delta functions spaced at $\Delta x_3 = m\lambda(F-\Delta)/b$ and weighted by $\tilde{T}(\Delta x_3/\lambda(F-\Delta))$. If a point x_0 is chosen as a reference, then a point at $x_0 + \lambda(F-\Delta)/b$ will be coherent, but a point immediately adjacent to it will not.

The fact that an incoherently illuminated grating will give rise to a grating-like coherence function is the basis of the Lau effect.⁵ A second grating illuminated by the coherence function of Equation (7) will sample the coherence function. If the distance between gratings is properly chosen, the second grating will only sample points that are coherent with respect to each

other. That light will propagate to the far-field and form interference fringes. Thus, the Lau effect describes a coherent interference phenomenon which arises from incoherently illuminating a periodic structure.

The Lau effect can form the basis of an interferometer as first described by Bartelt and Jahns⁶ and later by Sudol.⁷ The classic Lau effect requires propagation from one grating to another to produce the interference fringes. The interferometer uses a modified version where the first grating is imaged onto the second to give an effective distance of zero. The interference fringes are viewed in the far-field of the second grating by use of a lens. The setup is diagrammed in Figure 2. An incoherent source (in our case a tungsten lamp) is imaged onto the first grating G_1 to provide an incoherent periodic source. G_1 is imaged onto G_2 by the lenses L_1 and L_2 . Interference is observed in the focal plane of lens L_3 , which is also the image of plane P. The interference phenomenon can be understood from a geometrical point of view by considering Figure 4. The light falling on G_1 will consist of many plane waves at different angles and wavelengths. Any one plane wave will be broken up into three major components which we designate as the 0 (undiffracted), +1, and -1 orders. These components are imaged onto G_2 where they are further diffracted. The second diffraction causes certain orders to overlap. The +1 order from the -1 beam, and the -1 order from the +1 beam both overlap with the undiffracted order. The three orders come to a common focus after passing through L_3 . It is easy to see from the diagram that the system operates independently of wavelength. Different wavelengths of light will be diffracted different amounts by G_1 , but the dispersion will be compensated at G_2 .

Light diffracted at G_1 comes to three foci in the focal plane of L_1 . If G_1 has grating spacing b, the separation of the foci is $\Delta = \lambda F/b$ where F is the focal length of L_1 . Because these three points originate from the same beam, they are

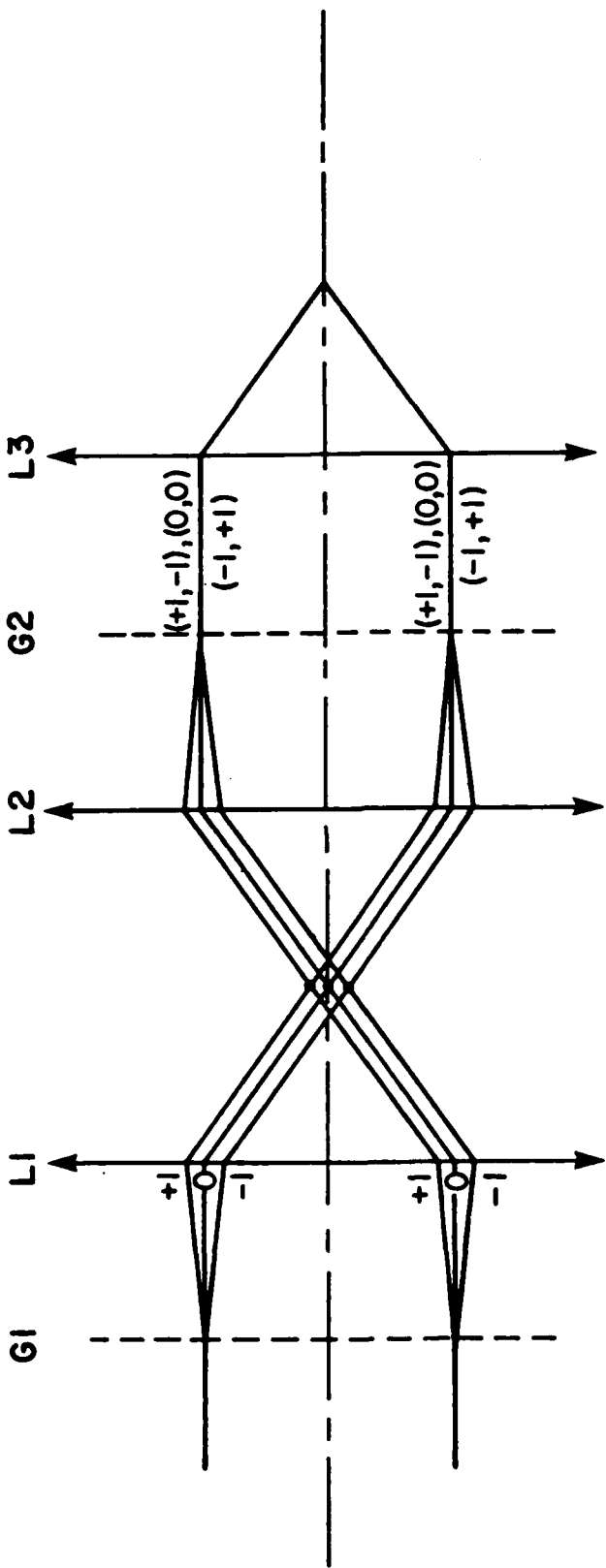


Figure 4. Geometrical Interpretation of the Lau Interferometer.

coherent with respect to each other. This is exactly the conclusion drawn from Equation (7).

The Lau interferometer is a shearing interferometer; that is, it overlaps adjacent points (the foci in Figure 4) in the object. As such it displays the derivative of a phase object. In the absence of any phase disturbance between L_1 and L_2 there is no phase difference between the adjacent foci and no interference is observed in the final plane. A quadratic phase disturbance will cause straight-line fringes to appear in the final plane. Straight-line bias fringes can also be formed by displacing G_1 . If G_1 is moved to some arbitrary distance d in front of lens L_1 , the waves traveling between L_1 and L_2 will no longer be plane but will have quadratic phase fronts. The three foci will now have a quadratic phase relationship between them, and bias fringes will appear in the observations plane. The fringes will be black and white because the interferometer is achromatic.

Unlike a conventional coherent interferometer, the fringes from a Lau interferometer do not have an intuitively obvious interpretation. The interpretation can be aided through analogy with a shearing interferometer and by considering the simple case of bias fringes with no phase object present. Referring to Figure 2, grating G_1 is moved a distance δ (positive or negative) away from the front focal plane of lens L_1 . No phase object is present at plane P. The resulting image in the focal plane of lens L_3 is a set of straight-line fringes (see Figure 6 in Section II.4). A rather complicated analysis of the coherence function shows that the intensity in the final plane consists of a shape function convolved with a set of delta functions, which is indeed a pattern of straight-line fringes. For fringes to occur the spacing b' of grating G_2 must be related to the spacing b of grating G_1 by $b = (F_1/F_2)b'$. In other words, the image of grating G_1 must be the same size as grating G_2 . When this condition is met the fringes occur at

$$x = k \frac{F_3}{F_2} \frac{F_1}{\delta} b \quad (8)$$

where k is an integer. The factor F_3/F_2 is the magnification between plane P and the image plane, which we may ignore for our present purposes.

We wish to relate the spacing x in Equation 8 to the phase front in plane P. A single point (which we consider to be on-axis for simplicity) gives rise to a wavefront represented by $\exp[-i(\pi/\lambda)(\delta/F_1^2)x^2]$ in plane P. Because G_1 is a grating there is another wave which originates at the same point that has a linear phase shift proportional to the grating frequency. The second wave has a phase front at P represented by $\exp[-i(\pi/\lambda)(\delta/F_1^2)(x-\lambda(F_1/b))^2]$ where b is the grating spacing. Other waves are also present from the higher grating diffraction orders, but we may ignore them here.

The grating G_2 overlaps the two waves so that they add coherently in the image plane. The intensity there is

$$\begin{aligned} I(x) &= e^{-i\frac{\pi}{\lambda}\frac{\delta}{F_1^2}x^2} + e^{-i\frac{\pi}{\lambda}\frac{\delta}{F_1^2}(x - \frac{\lambda F_1}{b})^2} \\ &= 2 + 2\cos [2(\frac{\delta}{bF_1}x - \frac{\delta\lambda}{b^2})] . \end{aligned} \quad (9)$$

Each point on G_1 causes a similar fringe pattern, and all the intensities are summed to give the total pattern. The linear phase terms can all be ignored. The maxima of the pattern occur when

$$x = k \frac{F_1}{\delta} b \quad (10)$$

where k is an integer, exactly as in Equation (8).

We have established that Lau interference patterns are analogous to shearing interference patterns; therefore, we may use the standard interpretation of shearing fringes for the Lau interferometer.

An interferogram may be written as $\cos(2\pi\phi(x))$ and a wavefront as $2\pi\omega(x)$. The shearing relationship between ω and ϕ is

$$\frac{\delta\omega}{\delta x} S = \phi(x) \quad (11)$$

where S is the shear. For the Lau interferometer

$$S = \frac{\lambda F}{b} \cdot \quad (12)$$

For the present example we have

$$\begin{aligned} \frac{\delta\omega}{\delta x} \frac{\lambda F_1}{b} &= \frac{\delta}{Fb} x \\ \omega &= \frac{1}{2} \frac{\delta}{F_1^2} x^2 \end{aligned} \quad (13)$$

which is indeed the case for a spherical wavefront. This example also illustrates why the Lau interferometer is achromatic. A phase front varies as λ^{-1} whereas the shear varies directly as λ . Therefore, the wavelength cancels out of Equation (11) and $\phi(x)$ is always independent of wavelength.

4. LAU INTERFEROMETER EXPERIMENTS

A breadboard Lau interferometer was constructed to demonstrate its properties and show its usefulness for wind tunnel measurements. The system was identical to that of Figure 2. The position of G_1 was variable, and a phase object was inserted between lenses L_1 and L_2 . All lenses had 200 mm focal lengths. The gratings both had 50 f/in (2 f/mm) spacing. The light source was a tungsten bulb in a lamp housing with a variable aperture and variable focus condenser lens. The phase object was a small stream of gas obtained through a hypodermic needle attached to a can of freon. A very slight pressure on the gas can's valve produced the phase object.

When aligned, and with no phase disturbance present, the output image has uniform intensity. Close inspection shows the image of the needle to have two ghost images associated with it. These images are a result of imaging through the second grating. Only the $+1$ orders from the grating are evident. If the gratings are moved slightly out of place, large fringes characteristic of the shearing pattern for spherical aberration can be seen. These fringes have some coloration (red on one edge, green on the other). The fringes are the result of residual spherical and chromatic aberrations in the system. Using higher-quality lenses would correct this problem.

Figure 5 shows an image of the gas stream coming from the hypodermic needle. The image is similar to that derived from a schlieren system, which is not surprising since schlieren is also a form of shearing interferometry. The flow is dark along the bottom edge and bright along the top edge, which is what we would expect for the derivative of a flow with cylindrical shape.

If G_1 is moved away from the front focal plane of L_1 , bias fringes appear across the image. Figure 6 shows how the phase disturbance affects the bias fringes. It is easy to make a

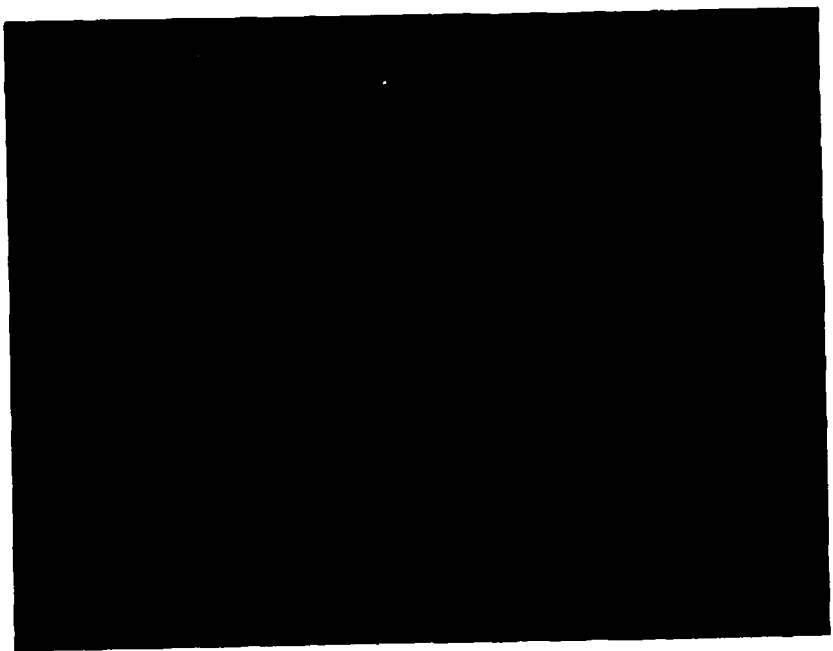


Figure 5. Infinite Fringe Lau Interferogram of a Gas Stream.

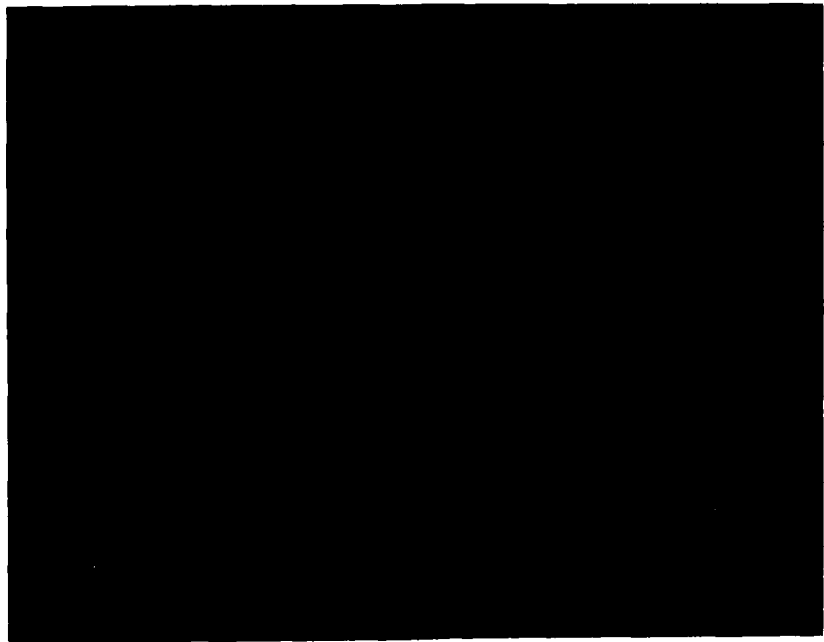


Figure 6. Lau Interferogram of a Gas Stream When Bias Fringes are Added.

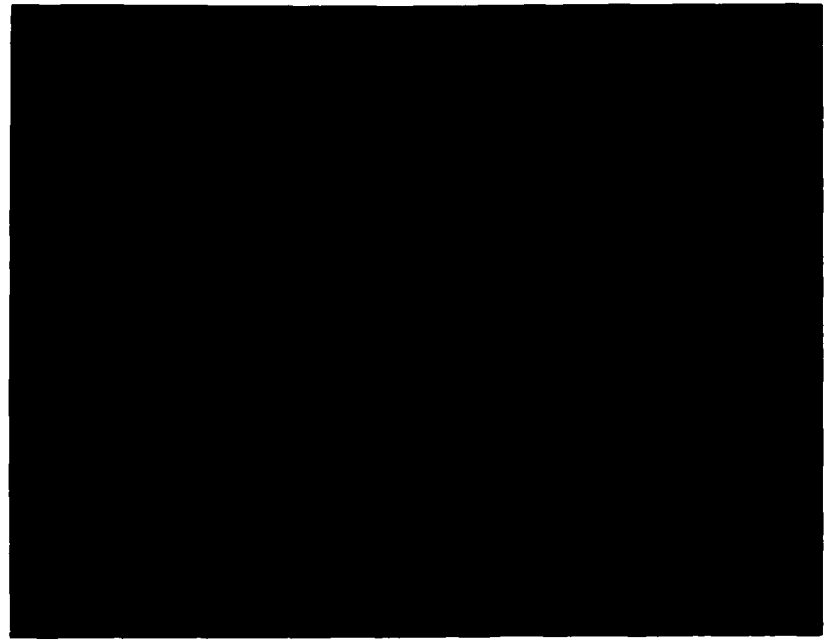


Figure 7. Lau Interferometer of Object Used in Figure 6, but Object Moved Out of the Region of Focus.

qualitative evaluation of the phase flow just from the photograph. It is interesting to note that the bias fringes do not have uniform intensity, but rather appear to be darkest at the edge with a light stripe in the center. The theory of the Lau effect predicts that the interference fringes will have an intensity profile corresponding to the autocorrelation of the grating lines in G_2 . For our experiments G_2 was a Ronchi ruling with square profile lines, so the autocorrelation is a triangle function, just as we observe. The appearance of bias fringes from defocused gratings has never been noted before in the literature.

Figure 4 shows that for interference to occur the gratings G_1 and G_2 must be matched. More specifically, the periodic coherence formation at the plane of the phase disturbance must match the grating G_2 . We see by Equation (7) that if G_1 is defocused ($\alpha \neq 0$) the period of the coherence function changes with the distance away from the focal plane of L_1 . If the phase disturbance moves too far away from the focal plane, the sampling is no longer matched to G_2 and interference no longer occurs. Therefore, the Lau interferometer can be made sensitive to the position of the phase disturbance. Figure 7 shows the same phase disturbance as in Figure 6 moved out of focus. It no longer has an effect on the position of the bias fringes. Its only effect is to reduce the fringe contrast. Of course, we might expect some position-dependent effect just from the nature of an incoherent imaging system. Indeed, if we increase the f/number of the system by stopping down lens L_1 , the depth of focus of L_1 increases and the position-dependent effect is no longer so apparent. However, we can definitely ascribe some position-dependence to the bias fringes. With no bias fringes across the field the phase object is no longer visible after it moves 85 mm from the focal plane. With the bias fringes present the object is no longer visible after a translation of only 35 mm. So the bias fringes have the effect of narrowing the range over which a phase object is visible.

The defocus effect has an interesting implication for wind tunnel applications. Phase disturbances will be visible only within a narrow region. Any other phase variations will not be visible as changes in the bias fringes. They will only reduce the overall fringe contrast. However, a coherent interferometer will integrate the phase over the entire region between L_1 and L_2 . Previous workers have only been concerned with in-focus images in the Lau interferometer. We are the first to describe the position-dependent effects.

To formally establish the interpretation of Lau fringes we used a controlled object from which we could get a known phase front. We wrapped nichrome wire around a glass tube to make a small heating filament. The heated wire is shown in a Mach-Zehnder interferogram in Figure 8. The rod is viewed on end to show the thermal gradient. A Mach-Zehnder interferogram is a direct measure of phase change, so it is easy to see how the thermal gradient decreases with distance away from the rod.

The unheated rod is shown in Figure 9 in the Lau interferometer. The bias fringes are aligned parallel to the rod. When the rod is heated as in Figure 10 the fringes shift to show the thermal gradient. To emphasize the shift we have used a video processor to subtract the images in the heated and unheated states. The fringe shifts near the rod are clearly visible. The wire itself is also visible because it expanded slightly when heated, but this change does not affect the fringe shifts. The fringe shift is large near the rod and becomes smaller further away. The same behavior of the gradient can be deduced from the Mach-Zehnder interferogram. An exact numerical comparison of the interferograms would require an expensive and time-consuming analysis beyond the constraints of the current contract, but the qualitative correspondence between the interferograms is obvious, and we are confident that further work would establish the numerical equivalency.

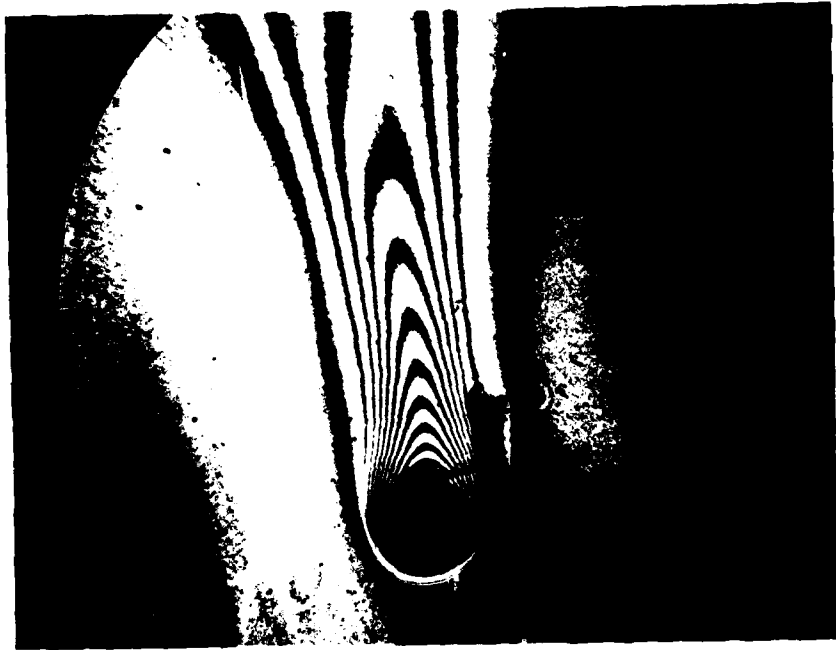


Figure 8. Mach-Zehnder Interferogram of a Thermal Gradient from a Heated Nichrome Wire Wrapped Around a Glass Rod (~ 2 mm diam). The interferogram was taken end on. The thermal gradient is clearly evident.



Figure 9. Lau Interferometer Bias Fringes with Unheated Wire.



Figure 10. Difference Image Obtained by Electronically Subtracting Lau Interferogram of Unheated Object from the Heated Object Interferogram. The shift in the fringe position is clearly evident.

SECTION III

COMBINED LDA/LAU INTERFEROMETER INTERFERANEMOGRAPHY SYSTEM

Combining the 3-D LDA system with the Lau interferometer proceeds in a straightforward manner. The LDA system (as worked out in Appendix A) should be formed from a 2-D LDA system at wavelength λ_1 and a 1-D LDA system at λ_2 combined at +45° and -45° to the normal to the principal flowfield velocity direction. The Lau interferometer can be set up in line along the normal (Figure 11) giving each optical system clear access.

To provide real-time data acquisition the phase shift in the Lau interferometer observation plane S (Figure 11) will need to be measured electronically. The detector must be positioned in the plane S at the location where the LDA volume is focused. To interpret the signal unambiguously, it is necessary that the actual signal intensity be measured, i.e., DC coupled. This can lead to problems resulting from a variation in the light source intensity and/or changes in optical transmission. Therefore, a reference detector should be used to monitor all background fluctuations, and the resulting signals should be ratioed.

Another problem is the 2π phase ambiguity. This can be overcome by dithering the position of G_1 along the plane of the grating. The fringes will vibrate and the relative phase of the vibrator and the AC component of the detector signal will determine the direction of the detected phase change and whether or not a 2π phase transition occurred.

The integrated LDA/Lau interferanemography system will be able to provide real-time data acquisition. Subsequent computer interpretation will be required for both signals. As an added benefit, at the expense of more data channels, additional detectors can be placed in the Lau detection plane, and density data of a more global nature will be available to assist interpretation of the interference pattern.

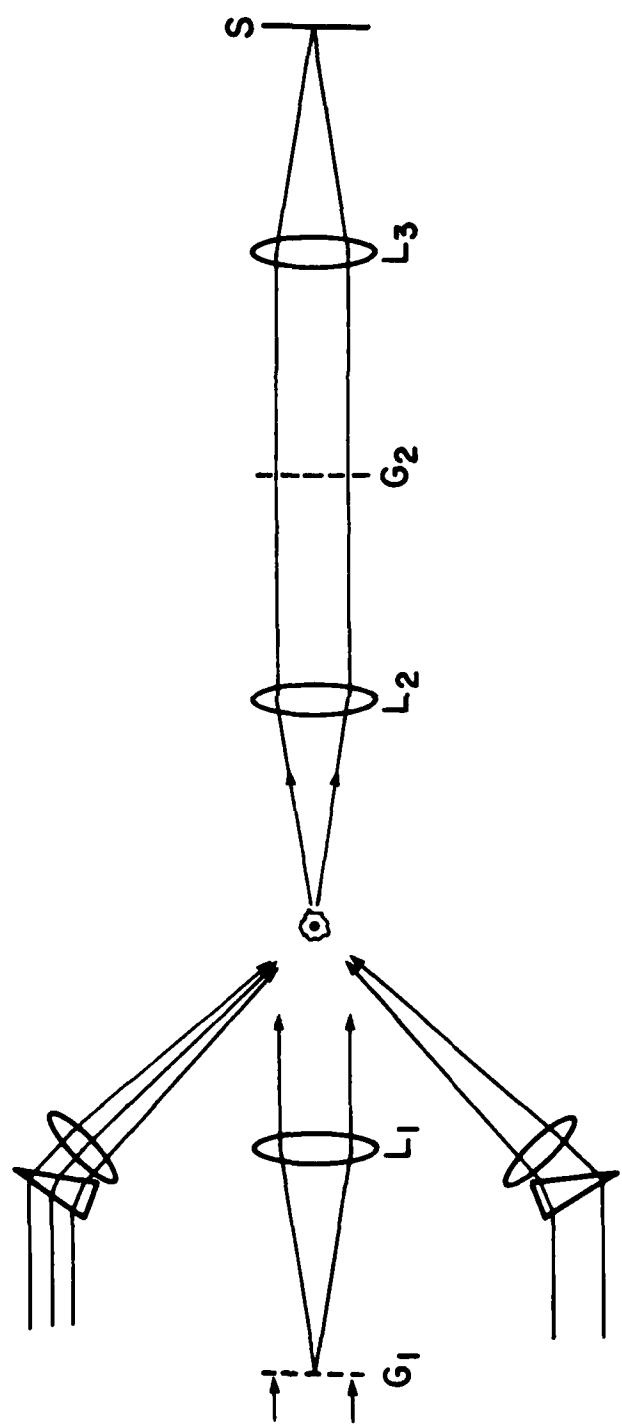


Figure 11. Combined Lau Interferometer and 3-D LDA Systems to Form an Interferonemography System.

SECTION IV SUMMARY AND CONCLUSIONS

The Lau interferometer is a true coherent interference device (as opposed to moire) which needs only incoherent illumination. It has an in-line configuration which uses no beam splitters or spatial filters. It is also extremely stable. (Striking the table with a rubber mallet did not produce any fluctuation in the fringes.)

The Lau is a shearing interferometer, so it presents the derivative of the phase variation. It can be used in either a schlieren mode or with bias fringes to aid in visualizing the phase disturbance. With a low f/number system using bias fringes, the region of phase visualization is limited to the focal region of the first lens. The Lau interferometer is capable of visualizing one plane in a thick phase disturbance.

We must emphasize that our understanding of the Lau interferometer to this point is largely qualitative. To fully understand and apply it an in-depth theoretical and experimental study will be required. Several questions must be answered by this study. The primary objective is interpreting the fringe patterns. They contain derivative information, but the information is not in a simple form. In the configuration used in this study the output consists of three overlapped images, rather than two as in other shearing interferometers. It is also necessary to determine under what conditions a simple fringe interpretation is valid. We anticipate that a weak phase disturbance is required, but that the conditions are influenced by the f/number of the system and the frequency of G_1 . Likewise, these variables affect the depth of focus of the phase imaging.

Along with the theoretical aspects of the interference pattern the engineering aspects of the entire system must also be examined. The choice of gratings is critical to the system.

What happens if radial gratings are used, rather than linear gratings? Previous work⁸ has shown that in classic moire interferometry a phase grating may be used as the second grating. If a thick phase grating is used for G₂, it might eliminate one of the overlapping images, thus simplifying the overall image. Also a large-aperture, low f/number system should be set up, perhaps using reflective optics, to provide a system better suited for wind tunnel work. We feel that a research and development program to address these issues will result in a valuable new tool for wind-tunnel diagnostics.

The LDA system is well in hand. The system is thoroughly understood and the technology required to use LDA is commercially available. The shortcoming with some commercial applications of 3-D systems is in the on-axis velocity resolution. By using the wider angle system, discussed in Appendix A, the system geometry can be tailored to provide the desired performance. The shortcomings, where there are any, tend to be in the data acquisition/signal processing systems and in optical access. Currently, only customized computer systems have the capability to provide the high-speed data-gathering power required for scale length and correlation time measurements.

REFERENCES

1. W. Merzkirch, Flow Visualization, (1974), Academic Press, New York.
2. Max Born and Emil Wolf, Principles of Optics, (1975), Pergamon Press, New York, p. 508.
3. L. Mandel and E. Wolf, "Spectral Coherence and the Concept of Cross-spectral Purity," JOSA 66 (1976), p. 529.
4. Max Born and Emil Wolf, op. cit. p. 499.
5. E. Lau, "Interference Phenomenon on Double Gratings," Ann. der Phys. 6 (1948), p. 417.
6. H. O. Bartelt and J. Jahns, "Interferometry Based on the Lau Effect," Opt. Comm. 30 (1979), p. 268.
7. R. Sudol, "The Lau Effect: An Interference Phenomenon in Partially Coherent Light," Ph.D. Thesis, the University of Rochester (1981), available from University Microfilms.
8. K. Harding and S. Cartwright, "Phase Grating Use in Moire Interferometry," App. Opt. 23 (1984), p. 1517.

APPENDIX

**REAL TIME ON LINE SIMULTANEOUS MEASUREMENTS
OF DENSITY AND VELOCITY IN COMPLEX FLOWS**

TABLE OF CONTENTS

| SECTION | | PAGE |
|---------|--|------|
| A-1 | INTRODUCTION | A-8 |
| A-2 | INTERFEROMETRY MEASUREMENT OF FLOW-FIELD DENSITIES | A-10 |
| A-2.1 | BASIC INTERFEROMETRY FOR FLOW FIELDS | A-11 |
| A-2.2 | INTERFEROMETRIC SENSITIVITIES FOR AFWAL/FI WIND TUNNELS | A-14 |
| A-2.3 | INTERFEROMETRY FOR REAL-TIME MEASUREMENT OF DENSITIES | A-17 |
| | A-2.3.1 Holographic Interferometry | A-17 |
| | A-2.3.1.1 Sources | A-18 |
| | A-2.3.1.2 Recording Material | A-24 |
| | A-2.3.1.3 Interference Pattern Recording and Computer Evaluation | A-26 |
| | A-2.3.2 Point Diffraction Interferometry | A-29 |
| | A-2.3.3 Heterodyne Interferometry | A-32 |
| A-3 | FLOW FIELD VELOCITY MEASUREMENTS | A-34 |
| A-3.1 | LASER DOPPLER ANEMOMETRY | A-37 |
| | A-3.1.1 Downbeating | A-38 |
| | A-3.1.2 "Fringe" Model | A-42 |
| | A-3.1.3 Dual Beam LDA | A-43 |
| | A-3.1.4 Multicomponent Velocity Systems | A-45 |
| | A-3.1.5 Considerations in Practical Application | A-47 |
| | A-3.1.5.1 Coordinate Transformation | A-49 |
| | A-3.1.5.2 Counter-Processor Errors | A-52 |
| | A-3.1.5.3 Data Uncertainty Due to Noise | A-55 |
| | A-3.1.5.4 Statistics Uncertainties | A-57 |
| | A-3.1.5.5 Uncertainties due to Flow Characteristics | A-58 |
| | A-3.1.5.6 LDA Beam Deflection Effects | A-60 |
| | A-3.1.5.7 Seed Influence | A-61 |
| | A-3.1.5.8 Scattering Considerations | A-63 |
| A-3.2 | ALTERNATE TECHNIQUES FOR FLOW FIELD VELOCITY MEASUREMENTS | A-71 |
| A-3.3 | SUMMARY | A-73 |

| | | |
|-------|--------------------------|------|
| A-4 | CONCLUSIONS | A-74 |
| A-4.1 | INTERFEROMETRY | A-74 |
| A-4.2 | LASER DOPPLER ANEMOMETRY | A-75 |
| | REFERENCES | A-77 |
| | SUPPLEMENT TO APPENDIX | A-80 |

LIST OF FIGURES

| FIGURE | | PAGE |
|--------|--|------|
| A-2.1 | Illustration of interferometric view of a general 3-D field. | A-12 |
| A-2.2 | Ray orientation for 2-D axisymmetric field. | A-12 |
| A-2.3 | Holographic interferometric system. | A-19 |
| A-2.4 | The UDRI metal vapor laser characterization setup. | A-23 |
| A-2.5 | Block diagram of developmental fringe analysis system. | A-30 |
| A-2.6 | Schematic diagram of a point diffraction interferometer for wind tunnel applications. | A-31 |
| A-3.1 | Scattering geometry. | A-39 |
| A-3.2 | LDA optical configurations. | A-40 |
| A-3.3 | One-component dual-beam LDA geometry. | A-44 |
| A-3.4 | Component separation schemes for two-dimensional LDA systems using 3-beam and 4-beam optical systems. | A-46 |
| A-3.5a | Schematic of DISA 3-D LDA system. | A-48 |
| A-3.5b | Schematic of TSI 3-D LDA system composed of a 3-beam 2-D frequency separation system, measuring two non-orthogonal velocity components, and a 2-beam 1-D LDA measuring the velocity component orthogonal to the plane of the other two components. | A-48 |
| A-3.6 | Orthogonal reference coordinate frame (X,Y,Z) and LDA coordinate frame (X',Y',Z'). | A-50 |

A-3.7 Relationship of measurement frame and reference frame. A-50

A-3.8 Maximum number of Doppler cycles scattered in the 1-D system analysis. A-56

A-3.9 Uncertainty in assurance that estimate of measured v is within three standard deviations of true v as a function of the local turbulence intensity and the number of independent velocity measurements. A-59

A-3.10 Uncertainty in assurance that estimate of measured TI is within three standard deviations of true TI as a function of the number of independent measurements. A-59

A-3.11 Fidelity of response for seed particles of silicon oil and TiO_2 with diameters of 0.5, 1.0, and 1.5 μm . A-62

A-3.12a Polar plot of scattering intensity for the components polarized parallel and perpendicular to the plane formed by the laser propagation vector and the scattering direction vector, for particles having an index of refraction of 1.47 + 0i and diameters of: (a) 0.5 μm ; (b) 1.0 μm ; (c) 1.5 μm . A-64

A-3.12b Polar plot of scattering intensity for the components polarized parallel and perpendicular to the plane formed by the laser propagation vector and the scattering direction vector, for particles having an index of refraction of 1.47 + 0i and diameters of: (a) 0.5 μm ; (b) 1.0 μm ; and (c) 1.5 μm . A-65

A-3.12c Polar plot of scattering intensity for the components polarized parallel and perpendicular to the lane formed by the laser propagation vector and the scattering direction vector, for particles having an index of refraction of 1.47 + 0i and diameters of: (a) 0.5 μm ; (b) 1.0 μm ; and, (c) 1.5 μm . A-66

A-3.13 Scattering factor as a function of collection angle for Silicone Oil droplets of 0.5, 1.0, and 1.5 μm diameter and a detector collector centered at 165° to the forward LDA optic axis. A-67

A-3.14 LDA signal quality (visibility, pedestal amplitude, and relative Doppler signal to noise ratio) for scatterers with index $1.47 + 0i$ having a radius between $0.1 \mu\text{m}$ and $10 \mu\text{m}$.

A-70

A-A.1 (a) Three beam optical configuration in which (X', Y') plane lies in (X, Y) plane. (b) Commonly employed three-beam configuration where (X', Y') plane does not lie in plane (X, Y) .

A-82

A-A.2 Generalized configuration for beams at crossing-focusing lens.

A-82

LIST OF TABLES

| TABLE | | PAGE |
|--------------|--|-------------|
| A-2.1 | Representative Interferometric Sensitivities for the Wind Tunnel Facilities of AFWAL/FI | A-15 |
| A-2.2 | Potential Laser Sources | A-25 |
| A-2.3 | Holographic Recording Materials | A-27 |
| A-3.1 | Velocity Measurement Summary | A-72 |

SECTION A-1

INTRODUCTION

As part of Contract No. F33615-83-C-3020 the University of Dayton has conducted a study of technologies involved and required for an interferanemography system. The current technologies of interferometry and laser Doppler anemometry were evaluated for their applicability to interferanemographic techniques as well as other techniques such as Rayleigh scattering and holographic mapping of flow-field particles.

The specified requirements for an interferanemographic system are to provide real-time/on-line simultaneous measurements of density and velocity in complex flow fields.

A generally accepted method for measurement of air density is interferometry. Within the past decade holographic interferometric techniques have been used successfully to obtain density data in a variety of wind tunnel studies. However, the general application and wide use of interferometry is hindered in wind tunnel studies by the following: (a) single line-of-sight views of the flow field limit the application to 2-D or 3-D axisymmetric fields; (b) insufficient measurements for optically weak fields (i.e., hypersonic flows or low density flows); (c) manual data reduction methods now widely used.

Laser Doppler techniques have been used to measure velocities in subsonic and supersonic flow fields. Laser Doppler Anemometry (LDA) is a process whereby changes in the frequency (Doppler shifting) of a laser radiation scattered from particles moving through an optical control volume are monitored to compute the velocity of the moving particles. The particles are kept small (0.2 to 1.0 micron in diameter), typically so that their velocities are the same as the local velocity of the fluid stream.

Section A-2 of this report presents a development of the requirements and techniques for interferometric measurements of a general three-dimensional flow field. As a part of the study using interferometry, it was necessary to characterize the interferometer sensitivities for the different wind tunnels at Wright-Patterson Air Force Base, and the results of this comparison are presented in Section A-2.

Section A-3 presents a development of the Laser Doppler Anemometry requirements and techniques for characterization of local velocities in a complex flow field. Alternate techniques for measurement of the local velocities are compared to LDA to see if they offer any advantage over LDA in work by the Flight Dynamics Laboratory.

Section A-4 summarizes the potential of existing technology to obtain real-time/on-line interferanemographic measurements in complex flow fields.

SECTION A-2

INTERFEROMETRY MEASUREMENT OF FLOW-FIELD DENSITIES

Aerodynamic measurements of density using interferometry require the use of optical equipment and processes which are capable of recording and interfering light waves of special character. Several processes involving holography have been developed and used successfully in wind tunnel applications, and these results are documented in the literature. In the present study, the prospects for obtaining real-time interferometric data simultaneously with laser velocimetric measurements are sought. Motivation for the development of this capability comes from an aerodynamic need to be able to measure the perturbation factors comprising the Reynolds shear stresses in air flows. These factors are the perturbations in both the density and velocity.

An important physical condition to understand in the use of interferometry is the fact that the measurable fringe shifts of an interferogram result from a summation of all changes in density along the path traversed by the light waves. This means the values of density calculated from interferometric measurements are path-dependent quantities. Furthermore, unless the flow field is two-dimensional and the optical axis of the interferometer is aligned with the axis of the flow along which the fluid properties are invariant, more than one view of the flow field is required to obtain density data. It is regrettable that this limitation places definite restrictions on the general usefulness of interferometry in wind tunnel applications, because many facilities in use today simply prohibit multiple viewing of the flow.

In response to the present study, a general description of the interferometer process applicable to wind tunnel studies is presented along with a survey on interferometric sensitivities for the specific wind tunnel facilities of the Air Force Wright

Aeronautical Laboratories, Flight Dynamics Laboratory (AFWAL/FI). Also given is a description of a new interferometric technique, Point Diffraction Interferometry (PDI), which appears to be a promising approach to obtaining "real time" interferometric data.

A-2.1 BASIC INTERFEROMETRY FOR FLOW FIELDS

The interference fringes obtained with interferometry are related to the refractive index of the gases in the test section and the reference section by

$$S(x,y,z) = \frac{1}{\lambda} \int f [n(x,y,z) - n_{ref}] dz \quad (A-1)$$

where $S(x,y,z)$ is the measurable fringe shift, λ is the wavelength of the light and $n(x,y,z) - n_{ref}$ is the relative change in refractive index.

For gases, the index of refraction is related to density through the Dale Gladstone constant K_{DG} as,

$$K_{DG} = \frac{n(x,y,z)-1}{p(x,y,z)} . \quad (A-2)$$

Therefore, Equation (A-1) becomes

$$S(x,y,z) = G \int f(x,y,z) dz \quad (A-3)$$

where

$$G = \frac{K_{DG}}{p_{ref} \lambda} \quad (A-4)$$

is a constant, and

$$f(x,y,z) = \frac{\rho(x,y,z)}{\rho_{ref}} - 1 . \quad (A-5)$$

Equation (A-3) is difficult to resolve because the integrand, $f(x,y,z)$, depends on three spatial coordinates (see Figure A-2.1). When applied to a plane, $x = x_c$ where x_c denotes a constant, the dependence is reduced to two variables and Equation (A-3) becomes

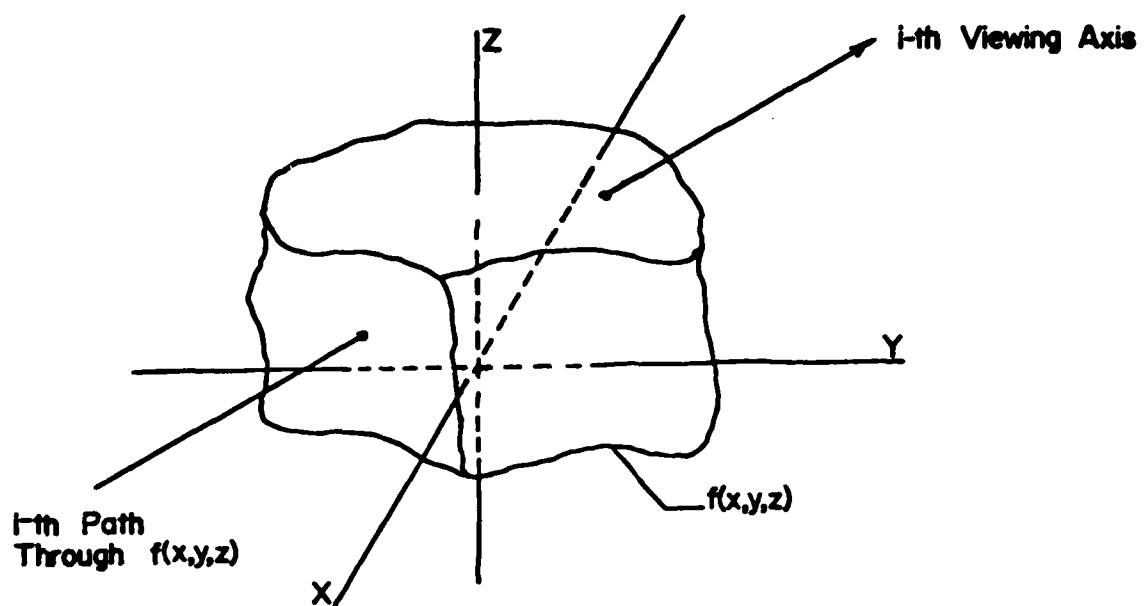


Figure A-2.1 Illustration of interferometric view of a general 3-D field.

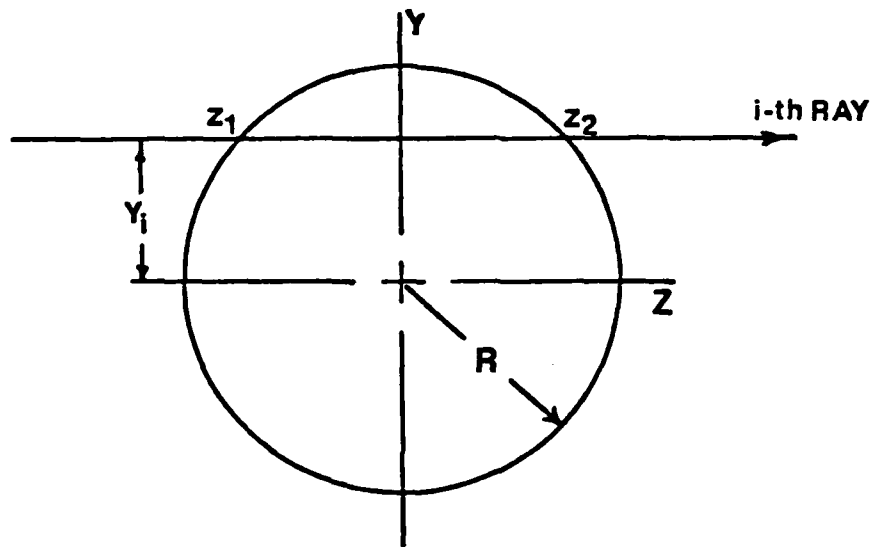


Figure A-2.2 Ray orientation for 2-D axisymmetric field.

$$S(y, z) = G \int_1 f(y, z) d1 . \quad (A-6)$$

No further general simplification is possible except for cases where the flow field is either 2-D or 3-D axisymmetric. For these cases

$$S(y) = G [f(y)]L \quad (2-D) \quad (A-7)$$

$$S(y) = G \int_y^R \frac{2f(r)}{\sqrt{r^2 - y^2}} r dr \quad (3-D \text{ axisymmetric}) \quad (A-8)$$

(See Figure A-2.2)

The density is obtained by solving these relationships for the density function. This results in

$$\rho(y) = \frac{S(y)}{GL} + \rho_{ref} \quad (2-D) \quad (A-9)$$

and

$$\rho(r) = -\frac{1}{\pi G} \int_r^R \frac{ds(y)/dy}{\sqrt{y^2 - r^2}} dy + \rho_{ref} \quad (3-D \text{ axisymmetric}). \quad (A-10)$$

For asymmetric fields, a general solution to the basic equation does not exist. Instead, multiple views of the field are required in conjunction with the use of special transformations. For steady flows, rotation of the model can be used to obtain multiple views, thereby permitting computation of the density from the optical data. However, for unsteady flows, the model rotation technique is not truly accurate, and results in considerable uncertainty in the data. Exact solutions are possible when the field is viewed over 180 degrees in increments of approximately 5 to 8 degrees. Smaller viewing ranges can be used (generally not less than 90 degrees), but error is inherent in these results.

A-2.2 INTERFEROMETRIC SENSITIVITIES FOR AFWAL/FI WIND TUNNELS

As a means of evaluating interferometric measuring capabilities in the AFWAL/FI wind tunnels, the interferometric sensitivity is used to estimate representative fringe shift magnitudes. These results are presented in Table A-2.1. Since the length factor in the interferometric integral equation varies from one application to another, an interferometric sensitivity per unit length is,

$$\phi(y) = \frac{S(y)}{f(y)L} = \frac{K_{DG} P_{\infty}}{\lambda} \quad (A-11)$$

For the present evaluation, the reference density is

$$P_{\infty} = \frac{P_{\infty 0}}{RT_{\infty 0}} = \frac{P_0}{RT_0} N_1 + \frac{\gamma-1}{2} M_{\infty 0}^2 0^{-\frac{1}{\gamma-1}}$$

assuming isentropic flow from the wind tunnel nozzle to the test rhombus. The zero subscripts denote the total state, and R, γ and $M_{\infty 0}$ are, respectively, 287 J/Kg-°K, the ratio of specific heats = 1.4, the free stream mach number; K_{DG} and λ are the same values as previously reported. For wind tunnel facilities of reasonably constant T_0 and fixed $M_{\infty 0}$, variation of the total pressure is seen to directly affect the interferometric sensitivity; the order of magnitude spread for the Mach 3 facility illustrates this effect.

To better compare the interferometric measuring capabilities of these facilities, a 15-cm length is used to obtain the actual interferometric sensitivities. These results occur, for example, if a 15-cm wide flat plate model were tested in each of the facilities. Finally, the most important result, the actual fringe shifts, are shown in the far-right column of Table 2.1. Note that the results for the 4-in. HWT are parenthesized, because a 15-cm model can not be tested in this facility.

The fringe shifts presented in Table A-2.1 are based upon the magnitude of the density change across a two-dimensional tur-

TABLE A-2.1

REPRESENTATIVE INTERFEROMETRIC SENSITIVITIES FOR THE WIND TUNNEL FACILITIES OF AFWAL/FI

| Facility | P ₀ min | P ₀ max (kPa) | T ₀ (K) | Mach No | Φ (per cm) min. | Φ (per cm) max. | Φ(15 cm length) min | Φ(15 cm length) max | Fringe Shift (2D B.L.) min | Fringe Shift (2D B.L.) max |
|---------------|-----------------------|--------------------------------|--------------------|------------|--------------------|--------------------|------------------------|------------------------|----------------------------------|----------------------------------|
| 1. Mach 3 | 414 | 4,140 | 239 | 3 | 1.49 | 14.89 | 22.4 | 223 | 14 | 140 |
| 2. Mach 6 | 5,516 | 15,514 | 583 | 6 | .56 | 1.56 | 8.4 | 23.4 | 7.4 | 20.6 |
| 3. TGF | | | | | | | | | | |
| a. subsonic | 17 | 294 | .23 | .63 | | | 9.5 | | .09 | |
| | | | .85 | .46 | | | 6.9 | | .81 | |
| b. transonic | 67 | 294 | .3 | 2.46 | | | 36.9 | | .60 | |
| | | | 1.0 | 1.63 | | | 24.5 | | 3.78 | |
| c. supersonic | 29 | 294 | 1.5 | .44 | | | 6.6 | | 1.93 | |
| | | | 3.0 | .08 | | | 1.2 | | .80 | |
| | 48 | 294 | 1.5 | .72 | | | 10.8 | | 3.17 | |
| | | | 3.0 | 15 | | | 2.3 | | 1.36 | |
| 4. 20 in HWT | 17,238 | 1,222 | 4 | 4.40 | | | 66.0 | | 49.73 | |
| | | | 12 | .03 | | | .5 | | .48 | |
| 5. 4 in HWT | 17,238 | 1,222 | 12 | .03 | | | (.5) | | (.48) | |
| | | | 16 | .01 | | | (.2) | | (.16) | |
| 6. 9 in SAW | 448 | 250 | .5 | 17.91 | | | 268.7 | | 11.71 | |
| | | | 1.2 | 10.74 | | | 161.1 | | 33.76 | |

bulent boundary layer on a flat plate. The span of the plate is considered to be 15 cm, and the plate is assumed to be at zero angle of attack in the uniform steady flow air stream of the test rhombus. For this situation, the density function is

$$f(y) = 1 - \frac{\rho_w}{\rho_\infty} = 1 - \frac{T_\infty}{T_w}$$

since the static pressure variation through the boundary layer is constant. The static wall temperature, T_w , varies with time as the model remains in the flow. Depending on the heat transfer rates, the wall condition could reach an adiabatic wall state, at which time

$$T_w = T_{AW} = T_\infty N_1 + r_c \frac{\gamma-1}{2} M_\infty^2$$

where r_c is the recovery factor,

$$r_c = (\text{Prandtl No.})^{1/3} Z .9$$

for turbulent air flow. Therefore, assuming the adiabatic wall condition exists, the density function becomes

$$f(y) = 1 - \frac{1}{1+r_c \frac{\gamma-1}{2} M_\infty^2} .$$

The usefulness of these results is apparent in Table A-2.1. Both high Reynolds number facilities (Mach 3 and 6 wind tunnels) appear good for interferometric studies, the TGF is marginally good for transonic and supersonic studies, and the hypersonic facilities are essentially no good for interferometric measurements. The fringe shifts (49.73 and 33.76) of the 20-in. HWT and the 9-in. SAW are too high and would probably result in a general lack of fringe distinction.

As previously mentioned, the field width, L , is an important factor in computing interferometric sensitivity and the

corresponding fringe shifts, and the 15-cm length of these results serves only as a basis for comparison. One notices that as L decreases, the fringe shift diminishes, and in fact it becomes small even for the high density flows of the Mach 3 and 6 facilities when L is on the order of a few millimeters. This might be true for boundary layer studies on cone or cylinder models.

A-2.3 INTERFEROMETRY FOR REAL-TIME MEASUREMENT OF DENSITIES

Present work in interferometry at the Flight Dynamics Laboratory is not capable of providing real-time density measurements for flow analysis in the study of dynamic events. At this time the interference patterns are recorded during a test and then evaluated in a non-real-time mode using manual data reduction techniques.

As shown in Section A-2.1, if interferometry is used to evaluate density profiles in complex asymmetric flows, multiple views of the field must be recorded. In order to record and evaluate in real-time density profiles using interferometry, an instrument is required that includes the following components:

1. Interferometer Illumination Source,
2. Interferometric Device,
3. Interference Pattern Recording System,
4. Interference Pattern Evaluation System,
5. Algorithms for Determination of Densities,

It was originally proposed that holographic interferometric techniques would be evaluated for its feasibility to be integrated into an interferanemographic system.

A-2.3.1 Holographic Interferometry

A hologram is a photographic recording of a coherent object wavefront and a reference wavefront. When a processed hologram

is reilluminated by the reference wavefront, the hologram will diffract the light in the reference beam and reproduce an exact replica of the object wavefront. After reconstruction, the reconstructed wavefront of the flow field can be used for study of the flow field. By using a pulsed laser source to record the hologram, the record freezes in time a picture of the flow field as it existed during the laser exposure time. With laser pulses of 50 ns or less the temporal variations of the flow field can be observed. By comparing a time history of the interference between the object wavefront and a reconstruction of the object wavefront as it existed in some reference state, quantitative information can be obtained of the temporal variations in the gas densities of a flow field. Figure A-2.3 shows a schematic drawing of a candidate holographic interferometer system for use in studying flow fields. Optical windows are used to provide optical access to the test region. For real-time evaluation of the interference pattern between a reconstructed reference object wavefront and the object wavefront during a test, a television camera would be used to view the real-time interference pattern. The laser source would be pulsed in sequence with the 30-Hz television frame rate, and the digitized interference pattern from the television camera would be evaluated to obtain the gas densities as explained in Section A-2.1.

A-2.3.1.1 Sources

Although a pulsed laser would not be required to record the reference object wavefront, it will be necessary for real-time evaluation during a test run. The pulse length of the laser must be short enough to freeze the temporal effects and have good enough coherence and beam quality to maintain a well-behaved coherent wavefront through the flow field volume relative to the reference beam. To obtain good historical information of a flow field in a dynamic flow requires a laser source with the short pulses of a Q-switched ruby laser and the versatility and continuous, adjustable repetition rate capabilities of a modulated

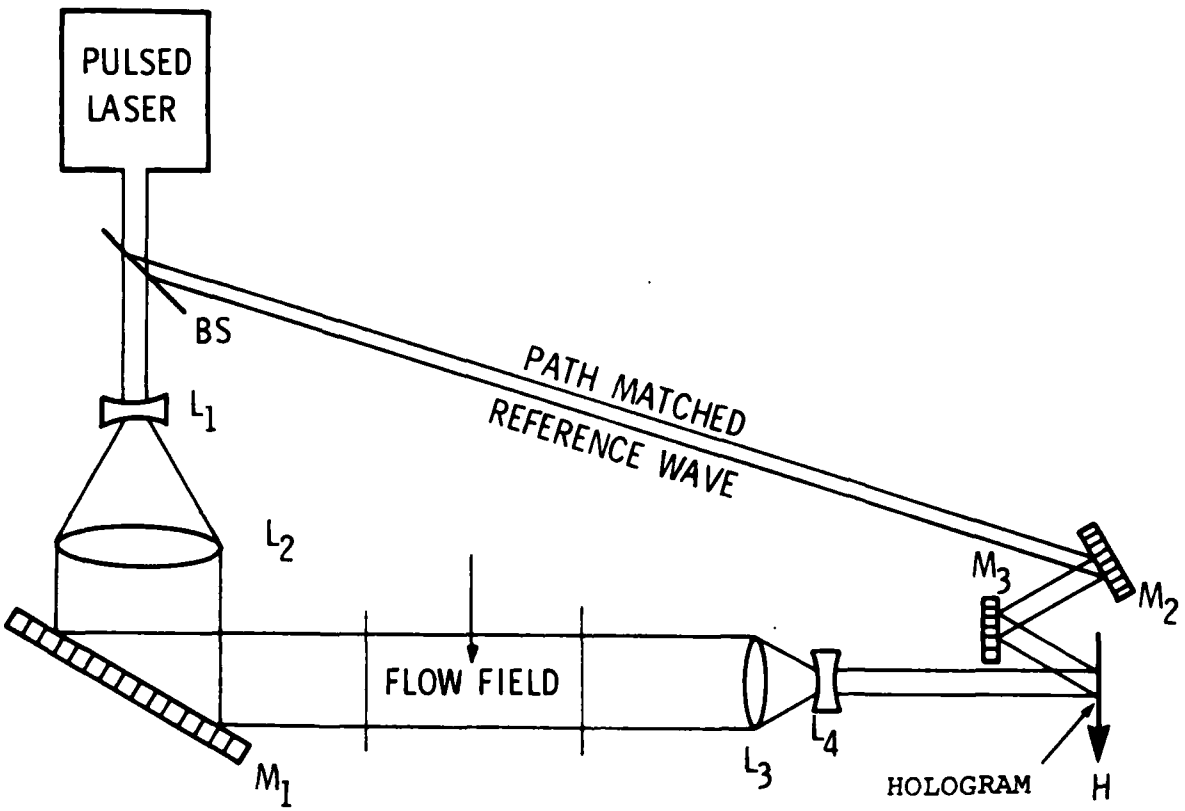


Figure A-2.3 Holographic interferometric system.

argon laser. The two most likely sources available are an excimer laser pumped dye and a metal vapor laser. A standalone excimer laser is not a usable source because of the very high transverse mode character of the beam. Multiple transverse modes will tend to scramble the coherence of the beam across the field, making holography difficult if not impossible.

Excimer lasers emit only in the ultraviolet, have no spatial coherence, and are limited to 500 Hz, although the pulse energies are high (100 to 200 mJ) and the pulse length is short (20 nsec). The excimer laser could be converted to a usable light source by using it to pump a dye laser. By pumping a dye laser with an excimer laser, the short, high-repetition pulse of light of the excimer can be maintained while potentially increasing the coherence of the beam through the properties of the dye. The dye laser will emit at many wavelengths through the visible spectrum and can be restricted to give a good coherence length. The pulse energy with an excimer pumped dye is an order of magnitude less than the excimer alone (10 to 30 mJ) and the pulse length is still very short.

Because it is a new laser system, there is not very much experimental data on the beam quality and coherence produced by combining the unacceptable excimer beam with the well-behaved dye laser medium. Pulse repetition rates are also somewhat limited at this time (about 500 Hz) although higher rates with sufficient energy will probably be available in the future. The cost of these systems is currently high (\$60 K to \$80 K), because of the two lasers required. The physical size of these systems is also quite large, requiring an area about 4 m by 1 m by 1 m. If lower repetition rates are acceptable, Molelectron Corporation produces a lower cost, compact design system.

There are a number of other possible lower cost lasers that provide lower repetition rates. A dye laser alone has a much longer pulse length than an excimer (up to 500 nsec) but is

limited in repetition rates to under 50 Hz. If high energies (over 100 mJ) are required, dye lasers are limited to under 10 Hz. A dye laser is adequate when viewing with a video system (which limits the repetition rate to 30 Hz because of the video frame rate), and they are low in cost (typically under \$20 K from Candella Corp.). Frequency-doubled, electro-optically Q-switched Nd:YAG will put out the same energy as the dye laser in a much shorter pulse (15 nsec) but it is currently limited to 30 Hz repetition rates and it costs twice as much as a dye laser. A program is underway with NASA/Lewis attempting to push this repetition rate up for the Nd:YAG lasers so that it is suitable for combustion diagnostic applications.

The Alexandrite laser can produce energies similar to those of the dye laser (100 mJ) with a shorter pulse length but at only slightly higher repetition rates (40 Hz). Because of the higher cost and limited coherence properties of the Alexandrite laser it is not as attractive an option as the dye laser.

Frequency-doubled, acousto-optically Q-switched Nd:YAG will operate at repetition rates up to 50 kHz with a 200 nsec pulse length, but at pulse energies of less than 5 mJ. There has been very little work done with frequency-doubled, Nd:YAG acousto-optically Q-switched, so the stability and coherence properties are not well characterized. It is very likely that with development work a higher energy, better controlled frequency-doubled, acousto-optically Q-switched Nd:YAG could be built. The laser would need to use amplifier systems and feedback circuitry which would make it fairly expensive. Nd:YAG technology is well established though, and it is a reasonably reliable system. The primary limitation of the acousto-optically Q-switched Nd:YAG would be its long pulse length which would limit its application in holographic recording.

The repetition rate capability of the laser system will directly affect the measurement and mapping accuracy of a particle system.

A metal vapor laser system is reliable and self-contained, and it has greater versatility than the excimer systems. In addition to its having a good working coherence length, by using an externally heated system the University of Dayton has shown¹ that the metal vapor laser can be prompted to pulse at low rates of a few Hz to around 5 kHz with the potential of operating up to 50 kHz in short bursts. The synchronizing electronics for such a system is similar to that used for the strobbed argon laser developed by the University of Dayton Research Institute (UDRI).²

The metal vapor laser is a system with properties similar to those of the acousto-optically Q-switched, frequency-doubled Nd:YAG in terms of repetition rate and scalability of pulse energy but with a much shorter (25 nsec) pulse length and better inherent coherence and stability properties. We evaluated the manganese metal vapor laser with a UDRI-built breadboard laser shown in Figure A-2.4. Initial studies with this laser indicate that it can be built to operate at 1 Hz up to a few hundred Hz continuous and operated in long bursts of perhaps 100 pulses up to 10 kHz and potentially up to 50 kHz. The pulse length is still very short and the coherence length is greater than 5 cm. The breadboard laser put out over 100 μ J per pulse. A larger copper laser can output up to 12 mJ with current designs (larger systems are also possible). For a self-heated metal vapor laser, the metal temperature is not dependent on a high repetition rate to sustain operation. Therefore, the laser can be cued to operate from single pulse to a few hundred or a thousand Hz. This is currently the only laser of this type available with a pulse length on the order of 20 to 40 nsec. The pulse energy, coherence, and stability exhibited by this system are superior to those of any comparable laser system at this time.

As with many newer types of lasers (dyes, excimers, etc.), the metal vapor laser is a high-maintenance item; the laser must be replaced or recycled regularly. The warmup time required has also been viewed as a drawback. Originally, a long warmup time

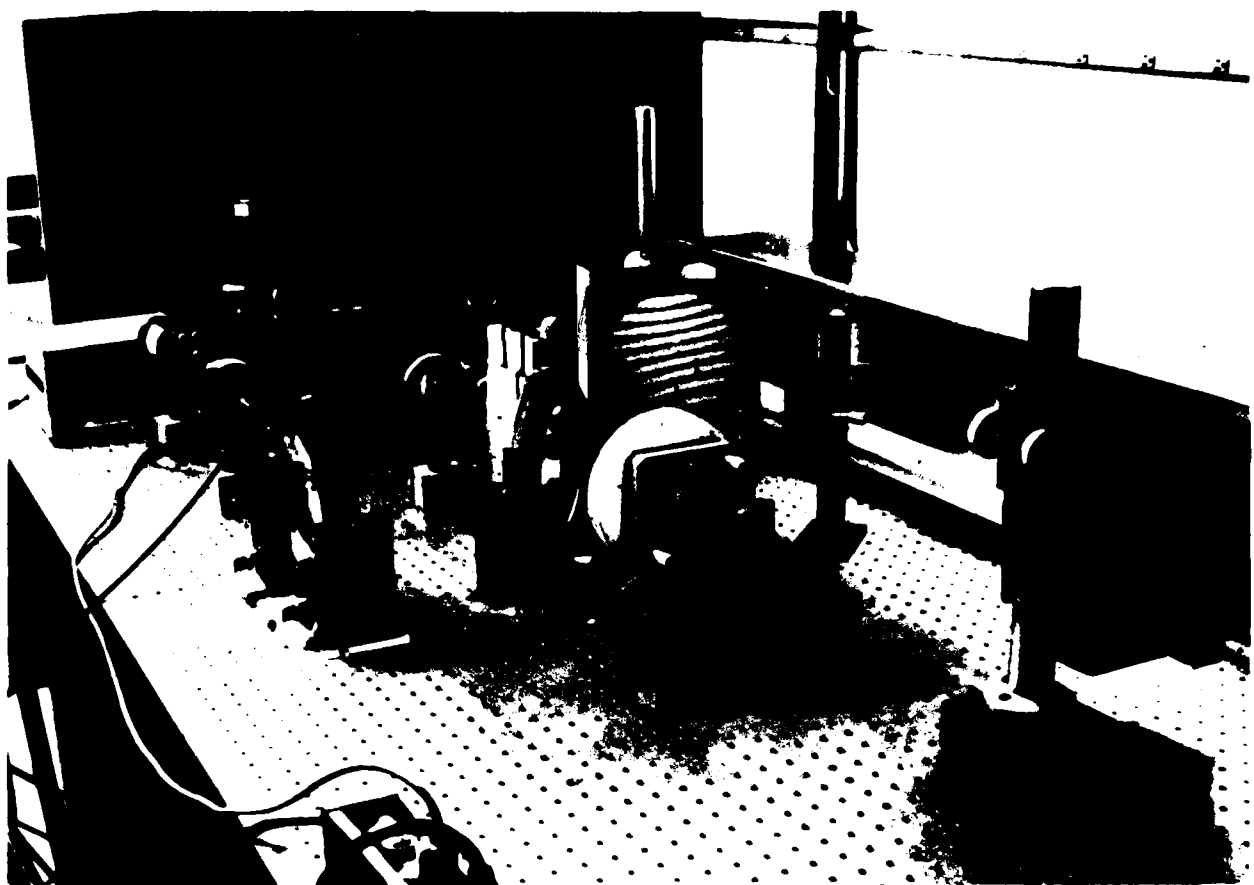


Figure A-2.4 The UDRI metal vapor laser characterization setup.

was necessary to reduce the chance of tube breakage. A new tube design may eliminate this requirement (which is currently required by most commercial metal vapor lasers). The warmup time of the breadboard laser was found to be 1-1/2 to 2 hours.

Due to the low average power of the breadboard system (about 10 mw, primarily unpolarized) this particular system may not be practical as a source for making holograms of large volumes. However, even this breadboard laser produces more energy per pulse than an argon laser at the pulse length which seemed desirable to freeze dynamic vibrations of a few hundred Hz (typically 100 to 200)sec with the argon laser). It will be possible to make a hologram of a field using a metal vapor laser, then view the reconstruction with a small argon laser (which is very long-lived and has low maintenance).

Table A-2.2 reviews the potential lasers for holographic flow studies based upon discussions with manufacturers and University of Dayton experience. The pulse energy required will depend on the type of film used to make the hologram. For typical exposures this is likely to be less than 1 mJ. To record the hologram it is also necessary to have a coherence length sufficient to cover all path length variations such as the marginal rays going through the edge of the collection lens or due to the tilt of the reference beam. For practical application, that would imply a coherence length of 5 cm or greater (a linewidth of 0.0035 nm or less). From Table A-2.2 it is seen that several existing lasers are suitable, and the actual laser selected would be determined by the budget and the measurements to be made.

A-2.3.1.2 Recording Material

An important factor which will affect the quality of a hologram and dictate the laser pulse energy required is the film used to record the hologram. There are a number of different emulsions available on film and plates, notably from Kodak and

TABLE A-2.2
POTENTIAL LASER SOURCES

| LASER | Pulse Width | Energy Per Pulse | Repetition Rate | Coherence Properties | Wavelength Comments | Cost |
|-------------------------------|----------------------------------|---|---------------------------------------|---------------------------------------|--------------------------------|------------------|
| Metal Vapor | 25 nsec | 0.1-12 mJ | 1 Hz-1 kHz continuous to 50 kHz burst | 5-20 cm | 530 nm or 510 nm | \$20 K - \$40 K |
| Strobed Argon | 1 μ sec-DC (500 nsec usable) | Width (AC energy) (at 500 μ sec 0.8 mJ) | DC - 10 kHz | 1 cm, 2 meters with power less of 40% | 514 nm | \$35 K |
| Excimer | 15-20 nsec | 100-200 mJ | 500 Hz max. (100 Hz typ.) | not spatially coherent | UV 250-250 nm only | \$40 K |
| Dye Laser Excimer pumped | 4 nsec | 10-30 mJ | 500 Hz max. (100 Hz typ.) | >40 cm | 380-550 nm tunable | \$55 K - \$70 K |
| Dye Laser Nd:YAG - pumped | 12 nsec | 20-40 mJ | 20 Hz | >40 cm | 550-760 nm tunable | \$50-60 |
| Dye Laser, Flashlamp pumped | 300-500 nsec | 120 mJ at 10 Hz 10 mJ at 50 Hz | 10-50 Hz | >10 cm | 350-700 nm tunable | \$16 K |
| Double Nd:YAG E-O, Q-Switched | 15 nsec | 150 mJ | 10-30 Hz | >20 cm | 532 nm | \$40 K |
| Double Nd:YAG A-O, Strobed | 150-200 nsec | 5 mJ at 1 kHz (10% stability) | 100 Hz-50 kHz | >10 cm ? | 532 nm | \$30 K |
| Alexandrite | 100 nsec | 100 mJ | 1-40 Hz | 1-10 cm ? | 730-775 nm (OK for video) | \$80 K - \$120 K |
| Ruby | 40 nsec | To 4J Typ. | 0.1 Hz | >10 cm | 6943 nm not usable for viewing | \$30 K - \$80 K |

Agfa-Gavaert, which are capable of recording a hologram. These films vary in sensitivity and, inversely, in resolution. These films are summarized in Table A-2.3. The speed of any of these films can be increased by a factor of 3 to 10 by preprocessing the film, either by pre-exposing it with a clean uniform beam or by predeveloping (except for the Laser Technology film which is already preprocessed). This preprocessing typically will not affect the quality of the hologram (since the entire emulsion is affected uniformly) but may reduce the efficiency of the hologram by reducing the contrast of the recording. A lower-contrast hologram will be less noisy than a high-contrast hologram since a high-contrast hologram will accentuate every light variation, like turning up the contrast on a video system.

The Laser Technology film is effectively already preprocessed since it is exposed wet. When we spoke with Laser Technology regarding this application, they mentioned that their holograms are typically fairly noisy due to the very active developer they use. Their process is oriented toward fast developing of holograms primarily for field applications.

A-2.3.1.3 Interference Pattern Recording and Computer Evaluation

To obtain real-time measurements of the flow-field density distribution a television camera would observe the real-time interference pattern, and the digitized video image would be computer analyzed to determine the fringe pattern. The interference fringe pattern information would then be used to calculate the refractive index and density variations through the flow field.

Software requirements for processing the image of a fringe pattern start with the utility routines needed to control the image digitizer and then transfer the digitized image into memory and finally, if desired, to the display screen. Other utility routines are needed to enhance the contrast, zoom in on a selected section of the image, mask out defects, and perform other elementary image-processing functions.

TABLE A-2.3
HOLOGRAPHIC RECORDING MATERIALS

| <u>Material</u> | <u>Base</u> | <u>Sensitivity in Green/cm² (Density = 1)</u> | <u>Resolution</u> | <u>(Gamma) Contrast</u> |
|-------------------------|-------------|--|-------------------|-----------------------------|
| Kodak | | | | |
| 649.F | plate | 800 ergs | 2000 + | 5 |
| SO-343 | film | 1000 ergs | 2000 + | 5 |
| 120-02 | plate | 500 ergs | 2000 + | 5 |
| SO-173 | film | 500 ergs | 2000 + | 4 |
| Minicard II | | | | |
| SO-424 | film | 50 ergs | 1250 | 4 |
| 131-101 | plate | 30 ergs | 1250 | 7 |
| SO-253 | film | 30 ergs | 1250 | 7 |
| Agfa-Gavaert | | | | |
| 8E56HD-AHI | plate/film | 350 ergs | 2500 + | 4 |
| 8E75HD | plate/film | 800 ergs | 2500 + | 3 |
| 10E56 | plate/film | 20 ergs | 1500 | 7 |
| 10E75 | plate/film | 120 ergs | 1500 | 4 |
| Laser Technology | | | | |
| Wet processing film | | 8 ergs | 2000 + | 4 |
| Laser test film | | (red tested) | | |

The next task is to match the image to the important features of the flow field area and test part. The coordinate system of the digitized image must be made to correspond to the actual object space. This is done by manually identifying key features, such as corners of objects or external fiducial marks, whose location in object space is known. Software will be provided to outline the shape of any test fixtures in the image. This gives the operator positive assurance of the accuracy of the coordinate transformation so that he may halt the analysis process at that point if the display does not look right.

An interactive setup dialogue is the best approach for the learning phase of the system to define the shapes of test fixtures and models. The result is a data file that can be used to identify and measure flow fields around the model in a test. An operator may be required to locate these features on each image. Simple geometric models can be defined, so that this identification procedure will require only a few seconds of work with a cursor.

Locating fringe centers is difficult, and no one algorithm is suited for all types of fringe patterns. Over uniform or background regions of the image, the fringes may be straight and evenly spaced. A coarse scan across the image, with large steps between scans, may provide enough information to describe the model geometry in these regions by a low-order polynomial approximation. These regions may be digitized rapidly. In some regions of the image the fringe pattern may be complex and low in contrast. Such regions require high-resolution but relatively slow fringe-following techniques. In highly complex areas of the image, the software can enlarge the region of interest and label locations of known fringes. For high-resolution measurement applications, an operator may be required to untangle the pattern manually with the use of a joystick or digitizing tablet. The computer can assist by modifying the display in response to operator commands.

Once fringe centers have been located, a final data file is prepared and saved for analysis. Absolute model measurement requires that full complexed fringe data be obtained and analyzed for all areas of interest. If a difference fringe pattern is created to show only deviations from the master part, this analysis can be made much simpler. It is thought that the time required for evaluation of a single interference pattern would be about 2 minutes. The cost and details of this type of system will be presented to the Air Force when desired. A conceptual diagram of a developmental fringe analysis system is shown in Figure A-2.5.

A-2.3.2 Point Diffraction Interferometry

A relatively new method for obtaining interferometric data of flow fields involves the use of Point Diffraction Interferometry (PDI). First reported by Smartt in 1975,³ PDI offers the use of a single-pass, relatively vibration-free interferometer that could be used for continuous surveillance of the changes in the optical path lengths of light waves traversing the flow. Unlike interferometers of the usual type, PDI is easier to use, because only one light beam is required to make the measurements, and while not yet done, application to wind-tunnel testing using conventional schlieren optical systems seems appropriate.

In the conceptual use of a wind tunnel PDI, a beam of coherent light passes through the test section of the tunnel using an optical scheme comparable to a Toepler schlieren system. Once the beam is captured by the second schlieren mirror (or lens), the light waves are directed into the PDI. As illustrated in Figure A-2.6, the optical components of the PDI resemble those of a conventional Mach Zehnder interferometer. One set of light waves passes through one path of the interferometer unaltered while the other set is focused and filtered similarly to the way coherent radiation can be spatially filtered so as to transmit selected bands of diffracted radiation. Here, the filtering is

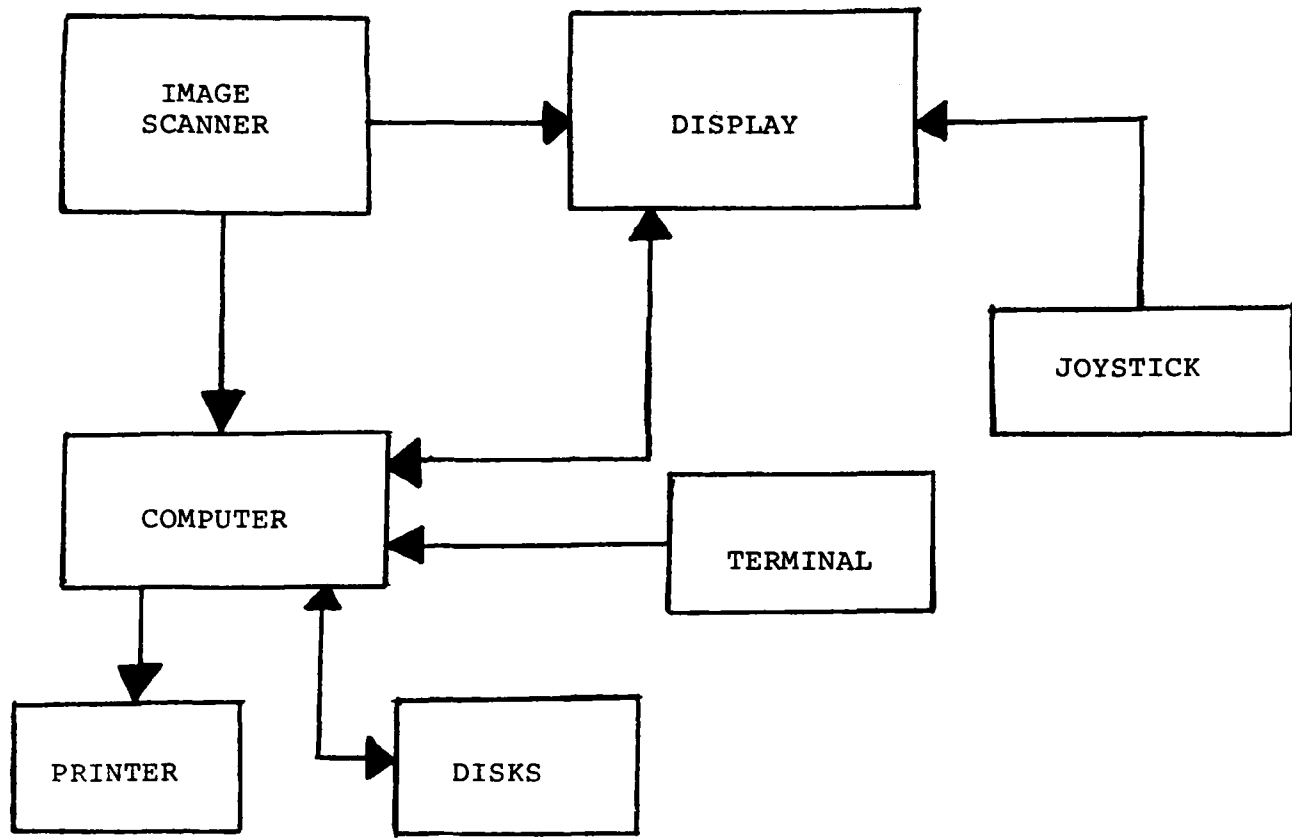


Figure A-2.5 Block diagram of developmental fringe analysis system.

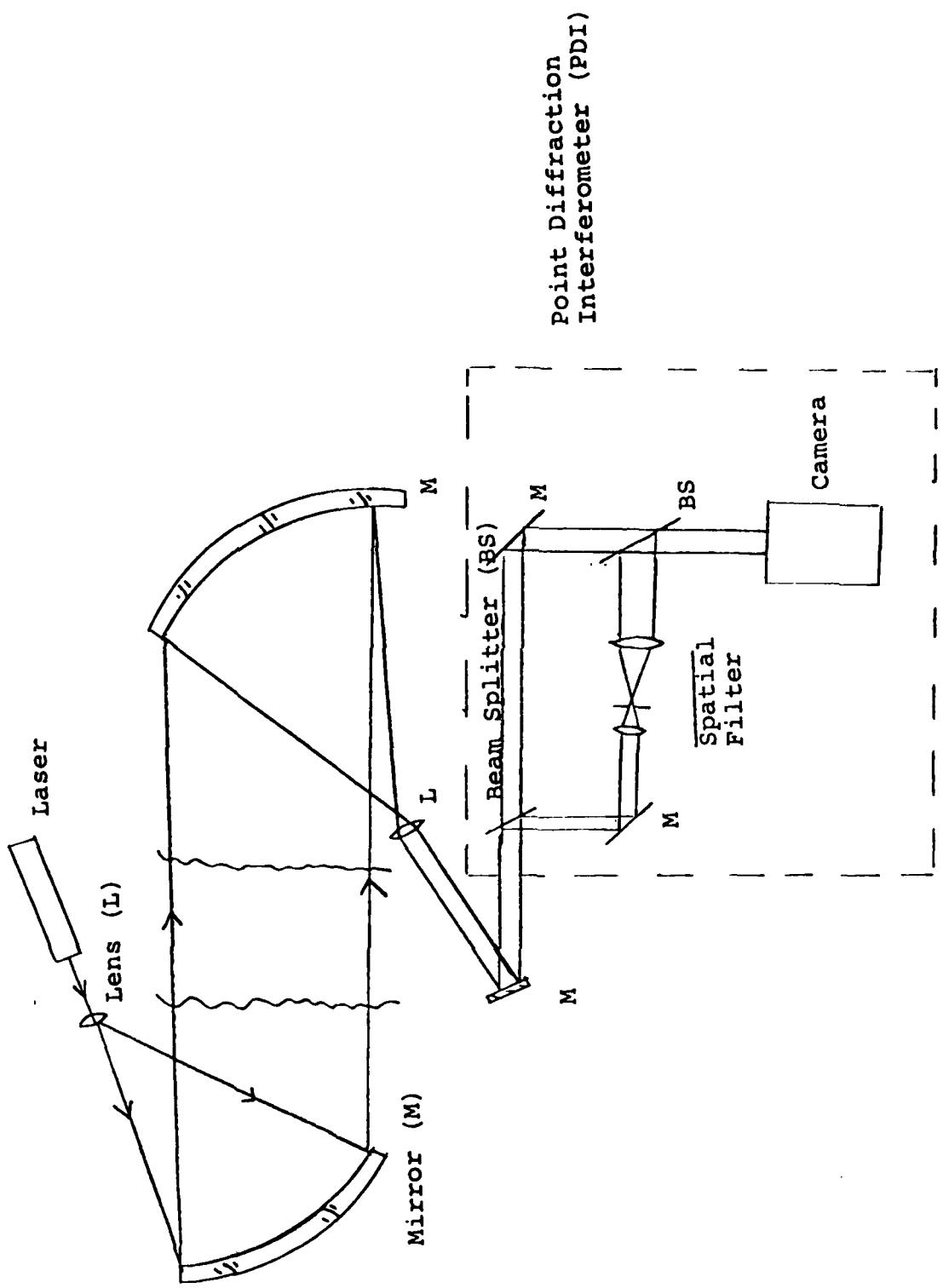


Figure A-2.6 Schematic diagram of a point diffraction interferometer for wind tunnel applications.

done so as to pass only the rays which are not refracted by the density field in the wind tunnel. As in the conventional Mach Zehnder interferometer, the beams are reunited by the second splitter plate which is also used to regulate the structure of the interference. From here, the usual fringe reading and applicable data reduction processes can be used to compute flow-field densities from the optical data.

The prospects of PDI are excellent because of its vibration insensitivity. As with holographic interferometry a pulsed source and television camera could be used for recording. Thus far, however, PDI has not been applied to wind tunnel tests.

A-2.3.3 Heterodyne Interferometry

Both the holographic interferometer and the point diffraction interferometer can be operated as heterodyne interferometers to provide real-time interferometry.⁴ In the heterodyne mode a frequency shifter (i.e., moving mirror in the reference beam) is used to modulate the phase in the reference beam in a periodic fashion to provide real-time interferometry. Since heterodyne interferometry provides a direct measurement of the object wave phase differences, it eliminates the need to find and evaluate fringe pattern positions as described in the interference pattern evaluation system, Section A-2.3.1.3. This is especially important in the analysis of flow fields where the fringe pattern can be badly distorted near the edges of test objects in the flow fields. Likewise since it is a direct measurement technique the amount of computer processing is much less, since the only requirement is to compute the densities and refractive indices from the directly measured phase variations in the object wavefront. With this type of instrument the phase measurements are instantly obtained instead of the 2 minutes in the system described in Section A-2.3.1.3 where the fringe patterns are digitized. A detector array with the required spatial resolution is used to directly measure the real-time phase differences. It is expected

that it would cost at least as much as the systems of Section A-2.3.1.3 because no work has been done with this technique for flow-field evaluation.

SECTION A-3

FLOW FIELD VELOCITY MEASUREMENTS

Optical techniques have been extensively utilized for nonintrusive probing of fluid velocities. A variety of different approaches have been used with the major efforts concentrated in either time-of-flight systems or in measurement of the Doppler shift of the frequency of scattered light. The time-of-flight techniques can measure the time to cross a single light beam (one-spot),⁵ whose cross-section is known, or they can measure the time to cross between two light beams (two-spot),⁶ whose spacing is known. Time-of-flight techniques are characterized by strong signals, the light beams are tightly focused, and the techniques can make measurements where signal interferences such as background luminosity or surface scattering would stop other techniques. Their drawback is that they can only measure one part of the velocity, either a single component or the magnitude of the velocity in a plane. Extension of this method to multi-component measurement is not practical.

Doppler shift techniques for measuring velocity have a long history, especially in the field of astronomy where the Doppler shift is used to measure the recession speed of stellar bodies. These speeds are very high and the spectral shifts, due to the Doppler effect, are large and easily discernible, even with coarse instrumentation. As the speed decreases, the Doppler shift decreases proportionally and much more sophisticated instrumentation is required to accurately measure the change in frequency. Commonly Fabry-Perot interferometers (FPI) are used for high-resolution measurements. Laser-based Doppler measurement instruments have been constructed, using FPI's either at the source or at the detection end.

The use of a laser as a source of radiation to interrogate the moving body has eliminated the need to have a body that

emitted radiation, as in the stellar observations. The laser's bandwidth can be much narrower than the halfwidths associated with spectral transitions, and this feature has been used in several techniques to provide measurements of quite small velocities, useful for laboratory aerodynamic studies. One approach has been to scatter the laser radiation from a solid body moving with the fluid. The scattering is elastic and the scattered radiation will be Doppler shifted in frequency. If the body is moving fast enough, so that the shift is greater than the laser's linewidth, the FPI can be used to measure the velocity field.⁷ Another technique, used in wind tunnels, has been to seed the flow with Na atoms.* The Na can absorb and re-emit the laser radiation, the "scattering" strength proportional to the Na absorption coefficient at the laser wavelength. Irradiating the flow at an angle to the main flow direction will result in a shift of the absorption band, according to the Doppler shift, from where it would be in a stationary sample. By sweeping the frequency of a laser's narrow linewidth, and illuminating both a stationary sample and the moving fluid, the Doppler shift can be determined directly from the intensities scattered from the two samples.⁸ Zimmerman and Miles⁹ have developed a clever modification that uses a retroreflector and eliminates the need for the stationary sample.

* This is a difficult technical feat and special care must be taken to prevent the formation of dimers. Also, this technique is only well suited to helium flowfields since He does not quench excited Na.

Another approach is to seed the flowfield with iodine. The I₂ spectrum is very rich in the visible region and several lines overlap Argon laser-lines. By using an etalon (effectively an FPI in the source instead of at the detector), the laser can be made to oscillate on a single longitudinal mode and this mode can be swept over the laser bandwidth. As a result, the I₂ absorption, and subsequent fluorescence intensity, will depend upon the location of the laser line within the Doppler shifted linewidth of the I₂ absorption line, and this I₂ line can be mapped by shifting the laser¹⁰⁻¹³ (the frequency changes in integral amounts of a fixed quantity which can be accurately determined independently). An alternative approach^{13a} has been to observe the scattering from iodine using four beams, the forward and retro-reflected beams in two directions to the flow. The authors attempted to determine two components of the flow velocity from the measurements. In any technique requiring multiple observations,^{13,13a} the observations must all occur within one correlation time of the flow in order that the observations can be interpreted as a flow velocity measurement. Unfortunately the time restriction in most aerodynamic flows of interest is too short for the two-dimensional mapping probes to handle and, as a result, with current technology these probes cannot provide meaningful measurements of velocity fluctuation.

The last Doppler technique that will be introduced is the measurement of the Doppler shift of elastically scattered radiation using either heterodyne or homodyne mixing.¹⁴ This is the most commonly employed nonintrusive velocity measurement technique, and instrumentation is available from several commercial sources. The principle of the technique makes use of the temporal coherence (monochromaticity) of the laser source. The Doppler-shifted scattered-radiation frequency is down-shifted to where it can be measured electronically. The down-shift frequency is usually derived from the same laser source and the Doppler shift can be measured precisely, enabling an accurate

determination of the velocity in the flowfield. The major limitation is the frequency range that can be measured so that the method becomes less useful at higher Mach numbers. The technique requires elastic scattering, usually from solid bodies in the flow, and is known as either laser Doppler anemometry (LDA) or laser Doppler velocimetry (LDV) depending on how accurately the solids are following the fluid flow. LDA techniques can be extended to multidimensional measurements in a straightforward manner and therefore it is the favored technique in aerodynamic velocity measurements. Consequently, in the following sections the LDA technique and its application to boundary layer measurement with a supersonic free stream flow will be studied in detail. This is the most trying condition for boundary layer measurements and the system designed for this flow will also work well in lower-speed tunnels.

In the sections that follow a detailed design and error analysis of a 3-D LDA will be worked out based upon the dual-beam LDA. This type of system represents the current state-of-the-art multi-component velocity measurement instrument used in wind tunnels. The criteria for selecting the configuration will be presented in a general format. The detailed examples will be relevant to the Flight Dynamics Laboratory's LDA system in operation in the transonic wind tunnel.

A-3.1 LASER DOPPLER ANEMOMETRY

In the far field, where the scattered light wave is a spherical wave, the scattered spherical field can be described in terms of its frequency

$$\nu_s = \nu_o + \frac{1}{\lambda} \bar{v} \cdot (\hat{r} - \hat{s}) \quad (A-12)$$

where ν_s is the scattered field's frequency, ν_o is the incident frequency, λ is the incident wavelength in the medium, \bar{v} is the

vector velocity of the scatterer, and \hat{f} and \hat{s} are unit vectors in the direction of observation and the incident laser direction respectively (Figure A-3.1). The Doppler shift, ($v_s - v_o$), depends linearly on the component of \bar{v} in the direction ($\hat{f}-\hat{s}$). It is important to be aware of the relative sizes of the parameters. Typically $v_o \approx 5.8 \times 10^{14}$ Hz when $\lambda = 514.5$ nm (Argon green line), so that the maximum Doppler shift would be ~ 3.9 MHz/(m/s). Even at high velocities, the Doppler shift is a small fraction of the incident/scattered frequency making direct observation difficult (ex. 3.9 GHz @ 1000 m/s represents a shift of 6.7 parts per million of the original frequency).

A-3.1.1 Downbeating

It is possible to beat the scattered radiation with another light beam derived from the same laser source. The mixing takes place in the photodetector, a device that responds to intensity, not to amplitude. In a simplified example consider two sinusoidal fields $\sin \omega_1 t$ and $\sin \omega_2 t$ incident on the detector. The detector would respond to $[\sin \omega_1 t + \sin \omega_2 t]^2$. By use of trigonometric identities this becomes $[\sin \omega_1 t + \sin \omega_2 t]^2 = 1 + \frac{1}{2} (\cos 2\omega_1 t + \cos 2\omega_2 t) + \cos(\omega_1 - \omega_2)t - \cos(\omega_1 + \omega_2)t$. The frequencies $2\omega_1$, $2\omega_2$, and $\omega_1 + \omega_2$ are so large that the detector cannot respond and it averages the result to zero. If $\omega_1 - \omega_2$ is sufficiently small the detector can follow this component's variation. The photodetector downmixes the signal to the frequency ($\omega_1 - \omega_2$).

There are three optical configurations used in LDA to provide a reference frequency.¹⁵ These are known as the reference beam mode, the dual scatter mode, and the dual-beam mode, all shown in Figure A-3.2. In the reference beam mode a weak reference beam is split from the main beam and mixed with the scattered radiation at the detector. The disadvantage to this mode (Figure A-3.2.a) is that the wider the collection aperture (to increase signal), the greater the uncertainty in r and there-

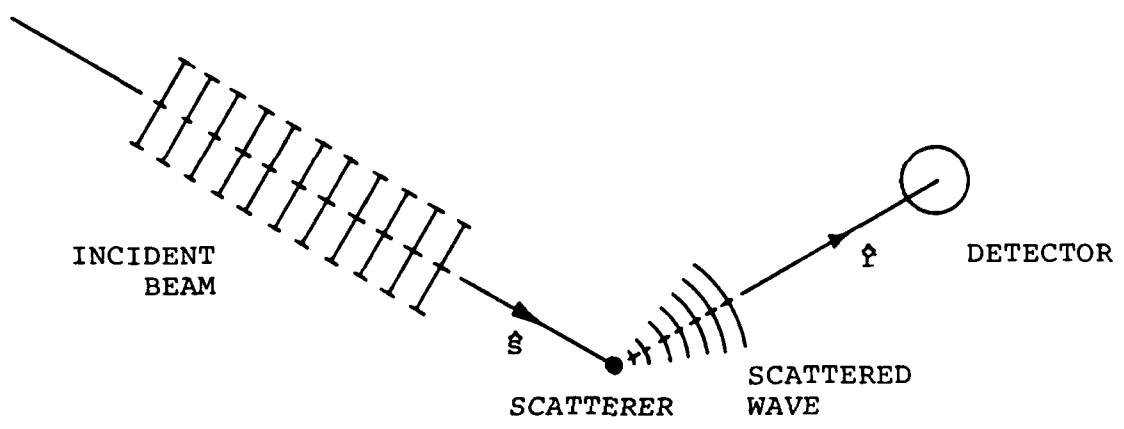
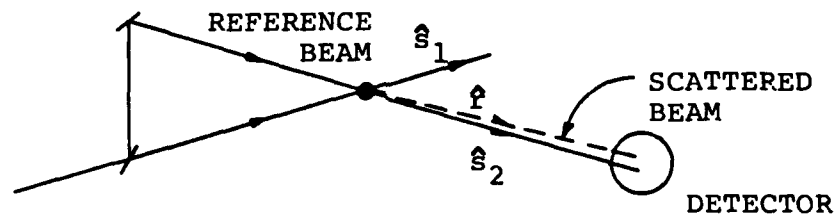
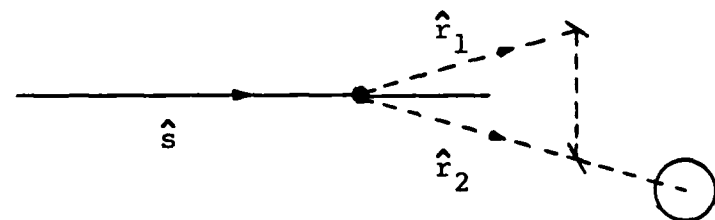


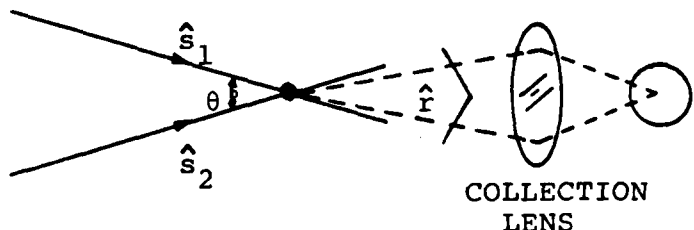
Figure A-3.1 Scattering geometry.



(a) Reference beam mode.



(b) Dual scatter mode.



(c) Dual beam mode.

Figure A-3.2 LDA optical configurations.

fore the greater the uncertainty in the velocity measurement. Also, the alignment requirements for heterodyning are severe and difficult to maintain.¹⁶ The advantage is that the reference beam can be brought from any angle so that any direction of velocity measurement can be selected.

The dual-scatter mode mixes together the light scattered in two different directions (Figure A-3.2.b). The resulting Doppler signal $v_D = v_{s1} - v_{s2} = \frac{1}{\lambda} \bar{v} \cdot (\hat{r}_1 - \hat{r}_2)$ is independent of the direction of the incident beam. The disadvantage of this mode is, as with the reference beam mode, that the aperture must be restricted in order to define r_1 and r_2 with sufficient accuracy that the component of v in the direction ($\hat{r}_1 - \hat{r}_2$) can be computed to the desired accuracy. This is a severe restriction on the collection aperture.

The dual-beam mode mixes the scattered radiation from two input beams, whose unit propagation vectors \hat{s}_1 and \hat{s}_2 , that cross at an angle θ . The resulting scattered frequencies from each beam, in a particular direction r , are

$$v_{s1} = v_o + \frac{1}{\lambda} \bar{v} \cdot (\hat{r} - \hat{s}_1) \quad (A-13a)$$

and $v_{s2} = v_o + \frac{1}{\lambda} \bar{v} \cdot (\hat{r} - \hat{s}_2) \quad . \quad (A-13b)$

As a result of the mixing, the Doppler signal generated by the detector is

$$v_D = v_{s1} - v_{s2} = \frac{1}{\lambda} \bar{v} \cdot (\hat{s}_2 - \hat{s}_1) \quad (A-14)$$

which is independent of r . This is the great advantage of the dual beam method; the Doppler frequency resulting from mixing the scattered radiations is the same everywhere in space. Consequently the scattered radiation can be collected over a large aperture, and a substantially stronger signal will result than for either of the other LDA methods. The Doppler frequency is linearly proportional to the component of velocity in the direction $\hat{s}_2 - \hat{s}_1$ with the relation

$$\nu_o = Kv \quad (A-15)$$

where

$$K = \frac{2}{\lambda} \sin \theta/2 \quad . \quad (A-16)$$

A-3.1.2 "Fringe" Model

When two plane parallel laser beams with the same polarization intersect on a screen, a set of interference fringes occurs with the spacing

$$d_f = \frac{\lambda}{2 \sin \theta/2} \quad . \quad (A-17)$$

Consequently researchers proposed the "fringe" model to explain the LDA signal. The Doppler frequency results from the scattering of a particle as it crosses a series of interference fringes. This model provides a simple conceptual picture to explain the LDA process which is correct only in limited situations and should not be used in a general sense.¹⁷ But so long as the scatterer size is substantially less than the "fringe" spacing the results will be accurate.

A difficulty arises with the use of Equation (15) for generalized turbulent flows. The Doppler signal is not direction sensitive, i.e., the detector interprets $-\nu_D$ and $+\nu_D$ as the same frequency. This is overcome by a single-sideband modification in which the frequency of one of the incident beams is shifted by a fixed amount, n_{BC} , usually using an acousto-optic Bragg cell. The Doppler signal now becomes

$$\nu_D = \nu_{BC} + Kv \quad (A-18)$$

and so long as the negative value of Kv never exceeds n_{BC} the Doppler signal can be interpreted unambiguously. Difficulties arise in selecting an optimal value of n_{BC} for measurements through flows that have large mean velocity changes, such as boundary layers in supersonic wind tunnels. Often a compromise value must be selected to provide adequate LDA performance in all

regions. An example illustrating a selection of v_{BC} is worked through later.

Using the concept of the "fringe" model, several operational requirements for the optical system become evident. The Doppler signal will be generated by scattering from the region in space where the two incident beams cross. For the "fringes" to have the same spacing throughout this region it is necessary that the beams be plane waves. Also, for ease of interpreting the flow information, the region of space in which the beams cross should be very small. Fortunately these two requirements can be fulfilled simultaneously by focussing the two input beams and crossing them at their waists. The resulting beam parameters (e^{-2} intensity profiles, wavefront radius as a function of position, etc.) have been presented in the literature^{18,19} and will not be developed here. Only the results will be used.

A-3.1.3 Dual Beam LDA

A simple configuration, which will provide the required optical arrangement, is shown in Figure A-3.3. The key element is the lens which both crosses the beams and focusses them at the crossing point. In actual practice a telescope should be used to ensure that the beams focus at the crossing location and the interference pattern, as seen on a screen, should be examined throughout the crossing region (the LDA spot). The beams will focus to a diameter

$$\frac{d}{e^{-2}} \approx (4/\pi) \lambda (f/D) \frac{D}{e^{-2}} \quad (A-19)$$

where f is the focal length of the lens, $D_{e^{-2}}$ is the diameter of the beams at the lens, and $f/D_{e^{-2}}$ is the f-number of the focused beam. The LDA spot is an ellipsoid with dimensions

$$d_m = \frac{\frac{d}{e^{-2}}}{\cos \theta/2} \quad (A-20)$$

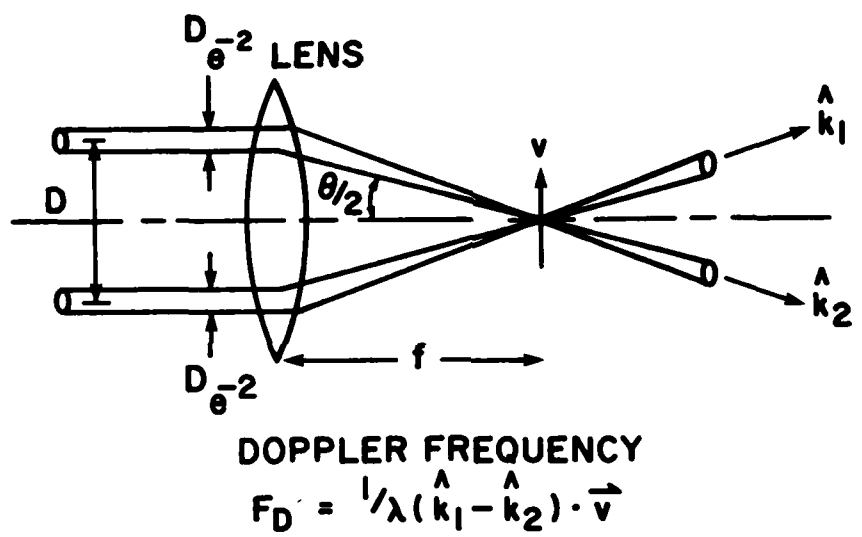


Figure A-3.3 One-component dual-beam LDA geometry.

$$l_m = \frac{d}{\sin \theta/2} e^{-2} \quad (A-21)$$

$$h_m = \frac{d}{e} e^{-2} \quad (A-22)$$

and the number of fringes within the spot is

$$N_{FR} = d_m / d_f . \quad (A-23)$$

It should be noted that when a Bragg cell is used the concept of the number of fringes has little utility. Instead the spot crossing time and the Doppler frequency must be computed and their product will give the maximum number of Doppler cycles in the signal.

A-3.1.4 Multicomponent Velocity Systems

There are three common methods for extending the LDA system to two-dimensional measurements and there are several configurations of each. The further extension to three-dimensional measurements is more restrictive. The three two-dimensional dual-beam LDA systems use either color, polarization, or frequency to differentiate the components. The systems can be either three-beam or four-beam systems and are shown as a matrix in Figure A-3.4. The optical system can be rotated about the centerline to provide a measurement coordinate orientation better suited to the flow system being studied, or to provide better access around models. If the beam pattern is translated with respect to the centerline or if the beams are tilted relative to the third axis, information on the velocity component in this direction may be mixed into the signals (see Appendix). In a two-dimensional system care must be exercised to ensure that the maximum contribution of this component to the signals is less than the uncertainty in the measurements themselves.

The color separation and polarization separation schemes have been used extensively. The frequency separation scheme

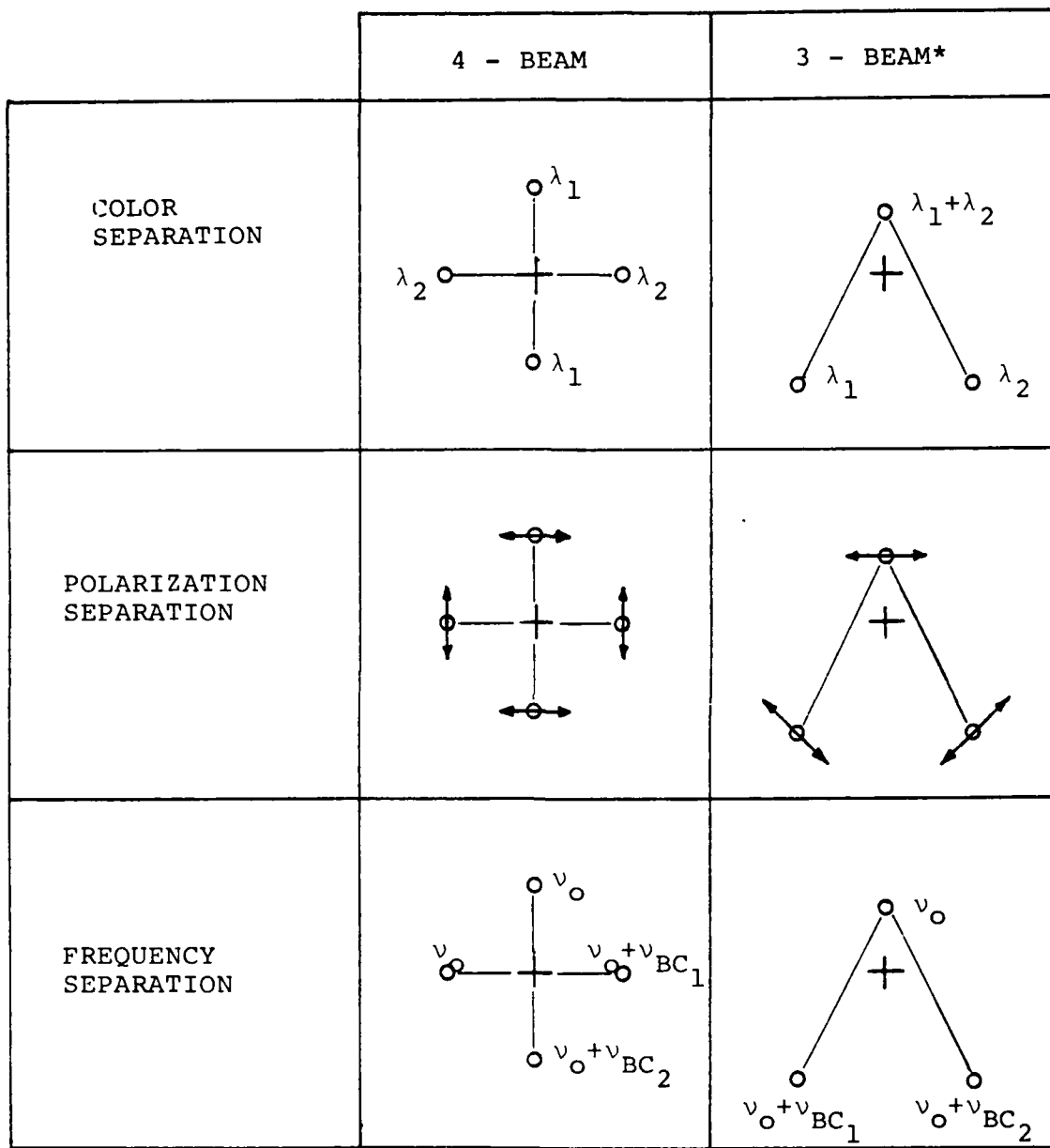


Figure A-3.4 Component separation schemes for two-dimensional LDA systems using 3-beam and 4-beam optical systems.

suffers from the fact that the frequency range for each component is severely limited since the two components must be separated by frequency filters. The extension from a two-dimensional system to a three-dimensional system usually entails the addition of a separate one-dimensional system to a two-dimensional system. When appropriate optical access is available the third component can be aligned orthogonally to the other two and the measurement is straightforward. Typical systems use Argon ion lasers and will combine polarization and color separation to get all three components using the two strongest Argon lines (514.5 nm and 488.0 nm) or they will use three different Argon lines (514.5 nm, 488.0 nm and either 496.5 nm or 476.5 nm). The two strong lines have comparable powers but the next strongest lines are reduced to $\approx 15\%$ of the stronger lines' power. As a result measuring the third component in a three-color system requires added care.

More often than not the flow system being measured does not provide optical access permitting orthogonal measurements. There are two generic schemes in use based upon measurements in a nonorthogonal coordinate frame. The commercial realizations of these systems are shown in Figure A-3.5.20,21 In addition there are several individual systems, similar in appearance and operation but using different separation schemes.^{22,23} One feature of the system shown in Figure A-3.5(a) is that the scattered signals are collected on the opposite arms from the incident beams. This ensures that the two arms are aligned to the same spot and that the measured signal on each channel, at one instant in time, comes from the same scatterer. This is of particular importance when measurements are taken in a nonorthogonal coordinate system or when cross-product data (e.g., Reynolds stress) are desired.

A-3.1.5 Considerations in Practical Application

There are several aspects of the acquisition and interpretation of LDA data that need to be taken into account in the design and operation of the LDA. First, there are the uncertainties

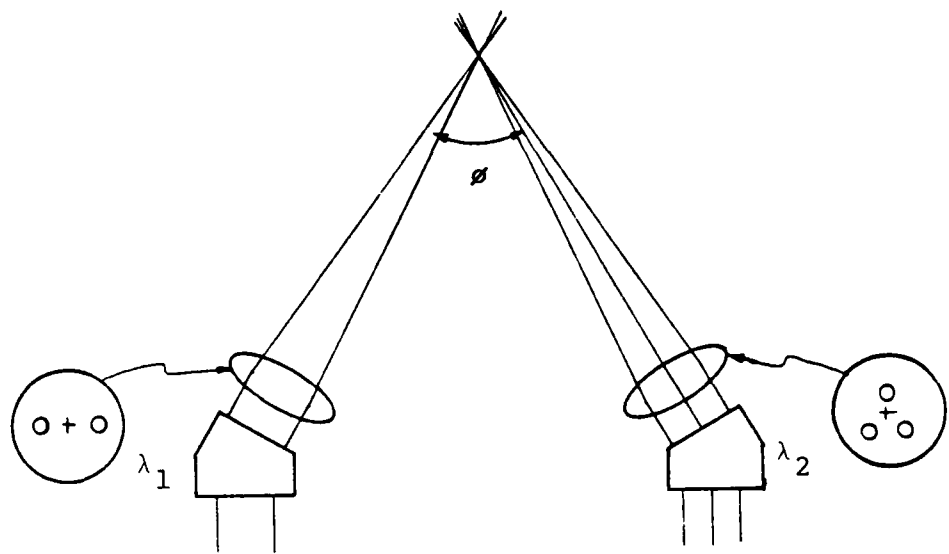


Figure A-3.5a Schematic of DISA 3-D LDA system.

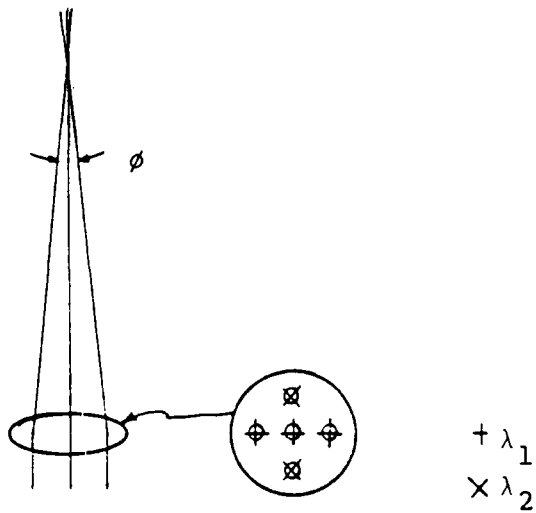


Figure A-3.5b Schematic of TSI 3-D LDA system composed of a 3-beam 2-D frequency separation system, measuring two non-orthogonal velocity components, and a 2-beam 1-D LDA measuring the velocity component orthogonal to the plane of the other two components.

that result when the data are measured in one coordinate frame and then transformed to a different frame. Then there is the question of how many measurements are required to characterize the distribution to any specified moment. Both of these questions are relevant to aerodynamic measurements in general and to the AFWAL/FI Transonic Wind Tunnel studies in particular.

A-3.1.5.1 Coordinate Transformation

Consider a flowfield in which the coordinate frame of interest is x, y, z , an orthogonal set. Suppose an LDA system is used that makes measurements along the coordinates x', y', z' , as shown in Figure A-3.6. The transformation from the measurement frame to the reference frame is given by:

$$\begin{bmatrix} v_x \\ v_y \\ v_z \end{bmatrix} = \frac{1}{D} \begin{bmatrix} \Gamma_{xx'} & \Gamma_{xy'} & \Gamma_{xz'} \\ \Gamma_{yx'} & \Gamma_{yy'} & \Gamma_{yz'} \\ \Gamma_{zx'} & \Gamma_{zy'} & \Gamma_{zz'} \end{bmatrix} \begin{bmatrix} v_{x'} \\ v_{y'} \\ v_{z'} \end{bmatrix} \quad (A-24)$$

where

$$D = \begin{vmatrix} \cos \gamma_{xx'} & \cos \gamma_{xy'} & \cos \gamma_{xz'} \\ \cos \gamma_{yx'} & \cos \gamma_{yy'} & \cos \gamma_{yz'} \\ \cos \gamma_{zx'} & \cos \gamma_{zy'} & \cos \gamma_{zz'} \end{vmatrix} \quad (A-25)$$

and Γ_{ij} is $(-1)^{i+j}$ multiplied by the determinant of the submatrix of D formed by striking out the row and column containing the (i, j) element. For example:

$$\Gamma_{yx'} = (-1)^3 (\cos \gamma_{xy'} \cos \gamma_{zz'} - \cos \gamma_{zy'} \cos \gamma_{xz'}) . \quad (A-26)$$

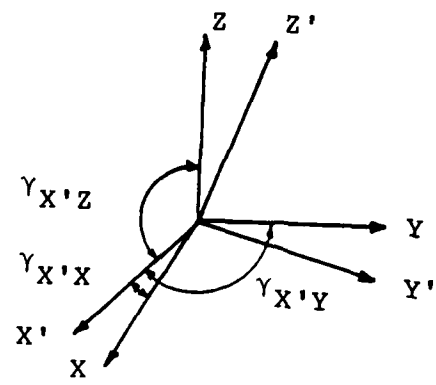


Figure A-3.6 Orthogonal reference coordinate frame (X, Y, Z) and LDA coordinate frame (X', Y', Z').

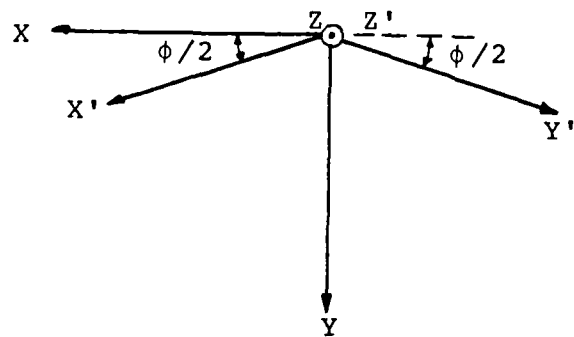


Figure A-3.7 Relationship of measurement frame and reference frame.

Consider the geometry shown in Figure A-3.5(a). The coordinate frame is such that z and z' coincide and x, y, x', y' are as shown in Figure A-3.7. The transformation becomes

$$\begin{bmatrix} v_x \\ v_y \\ v_z \end{bmatrix} = \frac{1}{2} \begin{bmatrix} \frac{1}{\cos \theta/2} & \frac{-1}{\cos \theta/2} & 0 \\ \frac{1}{\sin \theta/2} & \frac{1}{\sin \theta/2} & 0 \\ 0 & 0 & 2 \end{bmatrix} \begin{bmatrix} v_{x'} \\ v_{y'} \\ v_{z'} \end{bmatrix} . \quad (\text{A-27})$$

Expanding yields

$$v_x = \frac{1}{2\cos \theta/2} [v_{x'} - v_{y'}] \quad (\text{A-28a})$$

and

$$v_y = \frac{1}{2\sin \theta/2} [v_{x'} + v_{y'}] . \quad (\text{A-28b})$$

The uncertainties associated with each velocity calculated (one standard deviation) can be expressed as

$$\begin{aligned} \delta v_x = & \frac{1}{2 \cos \phi/2} \left(\frac{1}{2} \tan \phi/2 w d \right)^2 (v_{x'}^2 + v_{y'}^2) \\ & + [(\delta v_{x'})^2 + (\delta v_{y'})^2]^{1/2} \end{aligned} \quad (\text{A-29a})$$

and

$$\begin{aligned} \delta v_y = & \frac{1}{2\sin \phi/2} \left(\frac{\delta \phi}{2\tan \phi/2} \right)^2 (v_{x'}^2 + v_{y'}^2) \\ & + [(\delta v_{x'})^2 + (\delta v_{y'})^2]^{1/2} . \end{aligned} \quad (\text{29b})$$

In most systems of practical interest the precision in determining ϕ is sufficient that first term [of order $(\delta \phi)^2$] is negligible no matter how small the turbulence intensity. If the flowfield were to move the beams about so that this motion became the determining uncertainty in ϕ , then the relative importance of the terms might change. The uncertainties δv_x and δv_y will be

considered as resulting entirely from $\delta V_x'$ and $\delta V_y'$. For the geometry shown in Figure A-3.7,

$$\delta V_x = 1.05 \text{ RMS } (\delta V) \quad (\text{A-30a})$$

$$\delta V_y = 3.52 \text{ RMS } (\delta V) \quad (\text{A-30b})$$

where

$$\text{RMS } (\delta V) = \frac{1}{2} \sqrt{(\delta V_{x'})^2 + (\delta V_{y'})^2}. \quad (\text{A-31})$$

Therefore, the uncertainty in the determination of V_y is 3.5 times larger than the RMS uncertainty. For the geometry shown in Figure A-3.5(b) the factor increases to 6.4x. It is evident from this discussion that the uncertainty in the velocity determination must be reduced to as little as practical and, also, in a nonorthogonal reference frame, the angles between the axes should be as close to right angles as is practical. In some experimental configurations the beams are canted so that z and z' do not align either. This further complicates the issue as the V_z' component is mixed into V_x and V_y . Analysis of this situation is a direct extension of the material presented. It should be emphasized that the uncertainty in each component is a function of the magnitude of the RMS uncertainty. Consequently, even if the flow is principally in one direction, the uncertainty in the velocity measurement of the spanwise component may be greatly influenced by the uncertainty in the streamwise component.

A-3.1.5.2 Counter-Processor Errors

The uncertainties expressed in Equations (A-29a-b) include only the random uncertainties resulting from measurement limitations. Bias errors are not included. It is presumed that careful experimentalists will ensure that the contribution resulting from potential bias error sources is smaller than the random fluctuations. A source of the random fluctuations will now be considered and the magnitude will be computed for a "typical"

LDA measurement system. The parameters used will be for application to measurements through the boundary layer and into the free stream in a supersonic wind tunnel. Assumed is a system with a counter-processor (C-P), 1 ns resolution, determining the Doppler frequency. The laser source mode spacing is taken to be 140 MHz so that the maximum Doppler frequency will be 70 MHz. (An etalon can be used to eliminate the other longitudinal modes but 70 MHz will remain a practical limit due to the response of the typical photodetector. For high-power Argon lasers the longitudinal mode spacing is much less.) The size of the LDA spot diameter will be taken to be 250 μm (d_m) and the free stream velocity will be 1000 m/s. Because the crossing time

$$t_c = d_m/v = 250 \text{ ns} \quad (\text{A-32})$$

is minimal at the highest velocity, the Doppler frequency must be the highest possible for the system at this velocity, 70 MHz. The maximum number of Doppler cycles scattered will be

$$N_c = v_D t_c \approx 18 \quad (\text{A-33})$$

necessitating the C-P analysis circuitry to be set for 2^3 cycles if it is desired to make efficient use of the scattering events, most of which will scatter less than N_c cycles. If the uncertainty in the period determination is ± 1 C-P clock cycle, then δv_D is 0.875% and

$$\delta v = \delta v_D \left(1 + \frac{v_{BC}}{v_D - v_{BC}} \right) \quad (\text{A-34})$$

will depend on the frequency of the Bragg cell. A typical Bragg cell frequency is 40 MHz. If this were used then for v_D to be 70 MHz at 1000 m/s would require $K = 30 \text{ kHz}/(\text{m/s})$, equivalent to a "fringe" spacing of 33.3 μm . Therefore

$$d_f = \frac{\lambda}{2 \sin \theta/2} = 33.3 \mu\text{m} ,$$

and

$$l_m = \frac{d_m}{\sin \theta/2} = 32.2 \text{ mm}$$

at $\lambda = 514.5 \text{ nm}$, and $\delta V \approx 2\%$. The spot length, l_m , is too long to define the scattering event location precisely. Also, the velocity uncertainty deteriorates rapidly as the velocity decreases ($\delta V \approx 7.7\%$ when $V = 100 \text{ m/s}$), and the uncertainty in the orthogonal component is even larger. The situation can be improved by reducing n_{BC} to as small a value as practical. For example, if a dual Bragg cell arrangement is employed to effect $v_{BC} = 5 \text{ MHz}^*$ then d_f becomes $15.4 \mu\text{m}$ and l_m becomes 3.8 mm . Again $\delta v_D = 0.875\%$ but now $\delta V = 0.94\%$. When the velocity drops to 100 m/s , $t_c = 2.5 \mu\text{s}$, $v_D = 11.5 \text{ MHz}$, and $N_c \approx 29$. Leaving the C-P set for 2^3 cycles results in a frequency uncertainty δv_D of 0.14% and $\delta V = 0.25\%$. Even at $v = 10 \text{ m/s}$, $\delta v_D = 0.07\%$ and $\delta V = 0.6\%$. All the errors computed should be acceptable in most research situations. The system deteriorates rapidly when two-dimensional measurements are required and one measurement vector is orthogonal to the streamwise component. In this case the spanwise velocity is zero, the Doppler frequency is v_{BC} but the crossing time is determined by the streamwise velocity, yielding $N_c \approx 1$ at $V = 1000 \text{ m/s}$, a totally unacceptable result. Either v_{BC} can be raised back to 40 MHz with the accompanying increase in the uncertainties, or the optical system can be rotated to $\pm 45^\circ$ about the streamwise component. In the latter case, the Doppler frequency will decrease if the "fringe" spacing is maintained or the "fringe" spacing can be reduced to maintain the Doppler fre-

*In boundary layer flow measurements v_{BC} can be made small since the Bragg cell offset frequency is only used to ensure sufficient Doppler cycles for analysis during the passage of the scatterer. In recirculating flows, especially where the reverse velocity is comparable to the free stream velocity, v_{BC} must be maintained near the middle of the available Doppler bandwidth.

quency at 70 MHz (preferable). When the system is further expanded to three-dimensional measurements using either of the schemes shown in Figures A-3.5(a) or A-3.5(b), the 1-D system's optimum alignment will be as parallel to the free stream as possible. The uncertainties at lower velocities can be reduced by increasing the number of C-P cycles used in the analysis. Figure A-3.8 plots N_c versus the velocity for the one-dimensional analysis. Typically, the number of C-P cycles used should be approximately one-half the value of N_c for the maximum velocity anticipated at the measurement location, i.e., the average velocity plus 3 turbulence intensity increments. For example, if the average velocity was 10 m/s and T.I. = 50% then the maximum velocity anticipated would be 25 m/s. From Figure A-3.8, $N_c = 2^6$ at 25 m/s. Therefore the C-P could be set for 2^5 cycles and the uncertainty in the measurement would be reduced by a factor of 4 from that computed previously.

A-3.1.5.3 Data Uncertainty Due to Noise

The analysis presented above has assumed that the S/N was sufficiently high that the uncertainty due to the noise in the signal was negligible compared with the C-P timing uncertainty. Often this is not the case. The S/N degenerates as the frequency increases. Two factors determine the S/N. First, the signal decreases in direct proportion to the frequency increase. Second, the noise amplitude will change depending upon its origin. If the major noise source is detector shot noise, then the noise will decrease as the square root of the signal, so that

$$S/N \propto (\nu_D)^{-1/2}$$

On the other hand the signal may decrease to the point that thermal noise becomes dominant. As the Doppler frequency increases, the amplifier's bandwidth has to increase proportionally and the

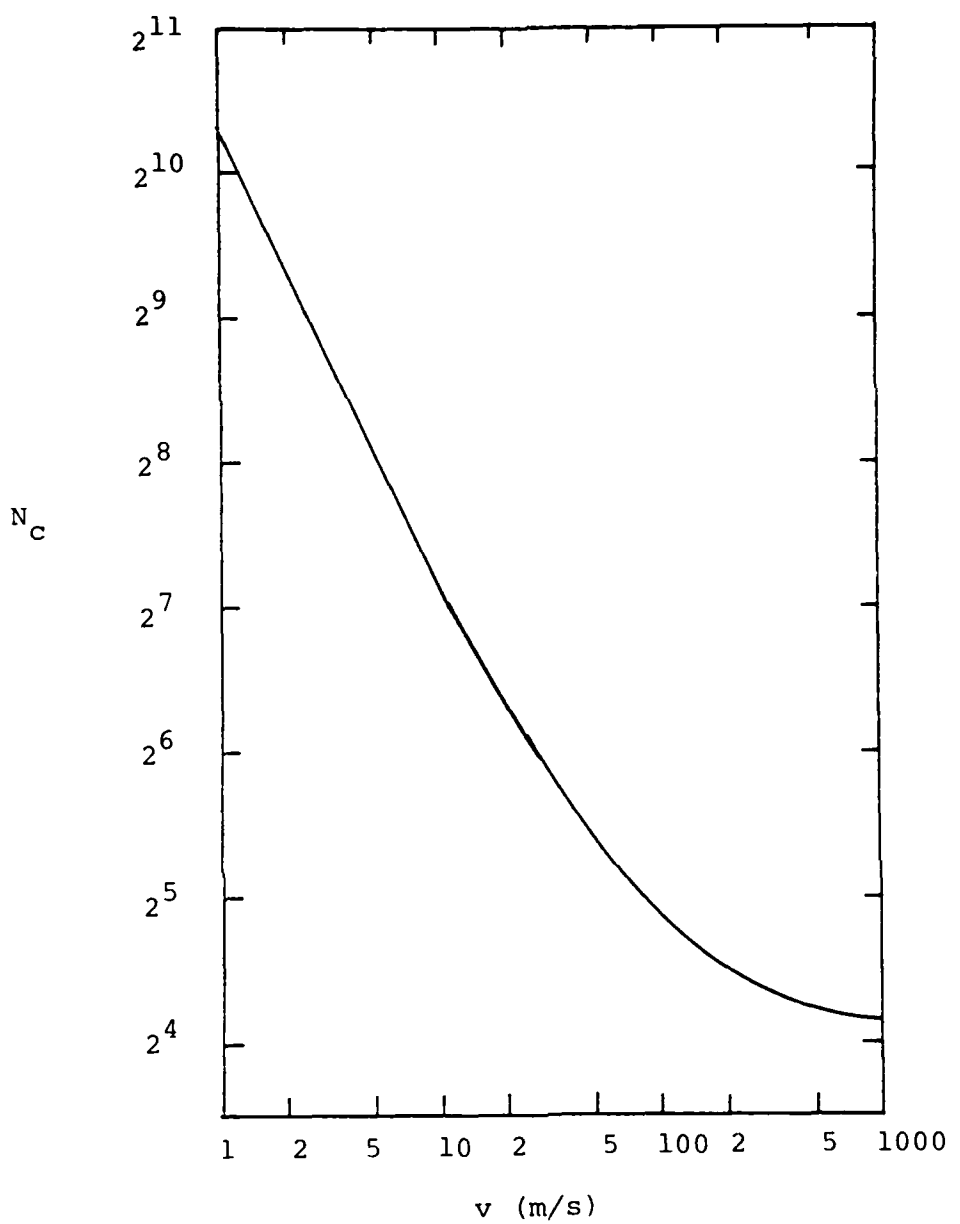


Figure A-3.8. Maximum number of Doppler cycles scattered in the 1-D system analysis.

$$N_c = \frac{d_m}{d_f} \left(1 + \frac{\nu_{BC}}{\nu_D - \nu_{BC}} \right)$$

with $d_m = 250 \text{ } \mu\text{m}$, $d_f = 15.4 \text{ } \mu\text{m}$, and $\nu_{BC} = 5 \text{ MHz}$.

thermal noise increases as the square root of the bandwidth. In the limit of the thermal noise being dominant

$$S/N \propto (\nu_D)^{-3/2}$$

This is the most common situation in aerodynamic LDA studies. A study of the effect of noise on the LDA frequency determination has been made by Adrian et al.²⁴ Whiffen et al.²⁵ have investigated a model proposed by Mayo in which the apparent turbulence intensity (E_n), due solely to the noise, can be expressed in terms of the S/N for a C-P using N_c Doppler cycles:

$$E_n = \frac{1}{4\pi\sqrt{SNR} N_c} . \quad (A-35)$$

Their measured results agreed within $\pm 50\%$ of the prediction. Based on this relation a minimum S/N of 4 is required to ensure the noise uncertainty contribution to the velocity is less than 0.5% when 2^3 cycles are used by the C-P. Pfeifer²⁶ has made similar observations in a study in which he also examined the influence of the comparison accuracy for a double counter C-P system, i.e., how the uncertainty is affected by the accuracy setting on the 5:8 comparison. His results show that the uncertainty is independent of the comparison accuracy and he measured uncertainties comparable to those of Whiffen.²⁵

A-3.1.5.4 Statistics Uncertainties

Beyond the uncertainties in a single measurement there are also the questions of how many measurements are required to adequately define the velocity distribution and of how long measurements must be taken in the flow to fully represent all possible flow conditions at the location. The question of the number of measurements was addressed by Cline and Bentley.²⁷ They showed that if the velocity distribution could be characterized as a one-dimensional normal distribution with mean value \bar{v} and standard deviation σ (turbulence intensity $TI = \mu$), then if a sample of size N gave a mean value of \bar{v} and a standard deviation of s ,

the variance in \bar{v} is

$$\sigma_{\bar{v}}^2 = \sigma^2/N \quad (A-36)$$

and the tolerance in \bar{v} is

$$Tol(\bar{v}) = Z \frac{\sigma_{\bar{v}}}{\mu} = Z TI/\sqrt{N} \quad . \quad (A-37)$$

Thus a 95% assurance that μ is within $Tol(\bar{v})$ around \bar{v} is achieved when $Z = 1.96$ (normal distribution). Figure A-3.9 is a plot of Equation (A-37) for several TI's, with $Z = 1.96$. For example, to be 95% sure that \bar{v} is within 5% of μ at a measurement location where the TI is 20% requires more than 50 random measurements. Higher-order moments will take longer to stabilize. The tolerance in the turbulence intensity is expressed as

$$Tol. (TI) = Z \sqrt{\frac{1}{N} \left[\frac{\beta-1}{4} + (TI)^2 \right]} \quad , \quad (A-38)$$

where β is the kurtosis of the distribution (the fourth moment about the mean divided by the square of the second moment about the mean). The assumption that $\frac{\beta-1}{N} < 0.3$ has been made to obtain Equation (A-27). For a normal distribution $b = 3$. If the distribution is not normal the implication of the value of Z must be re-evaluated. Assuming a normal distribution, Equation (A-38) is plotted in Figure A-3.10. To be 95% assured that the measured TI is within 5% of the true TI requires more than 500 random measurements, an increase by a factor of 10 over the requirements for determining \bar{v} to the same accuracy and assuredness. The number of measurements will increase further if higher moments are desired. Also, in many measurement situations the distributions are not Gaussian and β can be substantially larger than 3. As a result, the requirement for the number of measurements increases still more.

A-3.1.5.5 Uncertainties due to Flow Characteristics

The preceding discussion has assumed that the velocity

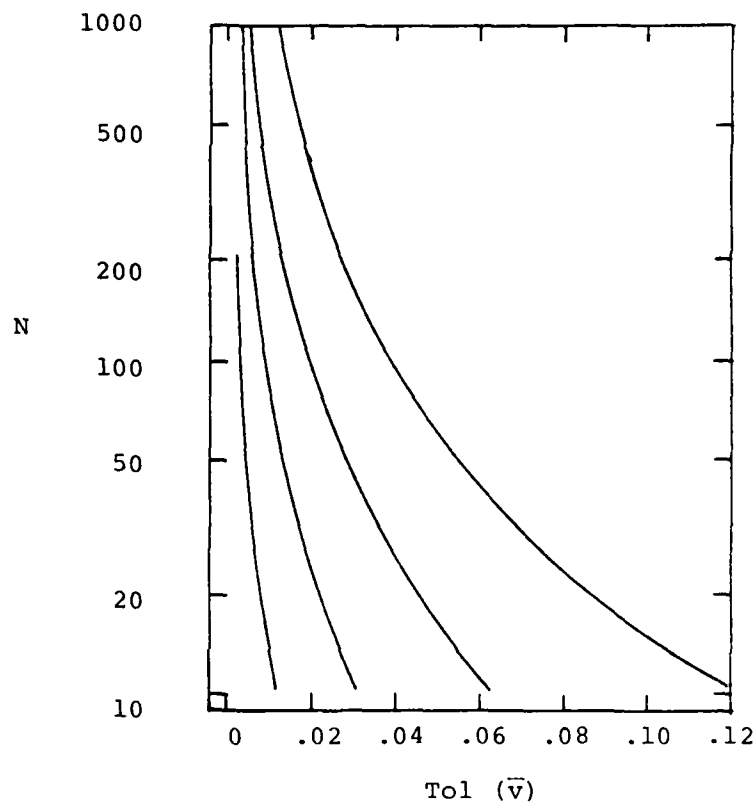


Figure A-3.9 Uncertainty in assurance that estimate of measured v is within three standard deviations of true v as a function of the local turbulence intensity and the number of independent velocity measurements.

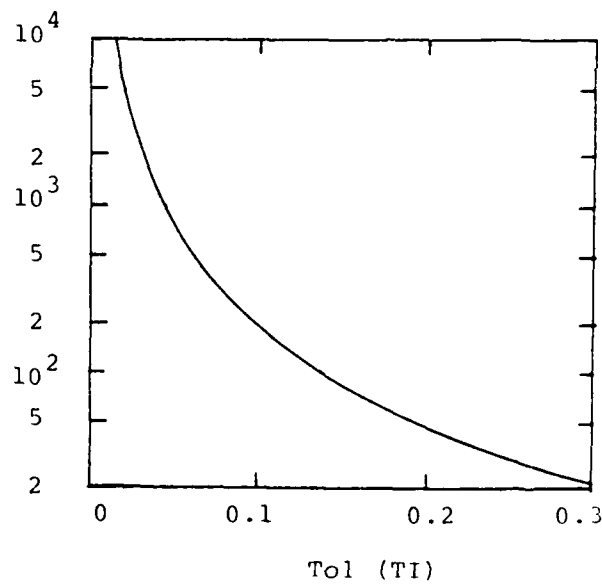


Figure A-3.10 Uncertainty in assurance that estimate of measured TI is within three standard deviations of true TI as a function of the number of independent measurements.

measurements are independent (random). Edwards²⁸ has investigated the effect on \bar{v} of the measurement rate, the flow properties, and the C-P properties. He found that the variance in the estimate of the measurement of the mean velocity, $\sigma_{\bar{v}}^2$, is given by

$$\sigma_{\bar{v}}^2 = \frac{2\tau_c}{T} \left[\frac{\sigma_m^2}{2R\tau_c} + \sigma_v^2 \left(1 + \frac{1}{2R\tau_c} \right) \right] \quad (A-39)$$

where τ_c is the flow correlation time, T is the time over which measurements were made, σ_m^2 is the variance in individual measurements due to errors (bias or uncertainty), R is the data arrival rate, and σ_v^2 is the flow variance. The key to accurately determining the average velocity is to take measurements for many correlation times, $T \gg \tau_c$. Merely increasing R is not sufficient. The combination of R and T should be chosen to provide sufficient data elements to reduce statistical uncertainty while also reducing the uncertainty in the mean, due to flow conditions, both to within acceptable bounds. In general, Edwards suggested that the arrival rate should be adjusted to ensure that $T > 200 \tau_c$. Then, based upon the computed value of τ_c and several parameters characteristic of the apparatus, a corrected \bar{v} could be computed.

The key point that should be made is the interactive nature of the data-taking process. The amount of data needed to correctly characterize the flow at the measurement location depends upon the flow being measured. Consequently an interactive computer with on-line data reduction is required to determine whether the measurement made meets the accuracy desired.

A-3.1.5.6 LDA Beam Deflection Effects

Another potential source of error in the dual beam LDA system would be the motion of the beams due to density fluctuations along the optical path. This will also give rise to the wd contribution in Equations (A-29a) and (A-29b). Two other potential error modes have received some study. The "fringe" spacing could change altering the frequency to velocity conversion fac-

AD-R165 950

TECHNIQUES FOR OPTICAL INTERFERANEMOGRAPHY<U> DAYTON

2/2

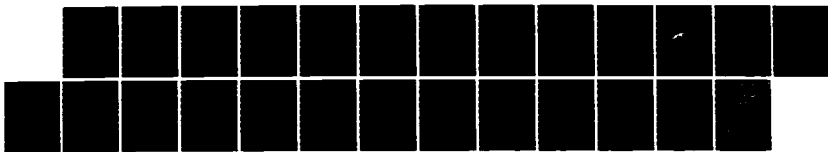
UNIV OH RESEARCH INST A J LIGHTMAN ET AL DEC 85

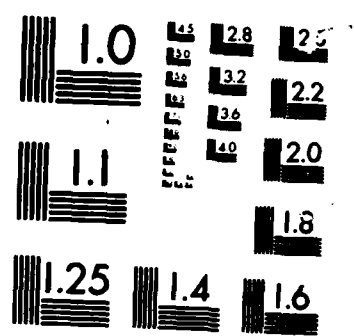
UDR-TR-85-101 AFHAL-TR-85-3898 F33615-83-C-3828

F/G 20/6

NL

UNCLASSIFIED





MICROCOPY RESOLUTION TEST CHART

tor, K [Equation (A-16)], and/or the "fringes" could be in motion contributing an additional frequency offset. Bouis²⁹ monitored the "fringe" system in a hot flow supersonic wind tunnel (1700°K, 720 m/s) and found that the "fringe" spacing fluctuation was $\pm 0.1\%$ and the combined sources of error gave an uncertainty of $\pm 0.3\%$. Both of these errors are small.

A-3.1.5.7 Seed Influence

The size requirements on the seed particles, to ensure faithful tracking of the velocity field, follow directly from an analysis of the relative motion³⁰ of the fluid and the seed particle. In gas flows, where $\rho_p/\rho_f \gg 1$ the equation of motion reduces to

$$\frac{d}{dt} U_p = \frac{18 \mu}{\rho_p d_p^2} (U_f - U_p) \quad (A-40)$$

where ρ is the density, U is the velocity, and d is the diameter. The subscripts are p for particle and f for fluid. Quite often the criterion used to evaluate a particle's suitability is based upon the fidelity of the particle's kinetic energy compared to that of the fluid. This has the form

$$\frac{\overline{U_p^2}}{\overline{U_f^2}} = \frac{1}{1 + \frac{2\pi f}{C}} \quad (A-41)$$

where f is the turbulent fluid fluctuation frequency and

$$C = \frac{18 \mu}{\rho_p d_p^2}. \quad \text{Typical response curves are shown in Figure A-3.11.}$$

It should be understood that this test is only on the kinetic energy. There are more stringent tests that require fidelity in both amplitude and phase for the particle's response to the fluid

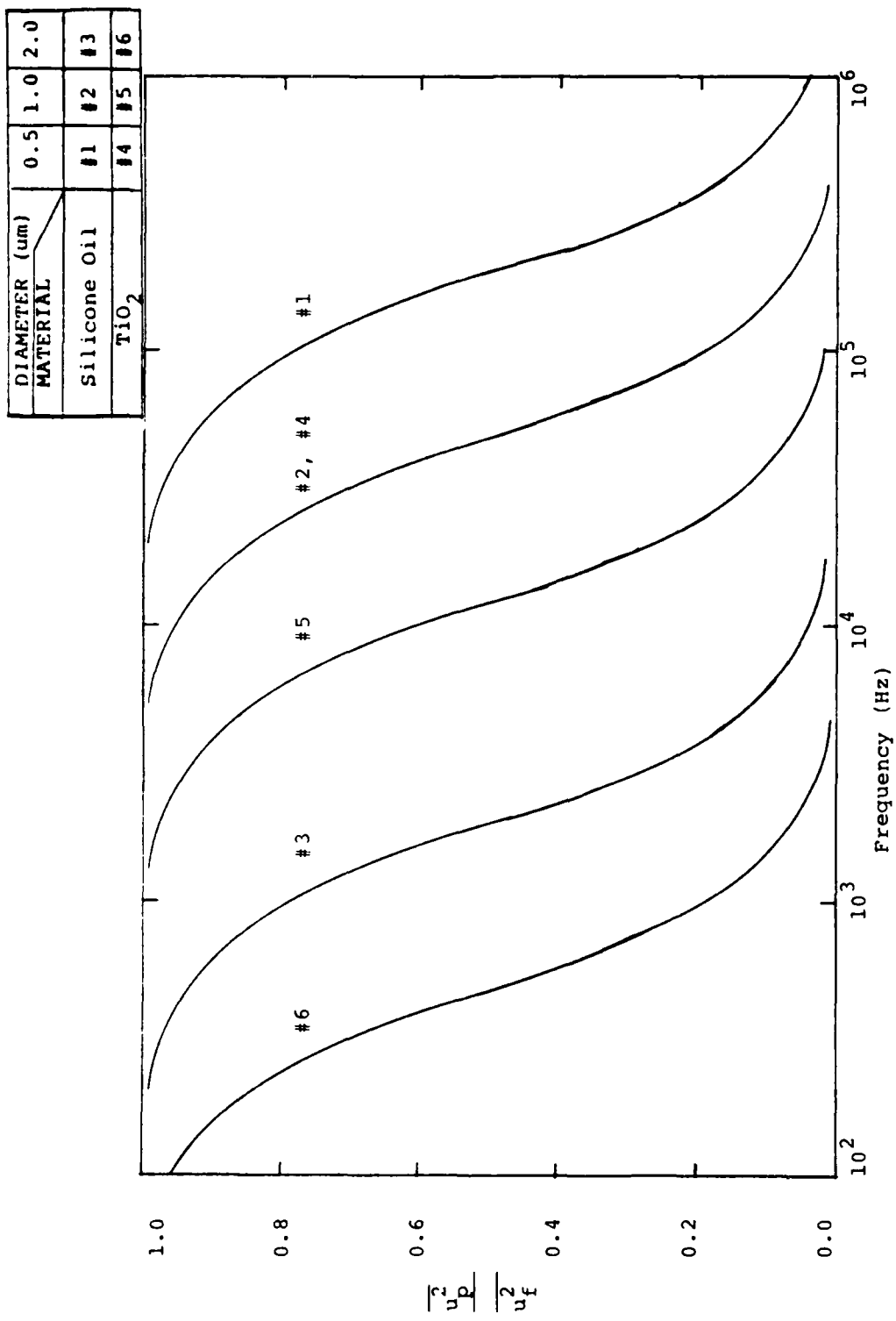


Figure A-3.11 Fidelity of response for seed particles of silicone oil and TiO_2 with diameters of 0.5, 1.0, and 1.5 μm .

fluctuations. These tests and their results in subsonic and supersonic flows have been reviewed^{31,32} and, as a rule of thumb, Melling³¹ suggests that subsonic flows be seeded with particles $< 1 \mu\text{m}$ in diameter and supersonic flows be seeded with particles 0.3 to 0.5 μm diameter. A major difficulty is the decrease in scattered intensity as the diameter decreases. For the diameter mentioned, the scattered intensity is approximately proportional to d^4 and it may be necessary to trade response for signal depending upon the circumstance. Devices for dispersing and injecting the seed are reviewed by Melling.³¹

Seeding the flow appropriately and the ability of the seed to follow the flow have been major concerns in wall boundary layer studies. Many studies have measured a decrease in the Reynolds shear stress very close to the wall when using LDA instrumentation. This is contrary to prediction and to hot wire measurements. Demotakis³³ has suggested that this error is seed related. He suggests that the seeds do not follow the strong turbulent structures near the surface. Instead they impact the surface and stick and, as a result, the LDA measurements are biased, showing a net velocity into the wall. These results have been called into question by Schairer³⁴ who suggests that orienting the LDA fringe system at $\pm 45^\circ$ to the wall normal and using a Bragg cell frequency offset might compensate for LDA measurement errors taken in the boundary layer very near the surface. His measurements had too much scatter to be conclusive but the trend appeared correct. This orientation and frequency offset of the LDA system are also suggested in this report. The result may be doubly beneficial.

A-3.1.5.8 Scattering Considerations

Another important consideration in the design of the LDA system is the placement of the detector. Figures A-3.12a-c are plots of the scattering intensity as a function of azimuthal angle for

SCATTERING INTENSITY PLOT FOR A SPHERICAL PARTICLE

ELEVATION: 0. DEG
LASER WUL: C. 5145 (UM)

PARTICLE DATA:
INDEX: (1.47, 0.00)
RADIUS: 0.25 (UM)

MIE PARAMETER: 3.1

SCATTERED INTENSITY
PERPENDICULAR —
PARALLEL
(0 DEG): 0.790E+02

SCATTERED INTENSITY (08)

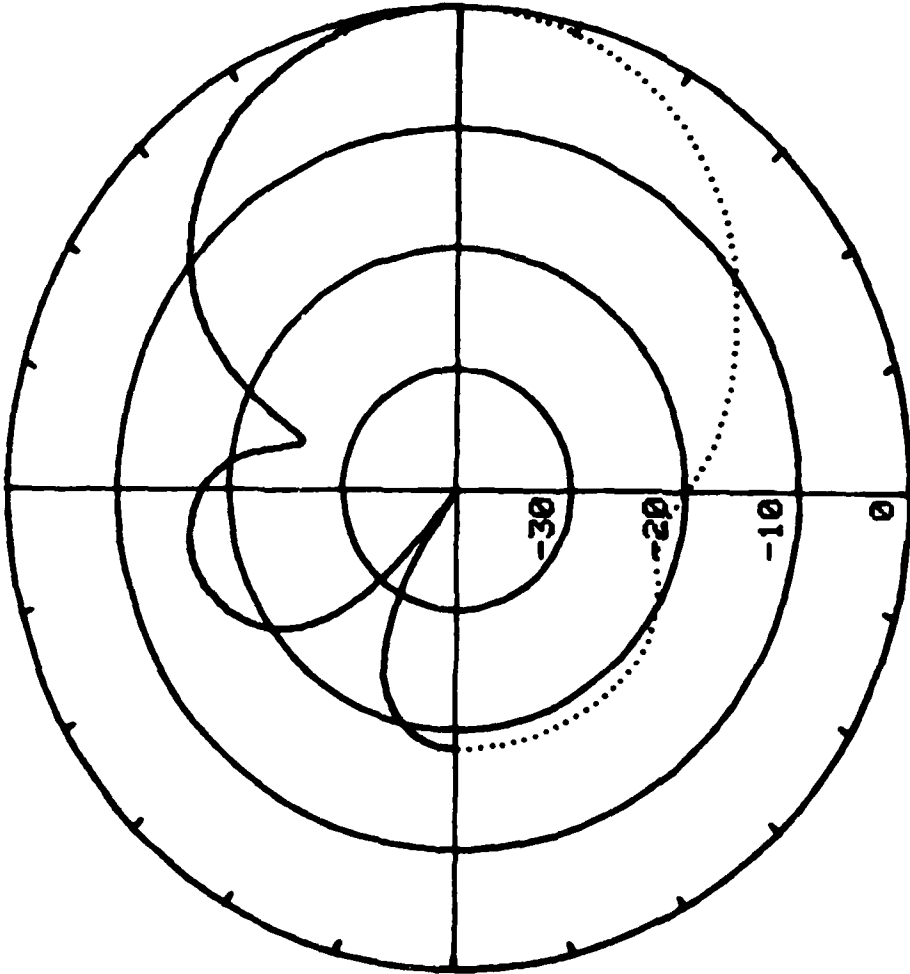


Figure A-3.12a Polar plot of scattering intensity for the components polarized parallel and perpendicular to the plane formed by the laser propagation vector and the scattering direction vector, for particles having an index of refraction of $1.47 + 0i$ and diameters of: (a) 0.5 μm ; (b) 1.0 μm ; (c) 1.5 μm .

SCATTERING INTENSITY PLOT FOR A SPHERICAL PARTICLE

ELEVATION: 0. DEG
LASER WVL: 0.5145 μm

PARTICLE DATA:
INDEX: (1.47, 0.01)
RADIUS: 0.50 μm

MIE PARAMETER: 6.1

SCATTERED INTENSITY

PERPENDICULAR —
PARALLEL
(0 DEG): 0.986E+03

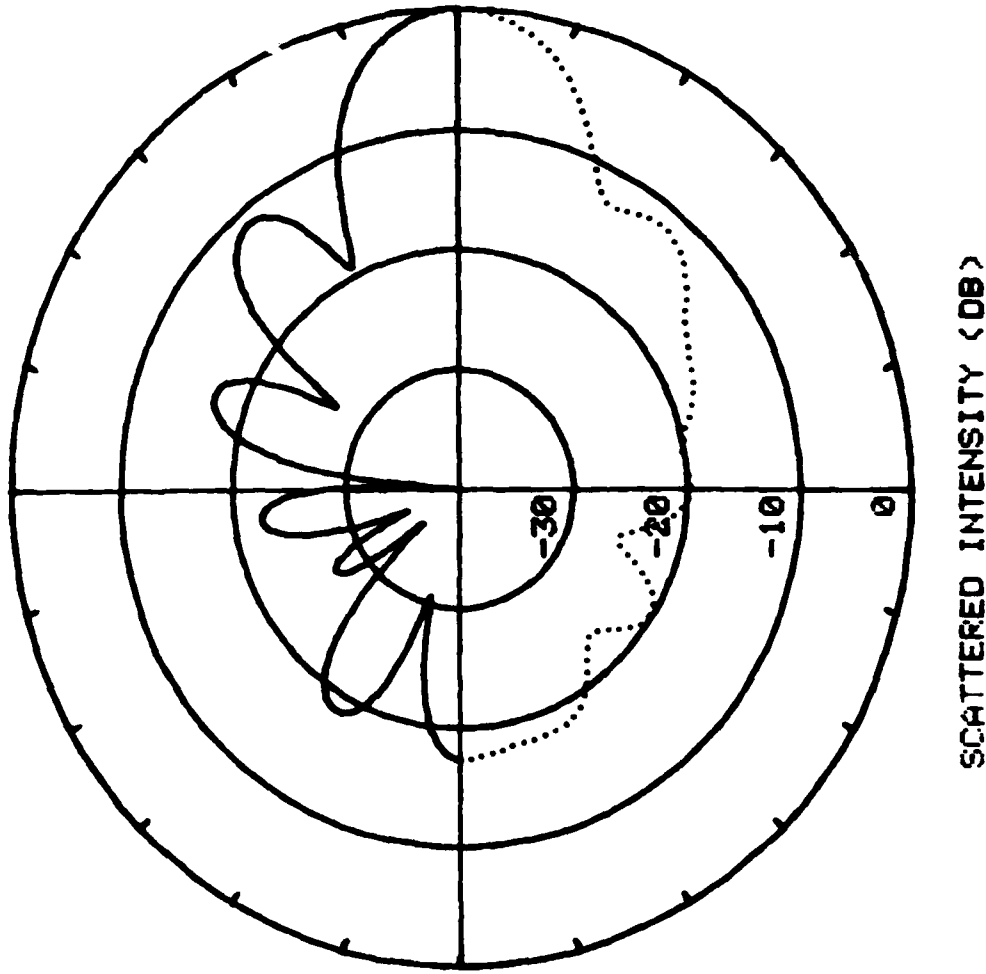


Figure A-3.12b Polar plot of scattering intensity for the components polarized parallel and perpendicular to the plane formed by the laser propagation vector and the scattering direction vector, for particles having an index of refraction of $1.47 + 0i$ and diameters of: (a) 0.5 μm ; (b) 1.0 μm ; and (c) 1.5 μm .

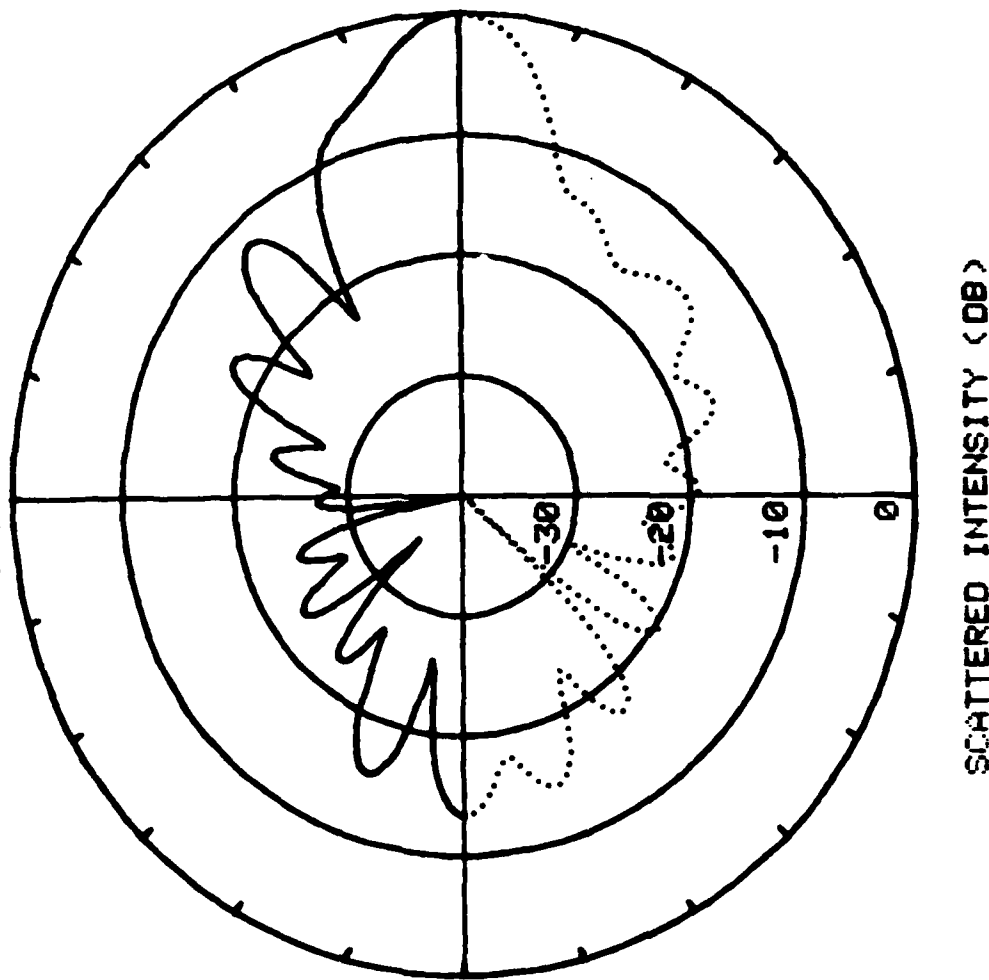
SCATTERING INTENSITY PLOT FOR A SPHERICAL PARTICLE

ELEVATION: 0 DEG
LASER WVL: 0.5145 (UM)

PARTICLE DATA:
INDEX: (1.47, 0.00)
RADIUS: 0.75 (UM)

MIE PARAMETER: 9.2

SCATTERED INTENSITY
PERPENDICULAR —
PARALLEL
(0 DEG): 0.192E+04



A-66

Figure A-3.12c Polar plot of scattering intensity for the components polarized parallel and perpendicular to the plane formed by the laser propagation vector and the scattering direction vector, for particles having an index of refraction of 1.47 + i1 and diameters of: (a) 0.5 μm ; (b) 1.0 μm ; and, (c) 1.5 μm .

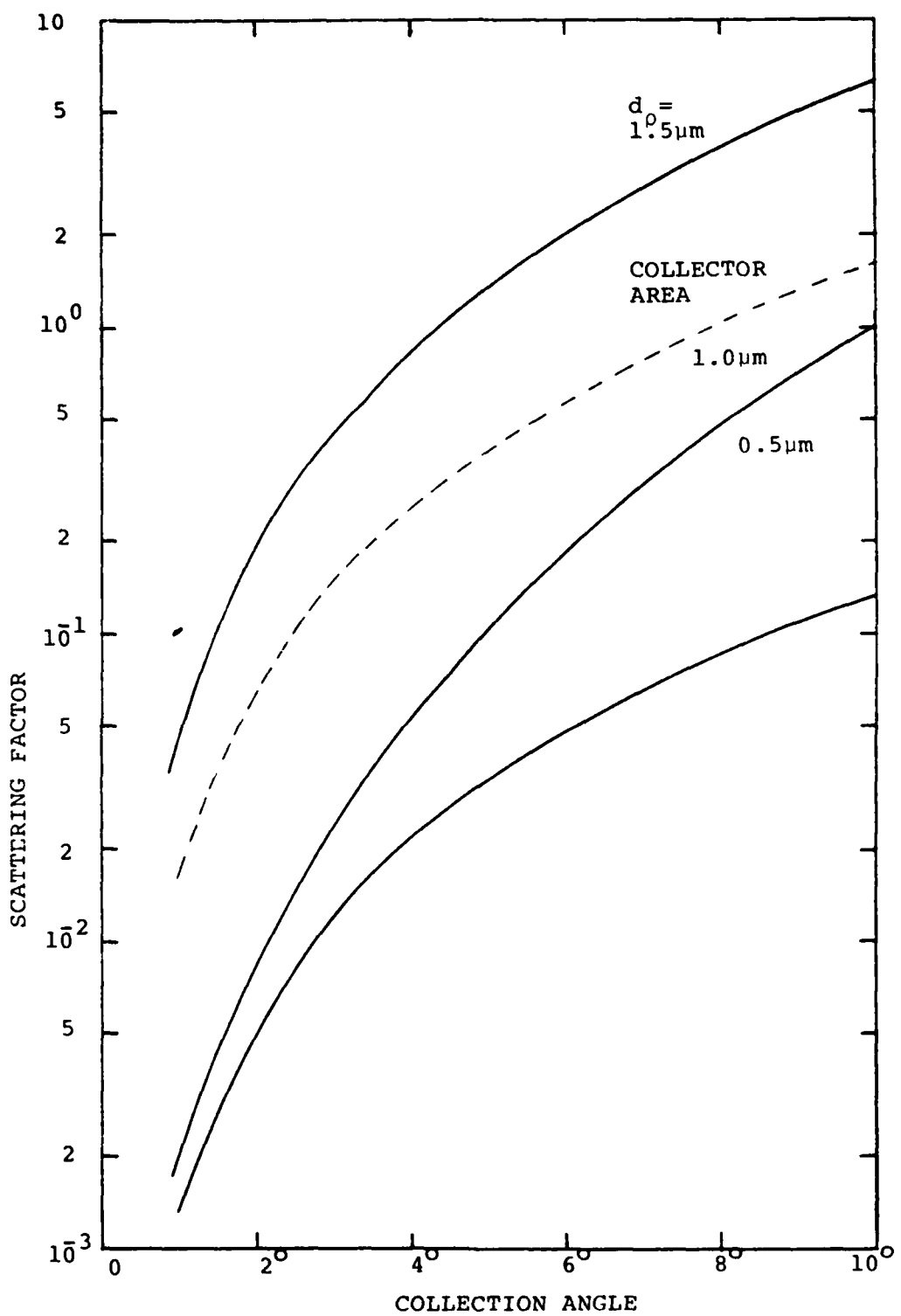


Figure A-3.13. Scattering factor as a function of collection angle for Silicone Oil droplets of 0.5, 1.0, and $1.5\mu\text{m}$ diameter and a detector collector centered at 165° to the forward LDA optic axis.

the components perpendicular and parallel to the scattering plane.³⁵ The radial distance scales logarithmically and it can be seen that there are large variations in amplitude over small azimuthal angle variations near the backward direction. The plots are for silicone oil droplets 0.5, 1.0, 1.5 μm in diameter, and input radiation at 514.5 nm. If the seed is monodispersed, the detector can be positioned to collect a maximum in the scattered radiation. If there is a spread in the seed diameters, the detector position must be a compromise choice. There is always a local maximum in the backward direction, but using this lobe results in the worst case for LDA spot localization. Collecting the backscattered radiation at an angle may result in the detector being placed over a local minimum in the scattering amplitude, such as at 150° for the 0.5 μm droplets, or 165° for the 1.0 μm droplets. Therefore, scattering plots should be used to help select the position for the collector. The information can be used to advantage. Often seeders will provide droplets with a narrow distribution of diameters. If the smaller scatterers will follow the flow better than the larger scatterers, the collection angle can be chosen to enhance the signals from the desired size scatterer, e.g., choosing a collection at 165° discriminates against droplets 1.0 μm diameter. But if the range of diameters is too large, this type of discrimination is not effective (Fig. A-3.12c).

It should also be remembered that the scattered intensity is strongly dependent upon the size. Therefore, even though there may be a minimum in the local scattering amplitude, used to discriminate against a particular diameter, the actual scattering amplitude for the size discriminated against may not be less than for the desired size. Figure A-3.13 is a plot of the collected scattering intensity for different sized collection angles centered at 165°. Although this angle represents a minimum for the 1.0 μm droplets, the scattered intensity for the two diameters is almost the same. As the collection aperture increases, so that the

collected scattered radiation includes that from regions beyond the minimum, the scattering intensity from the 1.0 μm diameter droplet increases much more rapidly than that from the 0.5 μm droplet and becomes an order of magnitude larger for a collection half-angle of 10°.

Another parameter of importance is the signal quality. Positioning of the detector and selection of the scatterer diameter should not be based solely on the scattering amplitude but should also take into account the Doppler signal amplitude, especially by looking into the expected S/N at the detector. Shown in Figure A-3.14 is a plot of the Doppler signal visibility, the pedestal peak rms amplitude, and the maximum S/N in the case of shot noise limitation. Figure A-3.14 was plotted for the detector located at 165° azimuth. It is evident that using a scatterer with radius 0.35 μm to 0.70 μm results in a significant decrease in the visibility and will show a corresponding decrease in the S/N compared with signals from scatterers with radii either slightly smaller or larger.

The factor needed to convert from the relative scattering amplitude scale used in Figure A-3.14 is k^{-2} ($k = 2\pi/\lambda$). Therefore a pedestal amplitude of 1 corresponds to a scattering cross-section of $6.07 \times 10^{-15} \text{ m}^2$ at 514.5 nm. For a total laser power of 1 Watt into the 250 μm diameter spot, the average number of photons collected by the detector, at the location and with the dimensions given, would be 3.053×10^{11} . To resolve a Doppler cycle the signal should only be integrated for 1/6 of a cycle. At 70 MHz this computes to 567 photons per integration period. This will vary depending upon whether the scatterer is at the center of the LDA spot or near the edge and whether the maximum or the average of the Doppler cycle is being considered. Nevertheless the computation is a good indicator of the expected signal strength and the associated Poisson fluctuation. A more accurate computation will depend upon the particular geometry used, the scatterer's properties, and the laser power in the actual system.

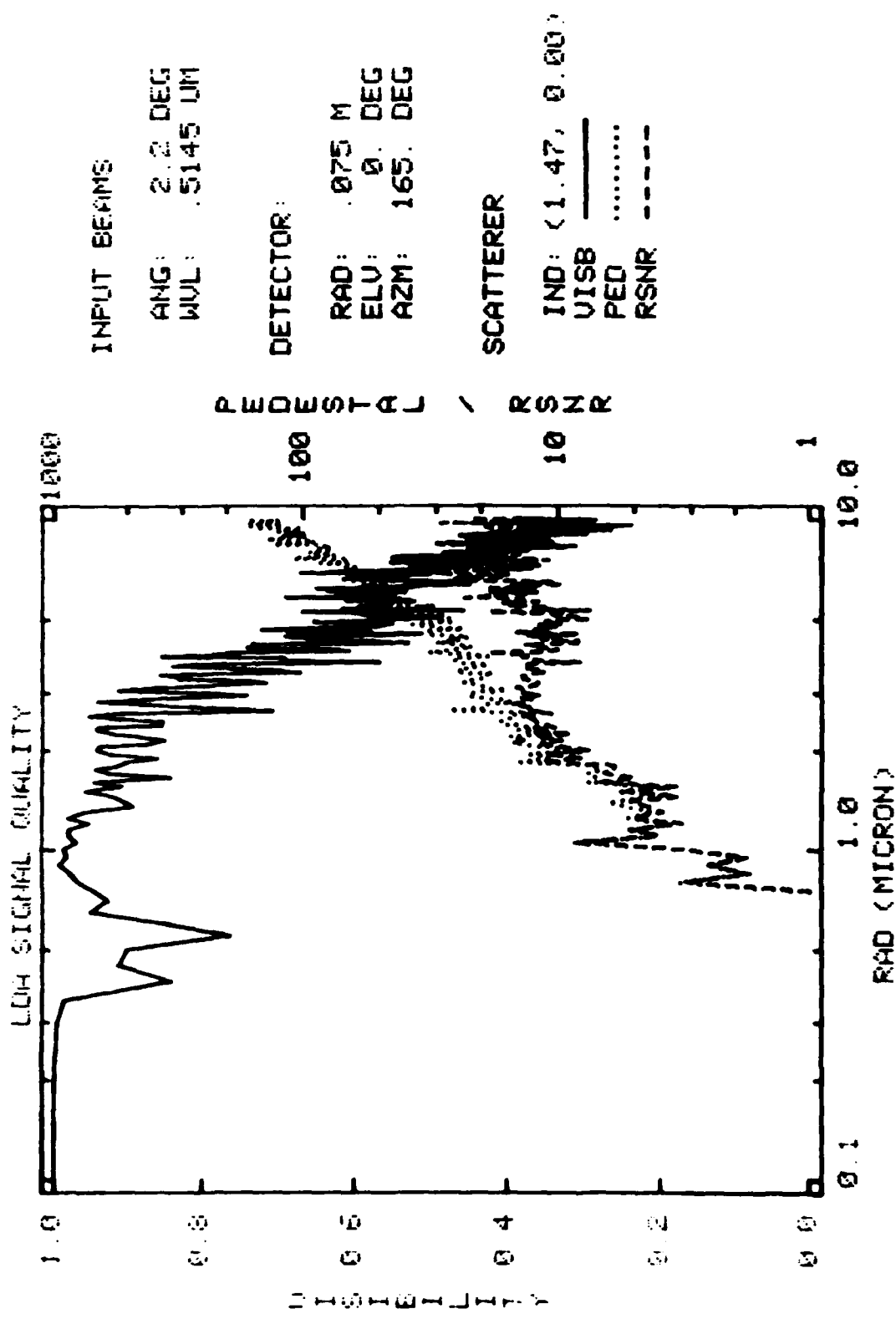


Figure A-3.14 LDA signal quality (visibility, pedestal amplitude, and relative Doppler signal to noise ratio) for scatterers with index $1.47 + i_0$ having a radius between $0.1 \mu\text{m}$ and $10 \mu\text{m}$.

A-3.2 ALTERNATE TECHNIQUES FOR FLOW FIELD VELOCITY MEASUREMENTS

The time-of-flight techniques were introduced at the beginning of this section with reference to the two-spot and transit velocimeters. There is another class of techniques based upon time-of-flight type measurements but it offers a distinct advantage to the aforementioned methods, principally it records a two-dimensional field of the flow at one time. The basic technique is to record a "snapshot" of the flow at two instants of time and to measure the change at each location in the flow that is imaged. There are three interesting variations of this technique which will now be discussed.

First, and perhaps most obvious, is to use sheet light scattered from seed particles in the flow. The light is pulsed twice and a simple frame of film is double exposed.³⁶ The pulses are timed so that the motion of the scatterers can be seen but it is not so great that there is confusion interpreting where particles moved to. If the flow is seeded with particles having the appropriate characteristics (size, shape, etc.) this technique combines both visualization and quantitative measurement. Another appealing feature of this technique, besides its two-dimensional mapping (velocity and field-of-view), is that it lends itself to straightforward machine analysis of the data. A laser scanner can be adjusted in size so that it can illuminate only one exposure pair at a time and the two-dimensional velocity can be read. A variation which we suggest is to provide some depth to the light sheet and to photograph the scattering from two angles. By triangulating the resulting velocity vectors it should be possible to measure velocity in three dimensions.

The second technique is to use front-illuminated holographic recording of the seed particles in the flow. If a double-pulsed hologram is recorded, the full volume illuminated can be examined in the reconstruction and the motion can be determined at each plane by adjusting the focus of the data inspection optical

Table A-3.1 Velocity Measurement Summary

| Technique | No. components measurable simultaneously | Direct-sensitivity | Maximum Velocity | Velocity Dynamic Range ⁴ | Spatial Resolution ⁵ | Comments |
|------------------------------------|--|--------------------|------------------|-------------------------------------|---------------------------------|--|
| Transit Velocimetry (1-spot) | 1 | No | H | L | H | This method has received limited use. It could be advantageous where optical access is very limited and/or where interference (scattering, background radiation) is troublesome. |
| Time-of-flight (2-spot) | 1 | Yes ¹ | H | H | H | Strong selection in situations where interference is a problem. Recent innovation providing directional sensitivity may enhance its usefulness. The lack of a multi-dimensional measurement capability is a drawback. |
| Fabry-Pérot Interferometer | 1 | Yes | H | H | H | Commonly used to measure very high velocities (even relativistic velocities). It cannot resolve the fluctuations typically associated with aerodynamic flows. |
| Fluorescence | 1/2 ² | Yes | H | H | H | Used in supersonic flow studies. It may be extendable to making two-dimensional velocity measurements at a point in space. Technological improvements may permit global survey velocity measurements in a single observation. |
| CARS/SRS | 1 | Yes | H | H | H/H | Limited in application as a velocity only technique. These methods provide a great deal of other information (density, concentration, temperature, etc.) and the velocity measurement is in addition to these other parameters. |
| LDA | 3 | Yes | H | H | H | Most commonly used velocity measurement technique. It has significant advantages over the other methods (3-D, high dynamic range, and high spatial resolution). Its disadvantages are that the measurements may be intermittent (seeded flows) and in aerodynamic studies specialized signal processors and high-speed computers are usually required. |
| Multi-pulse photography/holography | 2/3 ³ | No ² | H | L | H | This method shows promise, especially in liquid flows. Stereoscopic observation and laser analysis may provide a system with survey capability. |

*One dimensional measurements are standard. "Two-dimensional" measurements have been claimed in the literature but they are wrong. A correct extension to two-dimensional measurements can be made.
**Stereoscopic extension of the two-dimensional system will provide the third component.

- Recent innovations have provided directional sensitivity.
- While direct directional sensitivity is not possible, direction of flow can usually be inferred from the simultaneous global velocity mapping provided by this method.
- The maximum velocity capability is highly dependent upon many factors, most particularly upon the system geometry. The values given represent approximate maxima according to the scale; $H \leq 10^3$ m/s, and $H > 10^3$ m/s.
- This is a rule-of-thumb guideline for the approximate fractional velocity resolvable. The scale is: $L = 0(10^1)$, $H = 0(10^2)$, $W = 0(10^3)$, and, O_1 implies order of magnitude.
- Spatial resolution is another parameter greatly influenced by the system geometry. Several systems, particularly the one-spot and two-spot methods, are advantages in systems that only allow backscattering collection. Consequently the depth of field can provide significant uncertainty to the location of the event. On the other hand these systems have been used with scattering collected at right angles to the beams yielding good spatial resolution. The criteria used to determine L, H, W ranking was typical geometry (from the authors experience) and whether the nature of the method necessitated spatial localization (ex. KODCARS, dual-beam IDH).

system.³⁷ The advantage to this approach is that the entire flowfield is recorded at one time. The system required to examine the data and interpret the measurements is complex but the potential is so great that it is being pursued.

The last technique that is discussed here combines some of the features of the previous two but with a major distinction, no seed particles are used. Instead variations in density in the flow field are used as velocity tracers. These velocity variations produce an effect called "speckle" in the reconstructed wavefront image.³⁸ In a double-pulsed recording the density fluctuation will move slightly between exposures and the reconstructed speckle pattern will exhibit interference fringes that determine the local two-dimensional velocity.

A-3 SUMMARY

The various techniques for measuring velocity have been summarized in Table A-3.1. The range of operating conditions that each method can be used to study is so great that only the coarsest of scales can be used to differentiate the techniques. The principle areas of concern are the number of velocity components determinable and a combination of maximum velocity and fractional velocity that need to be measurable. For example, hypersonic velocities almost require a standard spectroscopic technique to measure the Doppler shift. But in these cases small fractional changes (<1%) are almost impossible to measure. The overlap between the capabilities is quite large and choice of a particular method will depend upon the total system requirements. In only one situation is the choice clear at this time-- simultaneous three component measurements are the province of LDA. One closing comment. Several techniques (CARS/SRS) do provide other information beside velocity, such as density, pressure, and temperature. These parameters are of vital concern in aerodynamic studies and, as a result, some combination of techniques may be highly desirable.

SECTION A-4

CONCLUSIONS

As a result of our evaluation of the present state-of-the-art in technologies required for a real-time interferanemography system, we have found that although we can define the laser Doppler anemometry system for inclusion in real-time interferanemography, it is not possible to design and build, at this time, an interferometric system suitable for real-time use for all the types of air flow to be studied.

A-4.1 INTERFEROMETRY

Summarizing the prospects of obtaining perturbation values of density for air flows in wind tunnel applications, the following points are made:

(1) To obtain truly accurate perturbation densities, multiple views of the field are required. Without multiple viewing capabilities, the flow fields studied have to be no more complex than two-dimensional axisymmetric. Even then, the perturbations can not be local to any specific point in the flow; they too must be two-dimensional.

(2) In addition to obtaining multiple views, continuous interferometric surveillance of the flow is required. Meeting this requirement using holographic interferometry would be difficult with its requirements for vibration isolation, separated two beam optical geometry, multiple hologram recording and processing, and temporal coherence requirements.

(3) The use of Point Diffraction Interferometry appears promising as a technique that might provide continuous interferometric surveillance of air streams. However, this technique has not been applied to wind tunnel studies, and both theoretical and experimental development of specific PDI processes has to be

accomplished before the worthiness of this technique can be assessed. Therefore, as a recommendation, PDI techniques should be analyzed and applied to control experiments to determine the degree of measuring ability especially with respect to sensing perturbations in density.

(4) Heterodyne interferometry techniques offer promise to obtain true real-time evaluation of the object wavefront. However, this technique should be analyzed and applied to control experiments to determine the degree of real-time measuring ability especially with respect to sensing perturbations in density.

(5) Because of the relatively low interferometric sensitivities of the hypersonic facilities of AFWAL/FI, interferometry should not be used as a means of measuring densities in these wind tunnels. Furthermore, applications for subsonic studies in the TGF wind tunnel and applications at the high total pressure levels of the Mach 3 and 6 wind tunnels also appear poor. The best applications appear to be for transonic and supersonic operation of the TGF facility, and for moderately low total pressure levels of the Mach 3 and 6 wind tunnels.

A-4.2 LASER DOPPLER ANEMOMETRY

This study has investigated the requirements for making three-dimensional LDA measurements in a wind tunnel. Where optical access is limited, as in the AFWAL/FI transonic facility, the optical configuration providing the best measurement accuracy is shown in Figure A-3.5a. The angle between the LDA systems, ϕ , is set to the maximum allowable consistent with good experimental design. Furthermore, the two-dimensional LDA system should be aligned to take measurements along directions at $\pm 45^\circ$ to the free stream velocity. In boundary layer studies it is assumed that the boundary is parallel to the free stream. If this is not the case, a compromise angle has to be used that is consistent with

the needs of both the free stream and the boundary layer, particularly when near the boundary. This last decision is based upon the requirements for accurate Reynolds stress measurements near the boundary and has been discussed earlier.

It has been shown that the data collection and data interpretation are interactive. Consequently it is essential that a computer, preferably a high-speed system capable of quasi real-time data evaluation, be used for data collection and analysis. In addition to the velocity record, other parameters should be recorded simultaneously. These include the time at which the velocity datum became available and the number of Doppler cycles in the burst. Due to the limited capability of the counter-processors for measurements in supersonic free streams, alternative forms of processing the LDA signals should be investigated.

REFERENCES

1. M. Cem Gokay, Oven-Heated Copper Vapor Laser System, University of Dayton Funded Proposal with NASA/Langley, R-4787, (1983).
2. J. S. Harris, R. L. Fusek, and J. S. Marcheski, "Stroboscopic Interferometer," Applied Opt., 18, No. 18 (1979)
3. R. M. Smartt, "Point Diffraction Interferometer," Journal of the Opt. Soc. of America, 62, 737 (1972).
4. N. A. Massie, R. D. Nelson, and S. Holly, "High-Performance Real-time Heterodyne Interferometry," Appl. Opt., 18, No. 11 (1979).
5. D. J. Holve, "Transit Timing Velocimetry (TTV) for Two-Phase Reacting Flows," Combust. Flame 48, 105 (1982).
6. L. Lading, "The Time-Of-Flight Laser Anemometer," in Applications of Non-Intrusive Instrumentation in Fluid Flow Research, AGARD CP-193, paper 23 (1976).
7. S. A. Self, "Boundary Layer Velocity Measurements in Combustion MHD Channels," in Laser Velocimetry and Particle Sizing, Hemisphere Publishing Corp., New York, 1979, pp. 347-356.
8. R. B. Miles, "Resonant Doppler Velocimeter," Applications of Non-Intrusive Instrumentation in Fluid Flow Research, AGARD CP-193, paper 19 (1976).
9. M. Zimmerman and R. B. Miles, "Hypersonic-helium flow-field measurements with the resonant Doppler velocimeter," Appl. Phys. Lett. 37, 885 (1980). Also, M. Zimmerman, "Resonant Doppler Velocimeter," Ph.D. Thesis, Princeton University, 1980.
10. J. C. McDaniel and D. Baganoff, "Density measurement in compressible flows using off-resonant laser-induced fluorescence," Phys. Fluids 25 (7) 1105 (1982).
11. J. C. McDaniel, B. Hiller, and R. K. Hanson, "Simultaneous multiple-point velocity measurements using laser-induced iodine fluorescence," Opt. Lett. 8 (1) 51 (1983).
12. J. C. McDaniel, Jr., "Investigation of Laser-Induced Iodine Fluorescence for the Measurement of Density in Compressible Flows," Stanford University Department of Aeronautics and Astronautics No. 532, 1982.
13. G. Kychakoff, R. D. Howe, R. K. Hanson and J. C. McDaniel, "Quantitative visualization of combustion species in a plane," Appl. Opt. 21 (18) 3225 (1982).

- 13a. G. Kychakoff, R. D. Howe, and R. K. Hanson, "Quantitative flow visualization techniques for measurements in combustion gases," *Appl Opt.* 23 (5) 705 (1984).
14. F. Durst, A. Melling, and J. H. Whitelaw, Principles and Practice of Laser Doppler Anemometry, Academic Press, New York, 1976.
15. R. J. Adrian, "Laser Velocimetry," University of Illinois at Urbana-Champaign, T. & A. M. Report No. 442.
16. A. J. Siegman, An Introduction to Lasers and Masers, McGraw-Hill Book Company, New York, 1971.
17. R. J. Adrian and K. L. Orloff, "Laser Anemometer Signals: Visibility Characteristics and Application to Particle Sizing," *Appl. Opt.* 16, 677 (1977).
18. H. Kogelnik and T. Li, "Laser Beams and Resonators," *Appl. Opt.* 5, 1550 (1966).
19. A. Yariv, Quantum Electronics, John Wiley & Sons, Inc., 1975.
20. DISA, 3-D Laser Doppler Anemometer.
21. TSI, LDV System 9100.
22. P. K. Snyder, K. L. Orloff, and K. Aoyagi, "Performance and Analysis of a Three-Dimensional Nonorthogonal Laser Doppler Anemometer," *NASA-TM-81283* (1981).
23. F. L. Crosswy, F. L. Heltsley, and P. M. Sherrouse, "Recent Development and Applications of a Three-Component Laser Doppler Velocimeter," 28th International Instrumentation Symposium, Las Vegas, Nevada, May 1982.
24. R. J. Adrian, J. A. C. Humphrey, and J. H. Whitelaw, "Frequency Measurement Errors Due to Noise in LDV Signals," *Proceedings of the LDA-Symposium Copenhagen 1975*.
25. M. C. Whiffen, J. C. Lau, and D. M. Smith, "Design of LV Experiments for Turbulence Measurements," in Proceedings of the Third International Workshop on Laser Velocimetry, Purdue University, 1978.
26. H. J. Pfeifer, "Signal Processing by Counters and Digital Processing of LDA Signals," in Laser Velocimetry, von Karman Institute for Fluid Dynamics, Lecture Series 1981-3.
27. V. A. Cline and H. T. Bentley III, "Application of a Dual Beam Laser Velocimeter to Turbulent Flow Measurements," *AEDC-TR-74-56* (1974).

28. R. V. Edwards and A. S. Jensen, "Particle Sampling Statistics in Laser Anemometers: Sample and Hold Systems and Saturable Systems," *J. Fluid Mech.* 133, 397 (1983).
29. X. Bouis, "Applications Recentes, a L'ISL, de la Velocimetrie Laser aux Mesures dans des Ecoulements Turbulents, Application of Non-Intrusive Instrumentation in Fluid Flow Research, AGARD CP-193, paper #7, (1976).
30. J. O. Hinze, Turbulence, McGraw-Hill, New York (1959).
31. A. Melling, "Particle Behaviour in Flows and Suitable Particles for LDA Measurements," in Laser Velocimetry, von Karman Institute for Fluid Dynamics, Lecture Series 1981-3.
32. S. L. Lee and F. Durst, "On the Motions of Particles in Turbulent Flows," NUREG/CR-1554 (1980).
33. P. E. Demotakis, D. J. Collins, and D. B. Lang, "Laser Doppler Velocity Measurements in Subsonic, Transonic, and Supersonic Turbulent Boundary Layers," in Proceedings of the Third International Workshop on Laser Velocimetry, Purdue University, 1978.
34. E. T. Schairer, "Turbulence Measurements in the Boundary Layer of a Low-Speed Wind Tunnel Using Laser Velocimetry," NASA-TM-81165 (1980).
35. R. J. Adrian and W. L. Earley, "Evaluation of LDV Performance Using Mie Scattering Theory," Proceedings of the Minnesota Symposium on Laser Anemometry (1975).
36. R. J. Adrian and C. S. Yao, "Development of Pulsed Laser Velocimetry (PLF) for Measurement of Fluid Flow," Eighth Biennial Symposium on Turbulence, Rolla, Missouri (1983).
37. J. S. Harris, K. G. Harding, and J. S. Loomis, Documentation and Evaluation of Water Flow Using Holography, UDR-TR-83-86, National Aeronautics and Space Administration, Langley, Virginia, August 1983.
38. R. Meynart, "Instantaneous velocity field measurements in unsteady gas flow by speckle velocimetry," *Appl. Opt.* 22, 535 (1983).

SUPPLEMENT TO APPENDIX

THREE-BEAM LDA POSITION CONFIGURATION

In order to determine the fluid velocities along the coordinates of interest (x , y , z) the measurement coordinates frame (x' , y' , z') must be known accurately. Often, to simplify the analysis, the 2-D LDA is aligned so that (x' , y') lie in the (x , y) plane. In the LDA configuration where a non-orthogonal 1-D system is used to measure V_z δV_z will be the largest uncertainty. By ensuring that V_z is not required to transform V_x' , V_y' to V_x , V_y the uncertainties in the result are minimized. When the x' , y' axes are aligned with x , y (Figure A-1a) the situation is trivial. When the flow conditions require x' , y' to be at $\pm 45^\circ$ to x , y the situation is not so simple for the 3-beam system. Most LDA systems effect the $\pm 45^\circ$ measurement by rotating the beams, as shown in Figure A-1b, by 45° around the optic axis. Unfortunately this mixes V_z into the equations. If the crossing angle is small, the contribution of V_z to V_x and V_y can be neglected, but this is not always true. The incident beams can be positioned so that the contribution of V_z' to V_x and V_y is zero.

Consider the optical configuration shown in Figure A-2. The beams will be assumed to form an isosceles triangle at the plane of the lens so that only one component need be considered. V_x' is measured by the Doppler signal generated by the beams at $(0, Y_1-D, 0)$ and $(x_1, Y_1, 0)$ due to scattering occurring at the measurement spot $(0, 0, z_1)$. The equation of the plane through these three points is

$$\frac{D}{x_1(D-Y_1)}x + \frac{1}{Y_1-D}y + \frac{1}{z_1}z = 1 \quad (A.1)$$

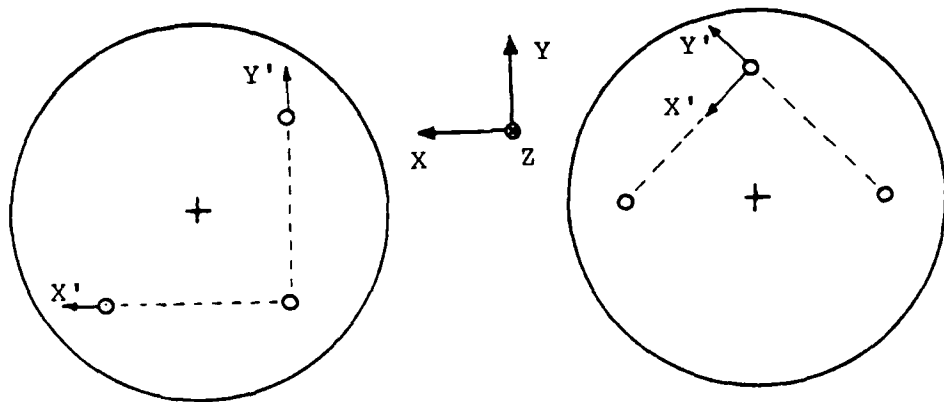


Figure A-A.1 (a) Three beam optical configuration in which (X', Y') plane lies in (X, Y) plane. (b) Commonly employed three-beam configuration where (X', Y') plane does not lie in plane (X, Y) .

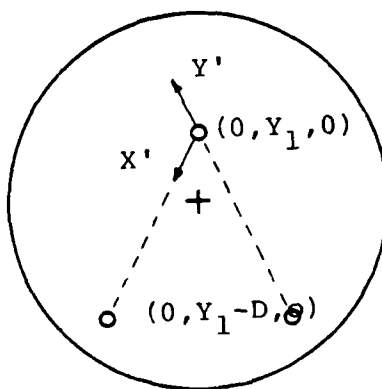


Figure A-A.2 Generalized configuration for beams at crossing-focusing lens.

in the reference coordinate frame. The direction cosines of the normal to this plane are

$$\frac{1}{K_1} \left\langle \frac{D}{x_1(D-y_1)}, \frac{1}{y_1-D}, \frac{1}{z_1} \right\rangle \quad (A.2)$$

where K_1 is a proportionality constant. The measurement direction x' will be perpendicular to (A.2) and also perpendicular to the vector that bisects the intersection plane of the incident beams. This bisector extends through $\frac{x_1}{2}$, $y_1 - \frac{D}{2}$, 0 and $(0, 0, z_1)$ and has direction cosines

$$\frac{1}{K_2} \left\langle \frac{x_1}{2}, y_1 - \frac{D}{2}, -z_1 \right\rangle . \quad (A.3)$$

The direction cosines of the normal to (A.2) and to (A.3) are given by the determinant

$$\frac{1}{K_3} \begin{vmatrix} x & y & z \\ \frac{D}{x_1(D-y_1)} & \frac{1}{y_1-D} & \frac{1}{z_1} \\ \frac{x_1}{2} & y_1 - \frac{D}{2} & -z_1 \end{vmatrix} . \quad (A.4)$$

Therefore, the contribution from V_z to V_x , will be zero if $(y_1 = D)$

$$y_1 = \frac{1}{2D} (D^2 - x_1^2) . \quad (A.5)$$

The most common 3-beam configuration uses two identical beamsplitters, the first one to provide two beams vertically (y) separated by $2d$, and the second to split the bottom beam horizontally (x) by $2d$. (This will not give $\pm 45^\circ$ but rather $\pm 63.4^\circ$. Its common use is a result of the cost of available beamsplitters versus the cost of custom-made beamsplitters.) In this case $x_1 = d$ and $D = 2d$ and according to (A.5)

$$y_1 = \frac{3}{4} d \quad (A.6)$$

The reconstruction from $v_{x'}$ and $v_{y'}$ to v_x and v_y is given by

$$v_x = \frac{\sqrt{5}}{2} (v_{x'} + v_{y'}) \quad (A.7)$$

and

$$v_y = -\frac{\sqrt{5}}{4} (v_{x'} - v_{y'}) . \quad (A.8)$$

Another advantage of this configuration for boundary layer studies is that the value of d_f , dictated by the free stream velocity, can be smaller, enhancing the measurement capability in the direction normal to the surface when inside the boundary layer.

END
FILMED

5-86

DTIC